INFLUENCE OF THE HEAT TREATMENT PROCEDURE ON THE STRESS CORROSION CRACKING BEHAVIOUR OF LOW PRESSURE TURBINE BLADE MATERIAL FV566

Nicole Seumangal

A thesis submitted to the Faculty of Engineering and the Built Environment, at the University of Cape Town, in fulfilment of the degree of Master of Science in Engineering

June 2017

Declaration

I, Nicole Seumangal, know the meaning of plagiarism and declare that all the work in the document, save for that which is properlyacknowledged, is my own. This thesis/dissertation has been submitted to the Turnitin module (or equivalent similarity and originality checking software)and I confirm that my supervisor has seen my report and any concerns revealed by such have been resolved with my supervisor.

Signed by candidate

Signature signature removed

Date ___16/06/2017_____

Abstract

Stress corrosion cracking is one of the leading damage mechanisms in low-pressure turbines in the power generation industry; in LP turbine blades it primarily occurs in the last stage blades. The research investigated the influence of tempering temperature on the microstructure, mechanical properties, and stress corrosion cracking properties of 12% chromium FV566 stainless steel, which is used to manufacture LP turbine blades.

The standard heat treatment of the steel comprises of austenitising, quenching and double tempering. Austenitising is carried out at 1050°C for one hour – which is sufficiently long to generate a fully austenitic matrix and to dissolve carbon completely. Subsequently, the material is quenched in air. The high level of alloying elements ensures the complete martensitic transformation, with carbon atoms trapped in the matrix and distributed homogeneously. Thereafter, tempering of the material at 580-600°C enhances the ductility and toughness. Tempering replaces the solid solution strengthening of the dissolved carbon with precipitation strengthening by carbides. [(1)] [(2)] The final microstructure of the FV566 steel blades is referred to as tempered martensite.

Van Rooyen [(3)] showed that for 12% chromium steel tempering at and above 600°C induces passivity of the material against SCC, while tempering of 12% chromium steels at 450-550°C causes sensitisation of the material and the material exhibits intergranular SCC. From such studies, the motivation arises to investigate the impact of heat-treatment parameters – specifically the impact of tempering temperature on the stress corrosion behaviour of the material.

The testing methodology comprises heat treatment of FV566 samples at 1050°C for 1 hour, at 350°C for 1 hour, and thereafter tempering for 1 hour at various tempering temperatures. Each stage of heat treatment is followed by air cooling – followed by analysis of the microstructure, mechanical testing and stress corrosion cracking testing of the specimens at the different temper conditions.

Stress corrosion testing was divided into two categories. The first set of tests was carried out with U-bend specimens to determine the susceptibility of materials at different heat treatments to SCC, the time taken for SCC to initiate, and the mode of cracking. The second set of tests was conducted to determine the threshold stress intensity, as a function of crack growth rate, for each heat treatment.

The SCC failure mechanism observed was intergranular SCC (IGSCC) by anodic dissolution for the 550°C, 560°C, 570°C, 580°C, 590°C, 600°C and 620°C specimens.

The material's resistance to SCC improved with increasing tempering temperature. Specimens tempered at 480°C and 550°C were most susceptible to SCC, while specimens tempered at 600°C were immune to SCC in a 4000-hour period. A change in tempering temperature results in a change in the quantity and type of precipitates formed which results in changes in SCC properties of FV566.

Acknowledgements

I would like to thank the following people for their contribution during the course of this study, without which the research would have been impossible:

My supervisors Professor Bernhard Sonderegger and Professor Knutsen, for their constant encouragement, guidance and supervision throughout the work.

Professor Robert Knutsen for his support, relentless encouragement and guidance.

Dr J Westraadt and the staff at the Centre for High Resolution TEM (CHRTEM) at the Nelson Metropolitan University – for assistance on the EBSD and TEM work for the microstructural analysis.

Mr Glen Newins and the workshop staff for their expertise and help in producing the specimens.

Mrs P. Park-Ross and Candice Mias for their assistance in the laboratory.

Miranda Walton and Innocent Shiru for assistance with the Scanning Electron Microscope.

The Eskom Power Plant and Engineering Institute for financial support and the opportunity to study further.

To all my fellow students at the Centre for Materials Engineering – for making the experience a memorable and enjoyable one.

My family for all their encouragement and support.

List of Acronyms and Abbreviations

a	Crack length
a_f	Final crack length
a_0	Starting crack length
Al	Aluminium
ASTM	American Society for Testing and Materials
B	Thickness
BCT	Body centred tetragonal
C	Carbon
CCD	Charged coupled device
CCR	Crack growth rate
CF	Corrosion fatigue
CLL	Crack line loaded
COD	Crack opening displacement
CMOD	Crack mouth opening distance
Cr	Chromium
da/dt	Crack growth
DIC	Digital image correlation
E	Young's modulus
EAC	Environmentally assisted cracking
EBSD	Electron backscattered diffraction
EDM	Electric discharge machining
EDS	Energy dispersive X-ray spectroscopy
EELS	Electron energy loss spectroscopy
EFTEM	Energy-filtered transmission electron microscopy
EPRI	Electric Power and Research Institute
FIB	Focused iron beam

FCC	Face centred cubic
FFT	Fast Fourier Transform
K_1	Stress intensity for mode 1 SCC
K_{10}	Starting stress intensity
K_{1SCC}	Threshold stress intensity
H	Height
HAADF	High angle annular dark field
HAADF STEM	High angle annular dark field scanning transmission electron microscopy
H_2	Hydrogen
H_2S	Hydrogen sulphide
HEAC	Hydrogen environment assisted cracking
HP	High pressure
HRTEM	High resolution transmission electron microscopy
HV	Hardness value
IGSCC	Intergranular stress corrosion cracking
IHAC	Internal hydrogen assisted cracking
IP	Intermediate pressure
IQ	Image quality
LEFM	Linear elastic fracture mechanics
LME	Liquid metal embrittlement
LP	Low pressure
mm	Millimetres
Mn	Manganese
M_f	Martensite finish temperature
M_s	Martensite start temperature
Mo	Molybdenum
NaCl	Sodium chloride

N	Newton
Ni	Nickel
OIM	Orientation image mapping
P	Load
Pa	Pascal
SAD	Selected area diffraction
SEM	Scanning electron microscope
SCC	Stress corrosion cracking
TEM	Transmission electron microscope
V	Vanadium
V_0	Crack mouth opening displacement
W	Width
WOL	Wedge open loading

Contents

List of Figures

List of Tables

1. Introduction

1.1. Background

Steam turbines are utilised in the power generation industry for converting thermal energy from pressurised steam to mechanical energy on a rotating shaft system. The capacity of a steam turbine varies from 150 to 720MW in the South African power generation industry. A typical 600MW steam turbine setup in a coal-fired power station consists of a high pressure (HP), an intermediate pressure (IP), and a low pressure (LP) turbine.

Various corrosion mechanisms exist in power plant steam turbines. These mechanisms depend on the material of construction, the local environment, and stresses applied to the components. The corrosion mechanisms in LP steam turbines include pitting, stress corrosion cracking, corrosion fatigue, erosion corrosion, and flow accelerated corrosion. [4]

Corrosion fatigue and SCC are the leading damage mechanisms in power generation low pressure steam turbine components, and are the primary cause of premature failure of LP steam turbines. [4] Stress Corrosion Cracking (SCC) is the slow, environmentally induced crack propagation of a metal. [5] The susceptible components are turbine blades, disks, rotors, bolts and expansion bellows. The predominantly susceptible components are the LP turbine blades and the disc rim blade attachment areas which are located in the phase-transition zone of the turbine. SCC component failures occur at loads below the design strength of the material. Stress corrosion cracking is a constant concern in this respect in the power generation industry, and thus a comprehensive understanding of the causes and mechanisms of SCC is warranted.

Several factors affect the susceptibility of a component to SCC. These include material factors such as yield strength, compositional variations, heat treatment procedures, the amount of cold work in the material, and the surface condition of the material. [4]

A significant amount of research has illustrated the effect of the heat treatment procedure on the microstructure of low carbon, chromium rich steels. There are well documented metallurgical changes with respect to carbide composition, morphology, and distribution occurring during tempering. [3] [4] [6] [7] [8] In the South African power generation industry the tempering procedure of LP turbine blades has been identified as the root cause for the onset of SCC in a particular investigation. [3] This has led to the requirement to understand the effects of the heat treatment procedure on the SCC behaviour of LP turbine blades.

This research was conducted within the Eskom Power Plant and Engineering Institute (EPPEI) programme. The research is centred in the Materials Specialisation Centre of EPPEI – which focuses on challenges in the power plant materials' discipline.

1.2. Objectives of the research

The study's objectives are to determine the effect of tempering on mechanical behaviour, SCC behaviour and microstructure of 11-13% Cr stainless steel FV566 turbine blades. The focus is on the tempering temperature used and its influence on the SCC mechanism, the crack propagation rates for a given applied stress intensity, and the threshold stress intensity of the material.

Heat treated samples are analysed for microstructural changes, and smooth U-bend specimens are tested for SCC susceptibility. Precracked modified compact tension samples are used to investigate the relationship between stress intensity and crack growth rate – for each heat treatment condition.

1.3. Experimental Approach

The experimental approach of this study comprised heat treatment of specimens by austenitising, quenching, and double tempering at various temperatures. In the power generation industry LP turbines are tempered at 550-650°C. For turbine blades in the Eskom power plants, a tempering range of 580-600°C is commonly used. A tempering range of 480-620°C was therefore chosen for the heat treatment procedure in this study. To determine the effect a marginal change in temperature will have on the material properties, temperature steps of 10°C were chosen.

Various techniques are used to evaluate the effect of tempering on the microstructure, including: light microscopy, scanning electron microscopy, transmission electron microscopy, electron backscattered diffraction, X-ray diffraction, and carbide replica extraction. TEM was carried out on heat treated samples in order to analyse the effect of tempering on the formation and location of precipitates. EDS was used to analyse the composition of precipitates. HRTEM and HRSTEM were used to determine the crystallographic information of certain identified precipitates.

Tensile tests and hardness value testing were undertaken to determine the mechanical behaviour of the heat treated samples.

Smooth un-notched U-bend stress corrosion test specimens were employed to determine the material's susceptibility to SCC. The time taken for cracks to develop and for the sample to fail, was monitored. Samples were analysed using light, SEM imaging, and electron backscattered diffraction (EBSD) – in order to determine the cracking mechanism. EBSD was used to distinguish between

transgranular and intergranular SCC mechanisms. This was achieved with the use of Orientation Imaging Microscopy (OIM) and Image Quality (IQ) maps.

The relationship between stress intensity and crack growth rates was determined according to ASTM E1681(E)-03(2008) [9] using Wedge open loading (WOL) specimens. Compliance equations were used to analyse the stress intensity of the WOL specimens. Crack growth rates were calculated using light microscopy surface imaging.

An aggressive environment was used for the U-bend and WOL specimens to accelerate stress corrosion testing times, and to achieve crack initiation and growth within the time frame of this study. A NaCl environment of 3.5% NaCl solution was chosen for the laboratory SCC testing.

1.4. Scope and limitations of the research

FV566 12-13% Cr stainless LP turbine blades are investigated for changes in mechanical, SCC and microstructural changes – with tempering temperature.

Accelerated SCC testing was used to achieve crack growth within an achievable time frame for the research. As a result, stress intensity versus crack growth relationships could not be determined for all tempering heat treatment specimens. Corrosion product layer formation and post cracking corrosion on specimens, limited analysis of fracture surfaces.

1.5. Plan of development

The dissertation begins with an introduction and with background and study objectives. This is followed by a literature review of pertinent information relating to the study in chapter two. The experimental procedure utilised in the study, are described in chapter three. Chapters four and five present and discuss the results. This is followed by a conclusion and summary in chapter six and recommendations for future work in chapter seven.

2. Literature Review

2.1 Power plants and steam turbines

Coal-fired power stations comprise about 41% of electricity generation capacity worldwide and 93% of the South African-installed generating capacity. [10] South Africa's steady economic growth and electrification program has led to a steep increase in the demand for power. Associated with the increasing demand for energy are primary challenges which affect standard power stations. These challenges are to reduce dust and gaseous emission levels, to lower the cost of electricity, and to ensure availability of power at the time of usage. The reliability of a power plant is a crucial factor in terms of ensuring the availability of power – by preventing unplanned failures and maintenance.

2.1.1. Layout of a coal-fired power station

Chemical energy from coal is converted into electrical energy through a series of processes in a power station. Coal is burnt in the combustion chamber of a boiler, and the heat energy from the burnt coal is used to convert water to high-pressure steam. The high-pressure steam is used to drive a set of turbines and a generator – i.e. the heat energy is converted into mechanical energy. The generator uses an electromagnetic field to convert mechanical energy into electrical energy as seen in Figure 2-1. [10]

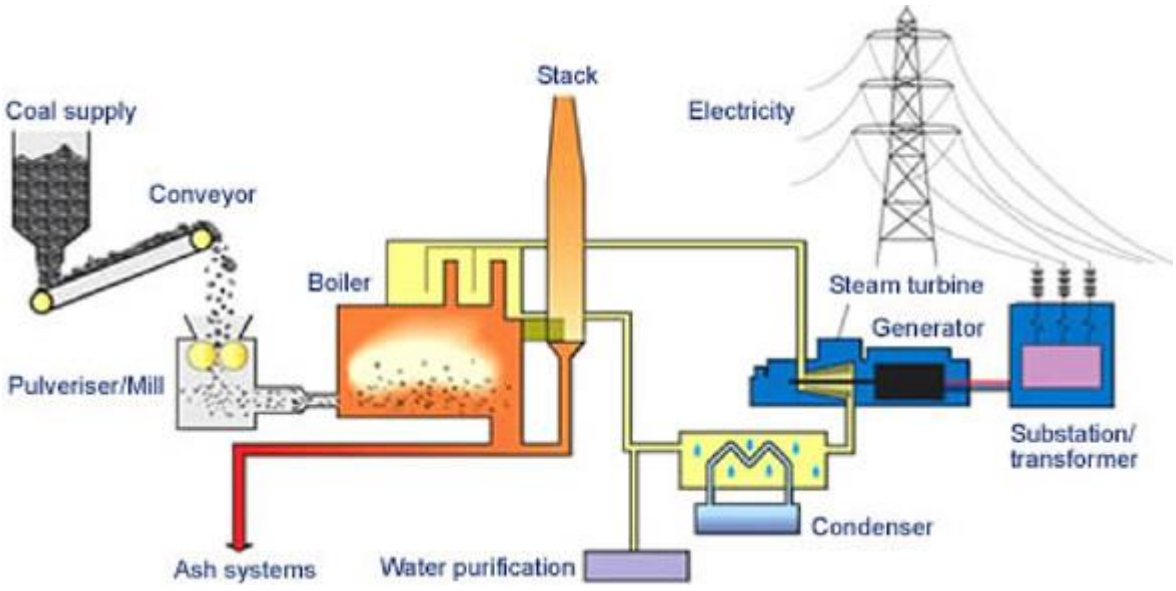

Figure 2-1: Layout of a conventional fossil-fired power station [10]

2.1.2. Steam turbines

The larger output coal-fired power station setup comprises a high pressure (HP), intermediate pressure (IP), and low pressure (LP) turbine. These components are the critical components of the power plant layout, and reliability is essential. Several components of the LP turbines are susceptible to corrosion, and the areas of concern are the blades, disks and rotors. These components have the greatest financial and availability impact on failure [(4).] The region most frequently affected, is the low pressure turbine blades. The environmental condition at the last stage blades of the low pressure turbines, is wet steam. The wet-steam environment renders the last-stage blades susceptible to corrosion, which is not a concern for other components. This research focuses on the LP turbine blades, and the failure mechanism of stress corrosion cracking which results in premature failure of the blades.

The primary materials used for the manufacture of the turbine blades are 11-12% chromium stainless steels, Cr-Mo-V, Ni-Cr-MoV, and primarily martensitic stainless steels. These materials are used due to their high strength and corrosion resistance properties.

Figure 2-2 depicts the distribution of blade failures for the last stage blades of LP turbines in the Unites States. [(4)] The L-1 stage has the most frequent blade failures – followed by the last stage which accounts for 40% and 20% of the total LP turbine blade failures in fossil power plants in USA.

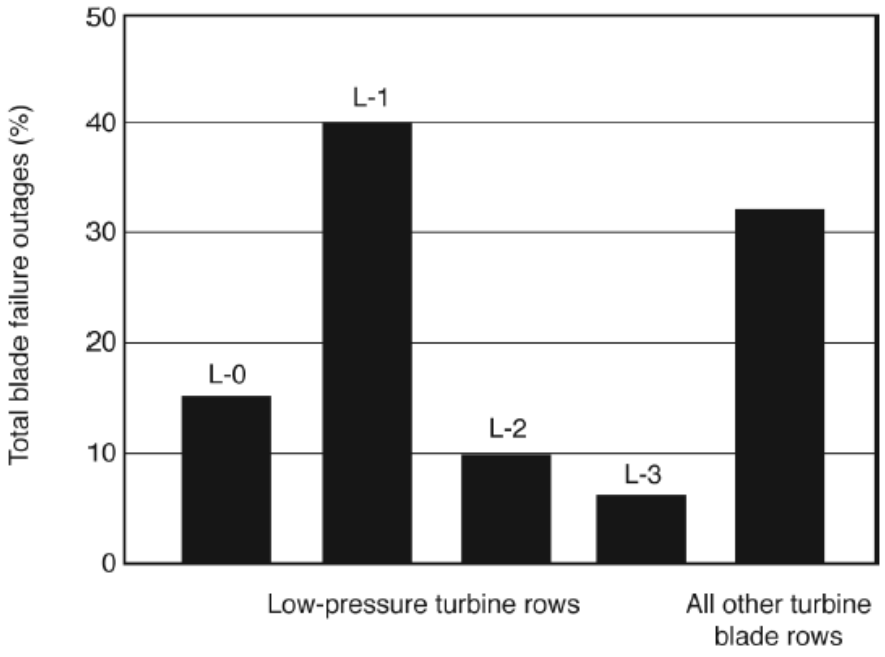

Figure 2-2: Distribution of blade failures by row for fossil-fired power stations in the USA [(4)]

In the South African power utility Eskom, the major causes of turbine blade failures are environmentally induced cracking and fatigue as seen in Figure 2-3. [3] A combination of SCC and fatigue has been a repetitive failure mechanism for the last-stage blades. Failure analysis of these blades has shown the failure mechanism to be transgranular cracking – alternating with intergranular cracking. [11]

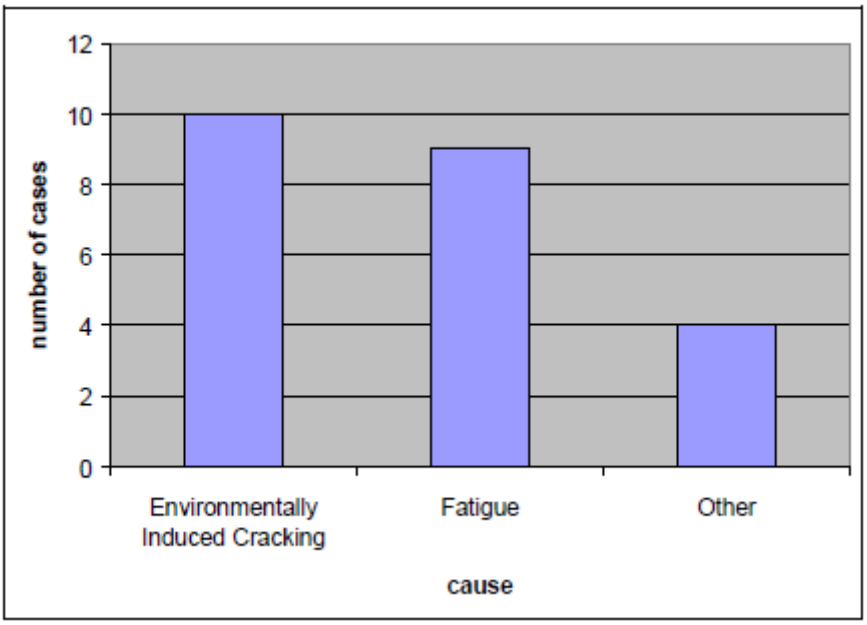

Figure 2-3: Failure statistics for turbine blades in the South African power utility, Eskom [3]

2.2. Stainless steels

Steels and stainless steels are the primary materials used for construction in industry. [12] The production of stainless steel has seen a steady increase from the 1970s through to 2010 (see Figure 2-4).

Stainless steels can be divided into four main categories based on their microstructure:

- ferritic stainless steel;
- martensitic or precipitation hardening steels;
- duplex stainless steel; and
- austenitic stainless steel.

The uses and applications of these steels are based on the desired properties of mechanical strength, manufacturing characteristics, weight, and cost/benefit considerations.

The most widely used stainless steel grades are austenitic Cr-Ni 18-8 type steels, which form 50% of the global production of stainless steels. This is followed by Cr-Ni-Mo austenitic stainless steel, and high-performance steels like duplex stainless steel and martensitic stainless steel.

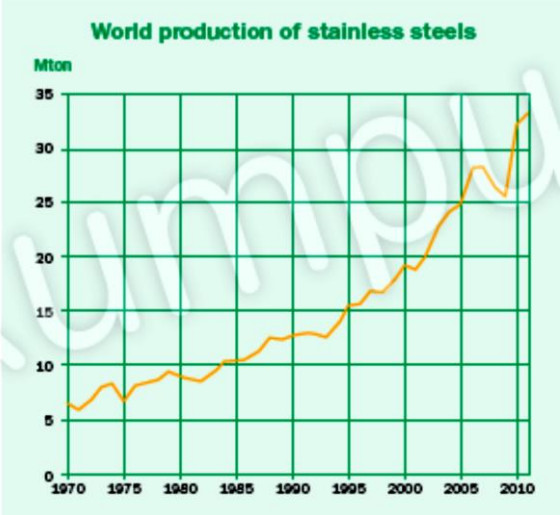

Figure 2-4: World stainless steel production 1970-2010 [11]

Chromium stainless steels are widely used due to their corrosion resistance. Chromium content above 12% additionally provides a substantial amount of oxidation resistance. 12% Chromium stainless steels are largely used in the power-generation industry for corrosion resistance and high temperature applications.

2.2.1. Martensitic stainless steels

Martensite is a supersaturated solution of carbon in iron, which is formed by the rapid cooling of carbon steel after heating [2]. The reaction is a rapid, diffusionless transformation process. Martensite is a metastable phase. During the transformation process, the face-centred cubic (fcc) structure of austenite transforms to body-centred tetragonal (BCT) ferrite. [13] The matrix contains large amounts of lattice distortion, which results in high residual stresses. The BCT crystal structure has no close-packed slip planes in which dislocations can easily move. [2] The high residual stress imparts a high hardness and strength to the material. The high hardenability and brittleness of martensitic stainless however leads to difficulty in machining and fabrication. To overcome this difficulty, these steels are tempered to improve strength, ductility and toughness.

Martensite transformation begins at the martensite start temperature M_s which can differ over a wide temperature range, from as high as 500°C to well below room temperature, depending on the

concentration of γ-stabilizing alloying elements in the steel. Once the martensite start temperature is reached martensite begins to form with further transformation taking place during cooling until reaching the martensite finish temperature M_f.

The structure and properties of the steel depend on the carbon content and alloys. [14] Martensitic stainless steels contain 12-17% Cr, 0-4% Ni, and 0.1-1% C, and are often alloyed with molybdenum, vanadium, niobium, aluminium and copper. Martensitic stainless steels are austenitic at the solution heat treatment temperature of 950°C-1050°C – and transform to martensite on cooling.

2.2.1.1. FV566 12% Cr stainless steel

FV566 is a 12-13% Cr stainless steel used in the manufacture of LP steam turbine blades – due to its high strength and corrosion resistance properties.

The nominal chemical composition of FV566 is listed below.

Material	C	Cr	Mn	Mo	Ni	Nb	P	Si	S	V	Fe
FV566	0.1	12.0	0.61	1.35	2.4	0.28	0.02	0.35	0.01	0.15	Bal
Min	0.08	11.0	0.4	1.0	2.0	0.05				0.05	
Max	0.15	13.0	1.0	2.0	3.0	0.4	0.03	0.6	0.03	0.4	

Table 2-1: Nominal Chemical composition of FV566 [15]

2.2.1.2. Alloying elements in martensitic stainless steels

Alloying elements are often added to improve the tempering resistance, strength, and formability of 12% chromium steels. [16] Alloy elements are added to promote the formation of a particular phase or to stabilise the phase. These elements can be grouped as austenite forming, ferrite forming, carbide forming, and nitride forming elements. [16]

Austenite forming elements

The most significant austenite forming elements are C, Ni and Mn. A high content of these elements render the material austenitic at room temperature. It is therefore necessary to balance the addition of these elements at low weight compositions, or with the addition of other elements.

Ferrite forming elements

The most significant ferrite forming elements are Cr, Si, Mo, W and Al. The Fe-Cr diagram in Figure 2-5 shows the stability of ferrite in chromium containing steels. The elements (Mb, V) tend to produce delta ferrite in the matrix at the solution heat treatment temperature of 1050°C, delta

ferrite lowers the strength of the material considerably. These elements are therefore balanced with the austenite forming elements mentioned above to ensure a fully austenitic structure around 1050°C, and resulting in a fully austenitic temperature upon cooling and tempering.

A higher carbon content also decreases toughness, and impairs corrosion resistance and weldability. Nickel is the best austenite former after carbon. Cobalt is also often used as it decreases the likelihood of delta ferrite formation (ɣ) and does not depress the martensite (M_s) start temperature. The carbon content of these steels is limited to 0.1%C. [17]

Carbide forming and stabilising elements

Most ferrite forming elements are also carbide forming elements. The affinity of the elements for carbon listed below, increase from left to right: [16]

Cr, W, Mo, V, Ti, Ta, Zr

Carbides which commonly form in 12% chromium steels, are M_6C, $M_{23}C_6$ and MC. The vanadium carbides are commonly VC and V_4C_3. The stability of the carbides depends on the presence of the other elements in the matrix. The Gibbs free enthalpy or the various carbides are shown in Figure 2-6. [18]

Nitride forming elements

Carbide forming elements are also nitride formers. CrN , Cr_2N, FeN and Fe_4N are common nitrides. [19] Nitrogen may be introduced on the surface of the steel by nitriding. Nitriding is a hardening technique to strengthen steels. [19] Stainless steels are nitrided with a special heat treatment due to the chromium oxide which forms as film on the surface of the steel. [16] This film prevents nitrogen absorption. Nitriding of stainless steel is not favourable as the chromium oxide layer which imparts the corrosion resistant properties to stainless steel is removed. Ni is not a nitriding element

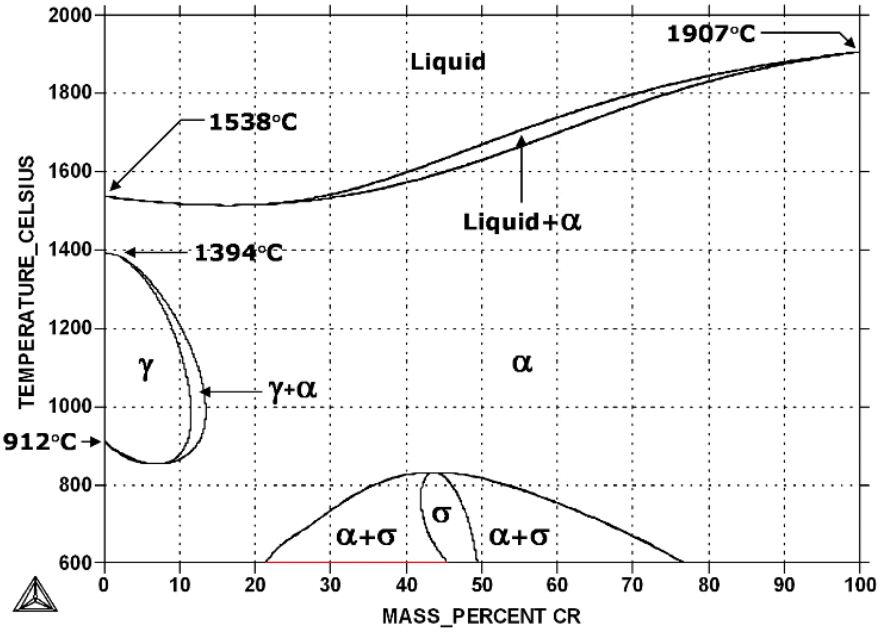

Figure 2-5: Cr-Fe equilibrium diagram [20]

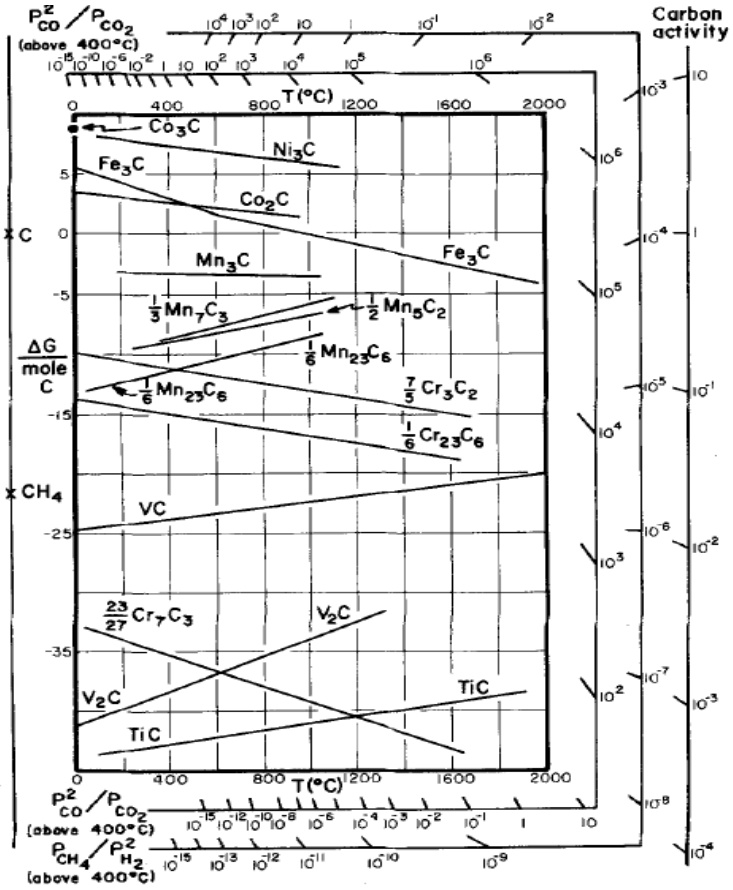

Figure 2-6: Ellingham diagram for the first transition series carbides. The formation of the lowest compound formed from the metal upon reaction with 1 mole of C is denoted only by the compound MxC. [18]

2.2.1.3. *Heat-treatment properties of martensite*

Tempering of martensitic stainless steels

Martensite is not an equilibrium phase and does appear on the Cr-Fe equilibrium diagram Figure 2-5. Martensite which forms after rapid cooling from austenite, has a high amount of lattice distortion with carbon atoms trapped in the matrix. Tempering is a heat treatment which replaces the solid solution strengthening of the dissolved carbon – with precipitation strengthening by carbides. Tempering improves the ductility, impact toughness and stress corrosion cracking properties. [16] Tempering is achieved by the controlled heating of a material below the lower transformation temperature A_{c1}. The A_{c1} temperature is the temperature at which the crystalline phases of the alloy begin to form a single phase of austenite.

Tempering and the time at tempering temperature have a significant influence on the type, size and morphology of carbide precipitates. Porter and Easterling [21] summarised the various changes which occurred during tempering for ferrous martensites up to a tempering temperature of 700°C shown in Table 2-2 .

Porter and Easterling showed that tempering between 250-350°C may result in the formation of lath like Fe_3C precipitates. The authors also showed tempering at 500-600°C for the chromium steels results in the formation of alloy carbides and secondary hardening and additionally the dissolution of Fe_3C.

Secondary hardening due to the precipitation of alloy carbides may increase the hardness of the steel during tempering. In high alloy steels a precipitation of finely dispersed complex carbides occurs at approximately 500°C. [16]

Figure 2-7 shows the relationship between tempering temperature and hardness value. Pickering et al. [22] showed an increase in hardness up to tempering temperatures of 500°C. This is followed by a pronounced softening. Pickering et al. postulated this pronounced softening at temperatures greater than 500°C due to the formation of Cr_7C_3 precipitates and M_2X precipitates. Tempering above 550°C of alloyed 12%Cr martensitic steels results in the formation of $M_{23}C_6$ which results in further softening of the material.

Temperature (°C)	Transformation	Remarks
25-100	Carbon segregation to dislocation; pre-precipitation clustering	Clustering predominant in high carbon steels
100-250	Epsilon-carbide precipitation (first stage of tempering)	May be present in low carbon low alloy steels
200-300	Retained austenite transforms to bainite (second stage of tempering)	Occurs only in medium and high carbon steels
250-350	Lath like Fe_3C precipitation (third stage)	
400-600	Recovery of dislocation substructure. Lath-like Fe_3C agglometrates to form spheroidal Fe_3C	Lath structure maintained
500-600	Formation of alloy carbides (secondary hardening or fourth stage)	Occurs only in steels containing Ti, Cr, Mo, V, Nb, or W; Fe_3C may dissolve
600-700	Recrystallation and grain growth; coarsening of spheroidal Fe_3C	Recrystallisation inhibited in medium carbon and high carbon steels, exquiaxed ferrite formed

Table 2-2: Changes which occurred during tempering for ferrous Martensite up to a tempering temperature of 700°C [21]

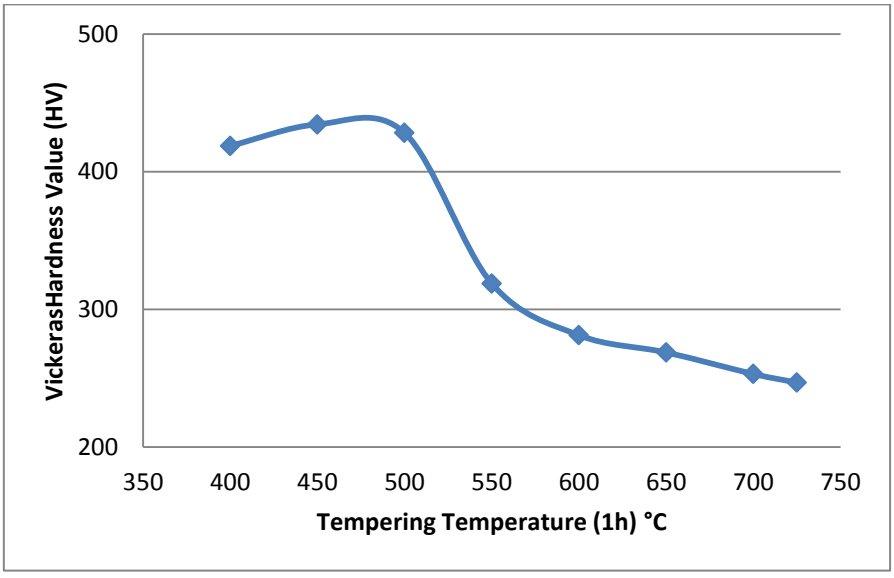

Figure 2-7: Vickers hardness value as a function of tempering temperature for unalloyed 0.1C-12Cr stainless steel [17]

Figure 2-8 shows the effect of tempering on impact resistance for various 12% Cr steels. A minimum impact resistance is observed at tempering temperatures in between 400-500°C.

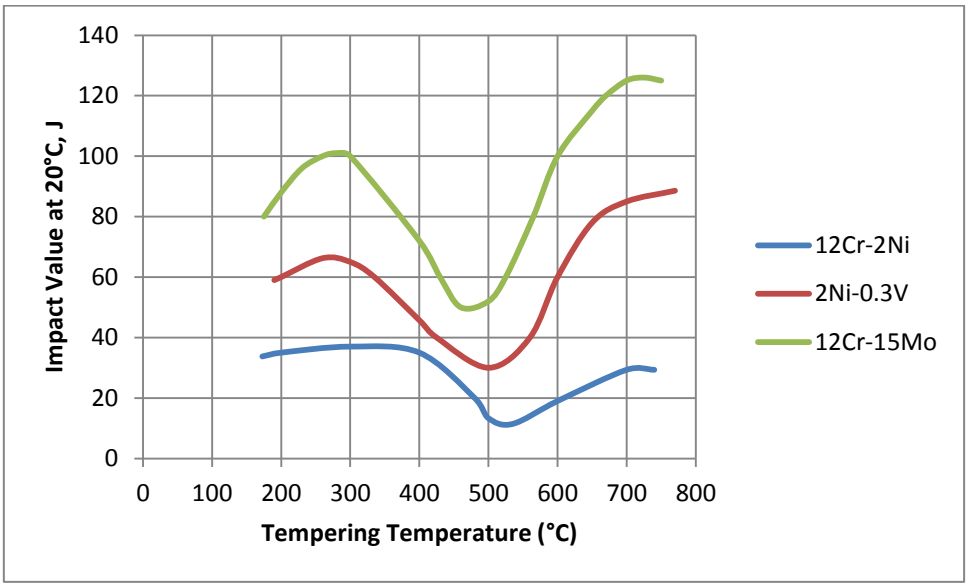

Figure 2-8: Effect of tempering on impact resistance for various 12% Cr stainless steels [17]

The effect of tempering temperature on the tensile strength and proof strength for 12% Cr stainless less with varying carbon content is shown in Figure 2-9. The ductility of the steel increases with tempering temperature.

The accompanying changes in the microstructure of 0.1C-12% Cr steel are seen in Figure 2-10. [17] Tempering at 300°C for 1 hour produces a predominately martensite microstructure with small particles of Fe_3C. Tempering at 450°C and 500°C produces a fine matrix precipitate seen in Figure 2-10 (b & c).

The hardness of 12% chromium steels has been observed at a minimum tempering temperature of 300-350°C. [22] At this temperature there is an increase in the precipitation of Fe_3C carbides. The associated reduction in hardness is due to the removal of carbon from the matrix solution during precipitation. The original Fe_3C precipitates re-dissolve during the formation of matrix precipitates. Tempering at 500°C for longer periods results in the formation of a larger amount of fine matrix precipitates and the re-dissolving of Fe_3C. The fine precipitates were identified by Irvine et al. as Cr_7C_3. [23] Irvine et all showed that apart from the separate nucleation of Cr_7C_3 there is transformation of Fe_3C to Cr_7C_3 and this causes small rods to form as shown in Figure 2-10 b and c.

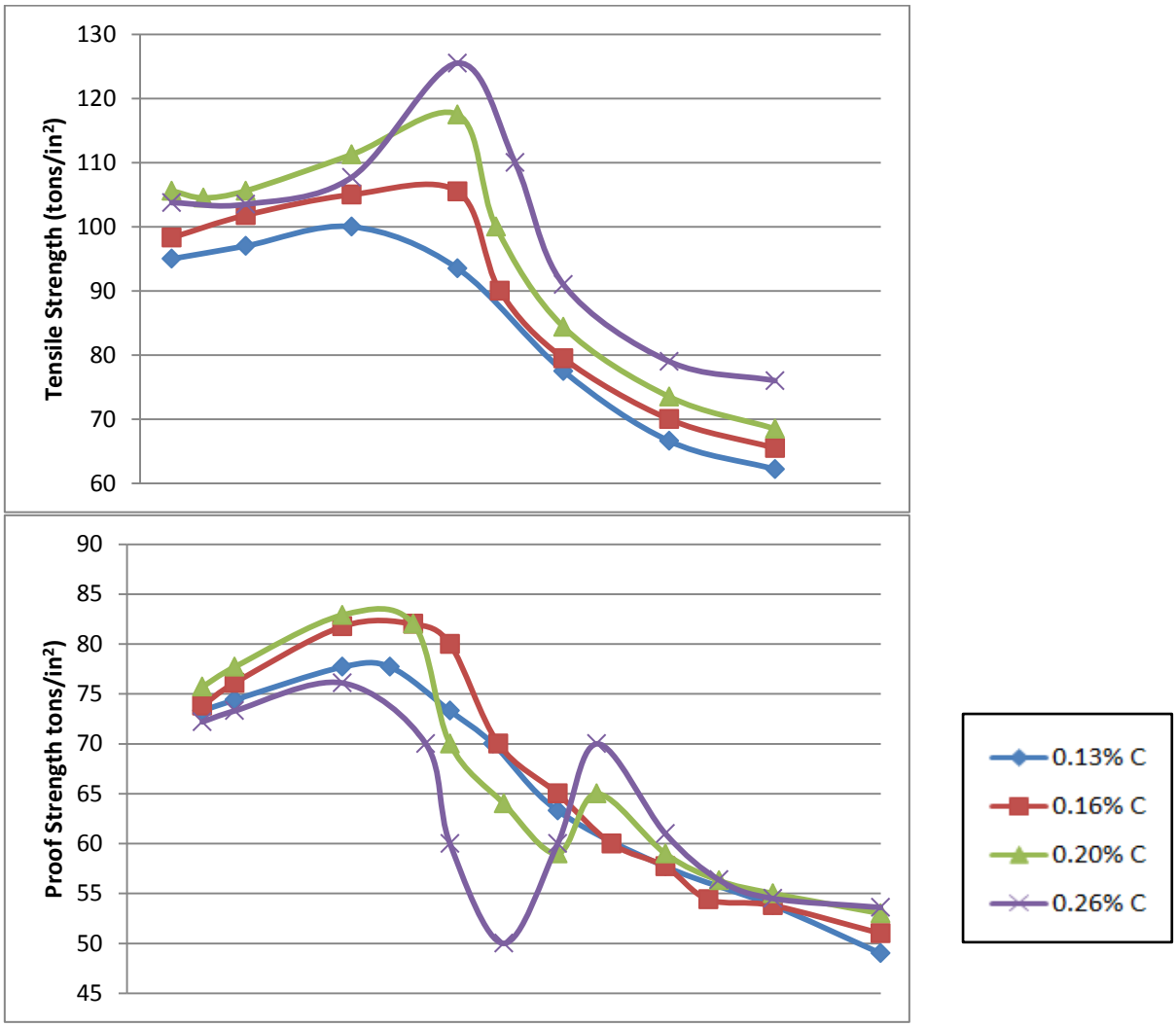

Figure 2-9: Effect of carbon content and tempering temperature on the mechanical properties of 12% Cr, 2% Ni, 1.5% Mo-V steel, tempered for 1 hour - a)tensile strength; b)proof strength [17]

Particles of M_2X were additionally identified to be present in the matrix. The M_2X carbide was identified as Cr_2C. Increasing the Mo and V alloying elements stabilises the preference of M_2X over Cr_7C_3. Due to the crystallographic structure of M_2X, M_2X can dissolve large amounts of alloying elements which causes a secondary hardening peak which is stabilised over a wide tempering range.

Irvine et al. noted tempering at 500°C and higher the formation of relatively large carbide particles are formed at martensite plate and austenite grain boundaries. These were identified as $M_{23}C_6$. As the tempering temperature increase the further precipitation of $M_{23}C_6$ occurs at the expense of Cr_7C_3. With further tempering this results in coarsening of the precipitates. Consequently the secondary hardening peak and hardness of the steel is removed.

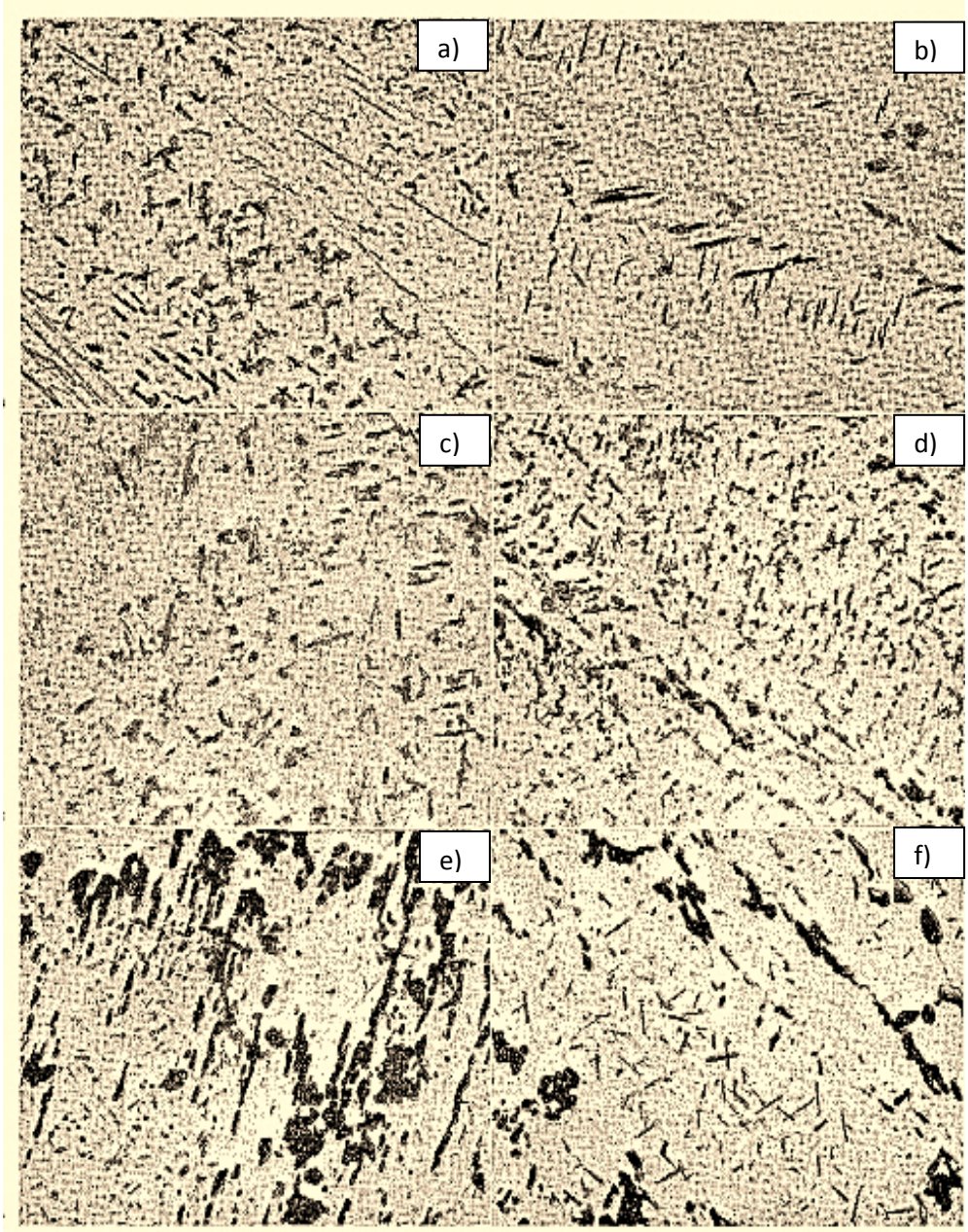

Figure 2-10: Electron micrographs of a 0.1C-12% Cr steel tempered at: a) 300°C for 1 h; b) 450°C for 240 h; c) 500°C for 8 h; d) 500°C for 240 h; e) 600°C for 8 h; f) 700°C for 1 h (magnification – 15000 X) [17]

Double tempering

At the martensite finish temperature all the austenite present in the matrix should have transformed to martensite but frequently in practice, a small portion of the austenite remains untransformed even at low temperatures. Large volume fractions of austenite can be retained in some highly alloyed steels, where the M_f temperature is well below room temperature. A double temper heat treatment is often used to overcome this problem. [24]

Double tempering produces a combination of mechanical properties which cannot be achieved from single tempering.

During service operation the steel may be exposed to temperatures between 200°C-500°C for extended periods. Irvine and Pickering [25] concluded the typical tempering temperature used for 12% chromium steels has been 650°C for one hour. Large particles of $M_{23}C_6$ with a small amount of matrix precipitates of M_2X are produced from this heat treatment. For 12% chromium steels the possibility of in service temperatures between 250-500°C are extremely high [25]. A double temper heat treatment is often therefore used to impart the steel with a combination of mechanical properties.

Irvine and Pickering investigated the double tempering heat treatment of a 12%Cr-Mo-V type steel. The steel was austenised at 1050°C, air cooled, tempered at 650°C for 4 hours followed by 400°C and 475° for various times. It can noted the first tempering heat treatment was at a higher temperature than the second heat treatment. The 0.2% proof stress of a single heat treatment of 650°C is approximately 689.48MPa whereas the 0.2% proof stress was increased by an average of 50MPa as seen in Table 2-3 and Figure 2-11. Irvine and Pickering [25] carried out the same tests but with longer tempering durations for the second temper treatment shown in Table 2-3. The 0.2% proof strength was increased by 165MPa [25]. Irivne and Pickering postulated this change in proof stress was due tempering at 650°C which leaves some carbon remaining in the solution which is in excess of the solubility limit at 400°C. When the steel is tempered at 400°C the excess carbon precipitate as a carbide which is stable at this temperature. For the 12%Cr-Mo-V steel this is M_2X.

The literature on FV566 is limited and only a few sources on SCC have been cited. [3] [6] [8] [22] [23] [10] [24]

Tensile properties obtained by double tempering								
Austenitising at 1050°C AC, Tempering 675°C (4 h) and Tempering as listed below								
MPa	400 (1h)	400 (1h)	400 (10h)	400 (16h)	400 (25h)	475 (1h)	475 (5h)	475 (10h)
TS	830.13	834.27	835.64	848.06	848.06	852.19	842.54	853.57
0.2% PS	722.57	728.09	729.47	740.50	746.01	746.01	739.12	750.15
0.1% PS	701.89	707.40	708.78	723.95	729.47	729.47	721.19	735.36
0.05% PS	674.31	681.20	683.96	703.27	707.40	707.40	700.51	717.05
0.02% PS	639.83	650.87	650.87	670.17	670.17	670.17	668.79	685.34
Elongation, %	24.9	23.8	28.8	24.3	23.8	23.8	24.9	23.6

Table 2-3: Tensile properties obtained from double tempering [17]

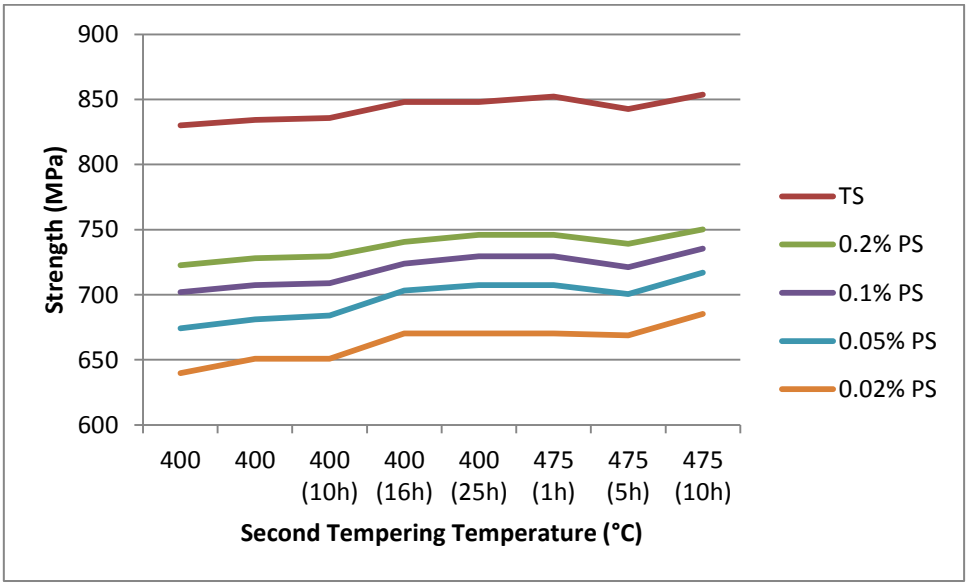

Figure 2-11: Tensile Properties of obtained by double tempering [17]

The transformation temperatures of FV566 are listed in Table 2-4:

Transformation temperatures of FV566 (°C)	
On heating at (139°C/hr)	
A_{c1}	750
A_{c3}	800
On cooling from 1000°C	
M_s	345
M_f	50

Table 2-4: Transformation temperatures of FV566 [26]. The M_f temperature was not determined experimentally and the value shown is from the material data sheet [15]

2.3. Corrosion

Corrosion is defined as the deterioration of materials due to reactions with their environments. [28] There are several general mechanisms by which the corrosion process takes place.

Various corrosion mechanisms exist in power-plant steam turbines. These depend on the material of construction, local environment, and stresses applied to the components. The corrosion mechanisms in LP steam turbines include pitting, stress corrosion cracking, corrosion fatigue, erosion corrosion and flow accelerated corrosion.

2.3.1. Pitting

Pitting is a mode of localised corrosion of a material and is typically associated with active–passive type alloys under environmental conditions specific to each material. Passivity or passivation is defined as a condition of corrosion resistance due to the formation of a thin surface film under oxidising conditions. [28]

The two main theories for passivity are the Oxide Film Theory and the Adsorption Theory for Passivity. [29] The oxide film theory attributes the improved corrosion resistance to the formation of a protective layer or film on the metal's surface. The adsorption theory postulates that the chemiabsorbed film displaces the normally adsorbed water molecules and slows down the rate of anodic dissolution involving the hydration of metal ions. [29]

A metal active in the EMF series, or an alloy composed of such metals, is considered passive when its electrochemical behaviour becomes that of an appreciably less active or noble metal. [30] Passivity is displayed by chromium from the formation of a highly adherent and very thin oxide film on the metal surface – which serves as a protective barrier to further corrosion. [28]

The electrochemical potential of a metal is an important factor in the pitting susceptibility of a metal. [4] The corrosion reaction involves the transfer of electrons and ions between the metal and the solution, and the rate of transfer is equivalent to electric currents. [31] The rate of the chemical reaction depends on the potential difference between the metal and the environment. As the potential difference becomes more negative, the cathodic reaction between the metal and the environment increases. As the potential difference becomes more positive, the anodic reaction increases. [31] The relationship between the potential difference and current is plotted as a polarisation curve. The current is indicative of the corrosion rates at the potential difference of the metal and the environment.

Chromium alloys display an active-passive behaviour in aqueous solutions, and an S-shaped polarisation curve – as seen in Figure 2-12 below.

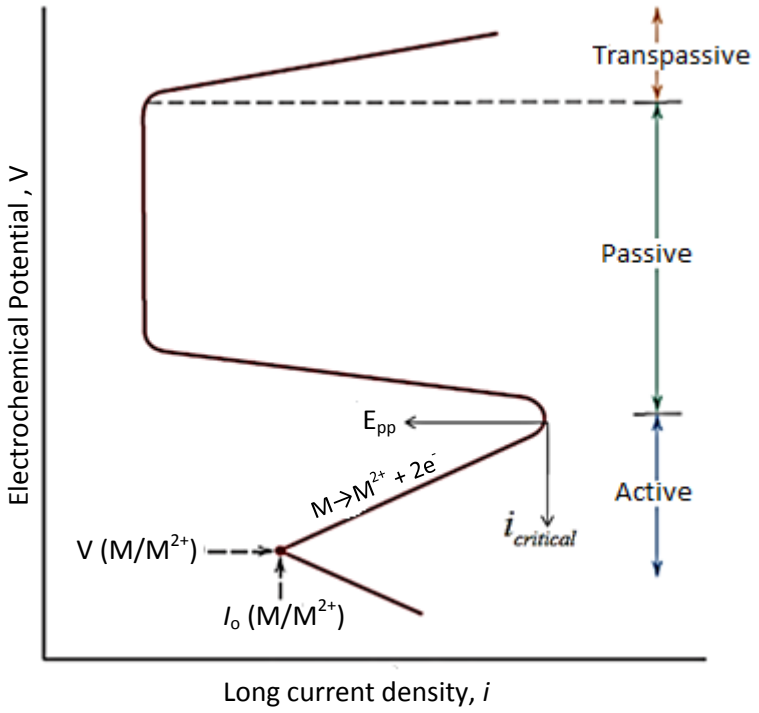

Figure 2-12: Pentiostatic polarisation curve for stainless steel [31]

For the theoretical polarisation curve shown above, the following key parameters should be noted: [31]

- Passive Potential (E_{pp}) is the potential of an electrode where a change from an active to a passive state occurs.
- Flade potential (E_F) is the potential at which a metal changes from a passive state to an active state.

- Transpassive potential is the potential corresponding to the end of a passive region which corresponds to the initial point of anodic evolution of oxygen. This may correspond to the breakdown electrolysis voltage of water or the pitting potential.
- Critical current density ($i_{critical}$) is the maximum current density observed in an active region for metal or alloy, that exhibits an active–passive behaviour.
- Passive current density (i_p) is the minimum current density required to maintain the thickness of film in the passive range.
- Pitting potential is the potential at which there is a sudden increase in the current density, due to breakdown of passive film on the metal surface in the anodic region.

Chromium alloy steels form a passive layer at much lower potential difference (E_{pp}). The transpassive layer for chromium steels occur at a high potential difference compared to unalloyed iron.

Pits are initiated by penetration of the local passive film by pre-existing conditions. The breakdown of the film may be by a chemical or mechanical process. The passive films can break down in the presence of impurities like chlorides and sulphates in the environment. [4] A high concentration of impurities in the passive film can lead to general corrosion and the formation of a pit. The base of the pit is now an anode – which leads to further corrosion of the metal surface.

Pitting growth rates decrease with time. [4] For pits to propagate, anodic and cathodic electrochemical reactions need to be continued. In an oxygen-rich environment oxygen is readily available to maintain cathodic reactions – hence the spacing of the pits is denser. In an oxygen-limited environment the formation of pits on the metal surface is less dense. [4]

In the presence of a tensile stress, corrosive environment, and susceptible material, a pit can propagate into a crack. In statically loaded cases this can lead to SCC – and in dynamically loaded cases to CF.

2.3.2. Corrosion fatigue

Corrosion fatigue is the combination of corrosion and fatigue in a metal, under the action of an aggressive environment and a cyclic stress, and which results in plastic deformation of the material and crack initiation. The crack propagates under a fatigue stress, as there is a concentrated stress at the crack tip. Corrosion aggravates the crack propagation at the crack tip. In the steam turbine application – there are both static and cyclic stresses. [4]

2.3.3. Erosion and erosion corrosion

Erosion and erosion corrosion are the mechanical wear of a material. [4] Impurities in the environment can cause surface damage to a material. For brittle materials, the impurities may cause chipping of the metal surface and material removal. For soft metals, the result is plastic deformation with the possibility of material removal; his leads to sites of localised stress concentrations. In a corrosive environment, the result is erosion corrosion. Corrosion aggravates the wear on the metal surface. In LP steam turbines, erosion corrosion is caused by water droplets or solid particle impingement. The stress concentration initiated during erosion and erosion corrosion can lead to CF or SCC – depending on loading conditions.

2.3.4. Stress corrosion cracking (SCC)

Stress corrosion cracking falls under a branch of corrosion known as Environmentally Assisted Cracking (EAC). This refers to any cracking of metal in a chemical environment. [32]

The four main types of EAC are: [32]

- Stress corrosion cracking;
- Corrosion fatigue;
- Liquid metal embrittlement; and
- Hydrogen embrittlement.

2.3.4.1. Definition of SCC

SCC is defined as the slow, environmentally induced crack propagation of a metal. [33] For SCC to occur, the following three requirements need to be present:

- An applied tensile stress or residual stress;
- A corrosive environment; and
- A material that is susceptible to SCC.

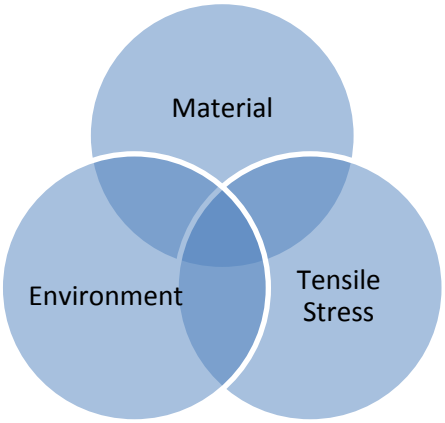

Figure 2-13: Stress corrosion cracking [5]

SCC produces a marked loss of mechanical strength – with a small amount of metal loss. SCC cracking behaviour is described in terms of the stress intensity factor and crack growth rate. The stress intensity factor describes the stress state at a crack tip, and is used to establish failure criteria due to fracture.

2.3.4.2. SCC mechanisms

The SCC mechanism for each material and environment combination is different. Variations in chemical compositions, internal strain, and electrochemical potential differences within the microstructure, lead to different SCC mechanisms.

SCC mechanisms can largely be classified as anodic (e.g. active path dissolution) and cathodic (e.g. hydrogen embrittlement , strictly a EAC mechanism).

Film rupture mechanism

Environmental conditions promote the formation of a passive film on the metal surface. The passive film ahead of a crack tip is ruptured by an initial applied stress. The exposed metal is subject to anodic dissolution – and the crack propagates. The environmental conditions support re-passivation of the metal surface. The applied stress ruptures the film formed, and then the process repeats.

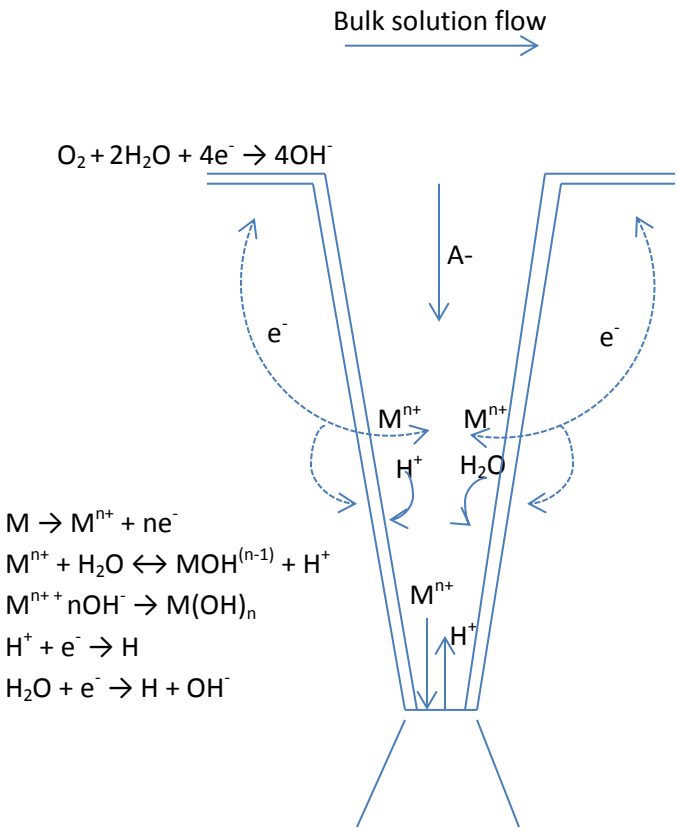

Figure 2-14: Passive film breakdown and anodic dissolution on the metal surface [4]

Active path corrosion

Compositional differences in the microstructures cause accelerated corrosion along a path which is more susceptible than the bulk material. The energy associated with grain boundaries make the material favourable for solute segregation and precipitation reactions. This increases the susceptibility to localised corrosion. [33] Compound precipitates which are anodic with respect to the surrounding matrix along a grain boundary dissolve preferentially – and the applied stress acts to tear ligaments of remaining grain boundary material. Sensitisation of stainless steel due to chromium carbide formation and depletion of Cr adjacent to the grain boundaries, is an example of active path corrosion.

Corrosion Tunnel Model [34]

Corrosion tunnels are formed by active corrosion. Dissolution of metal in the tunnels leads to fracture of the dissolved regions by ductile overload. Crack growth takes place until the crack tip is plastically blunted, and the process will continue. In many cases this occurs by a slip in the alloy and results in the exposure of unfilmed metal at the slip step.

Film induced cleavage [34]

If a brittle layer forms on a crack during corrosion, it can inject a microcrack into the substrate before being arrested. Due to the corrosion process, the brittle film can form again after the microcrack is arrested – and the process will continue. The cleavage process is initiated by dealloying.

Hydrogen embrittlement [32]

Hydrogen embrittlement is a form of environmentally-assisted cracking, which acts to embrittle a material. It differs from anodic SCC, in that the reaction is cathodic. The introduction of atomic hydrogen in a metal can significantly reduce the ductility and toughness of a material.

Atomic hydrogen diffuses interstitially through a metallic crystal, and at grain boundaries. Hydrogen atoms reduce the cohesive bond strength between metal atoms – thereby enabling the fracture process of a metal.

Hydrogen embrittlement is divided into two main categories:

- Hydrogen environment assisted cracking (HEAC); and
- Internal hydrogen assisted cracking (IHAC).

The two categories are based on the source of hydrogen for the embrittlement process.

For hydrogen embrittlement, a high triaxial stress near the crack tip is available. This stress causes the crystal lattice at the crack tip to expand – and increases the solubility of hydrogen at the crack tip. The increased concentration of hydrogen in the crack-tip zone causes the area to be embrittled, as depicted in Figure 2-15 below. Due to this embrittlement, and combined with the high local applied stress, microcracking is initiated at the crack tip area. The crack propagates as the local crack tip is embrittled by hydrogen, and the process continues. The microcracks propagate and join the existing cracks in a material.

IHAC takes places when dissolved hydrogen is present in a material. Hydrogen can dissolve into a material at elevated temperature, if the material is exposed to hydrogen – e.g. H_2S gas. Cooling of the material to ambient temperature results in diffusion of hydrogen from the material. The diffusion rate will depend on the rate of cooling and thickness of the material. Hydrogen will diffuse interstitially in a material ahead of an existing crack or flaw, so accelerating the fracture process.

HEAC involves hydrogen entering the material at the crack tip. H_2 molecules disassociate either from a gas, the electrolyte or water vapour to form atomic hydrogen s at the crack tip when;

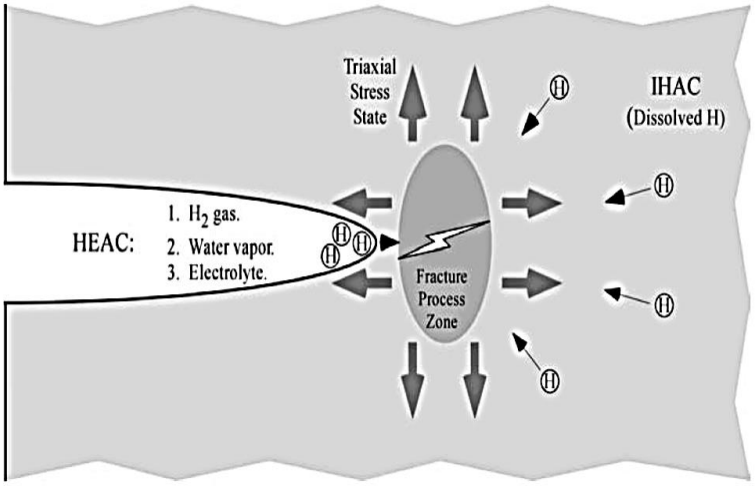

Figure 2-15: EAC driven by hydrogen embrittlement [32]

The factors which affect the hydrogen embrittlement cracking behaviour, are loading rate and history, temperature of the environment, strength of the material, and the amount of hydrogen available for the reaction. [33]

2.3.4.3. Sensitisation of stainless steel as a SCC mechanism

Grain boundary chemistry has been acknowledged as a primary factor affecting intergranular stress corrosion cracking and intergranular attack. [35] The term sensitisation refers to refers to breakdown in corrosion resistance of a material due to the depletion of chromium adjacent to the grain boundaries and precipitation and growth of chromium rich carbides. [36] Heat treatment of stainless steels can result in sensitisation by the formation Cr depleted zones adjacent to grain boundaries by precipitation of chromium carbides. [37] The effect of the carbide distribution and the influence on stress corrosion cracking has been investigated by several authors, [36] [38] [39] who have shown that the precipitation of chromium carbides influences the stress corrosion behaviour of the material.

The depletion of chromium is controlled by the thermodynamics of carbide formation and difference in diffusivities of the chromium and carbon. During the carbide precipitation, interstitial carbon diffuses rapidly to the grain boundaries, but diffusion of chromium is comparatively much slower and this results in depletion of chromium at the grain boundaries. [36] The material which contains areas of chromium depletion is referred to as sensitised; in this state the material is susceptible to intergranular stress corrosion cracking.

The precipitation of chromium-rich carbides at grain boundaries leads initially to the formation of a chromium depleted zone in the matrix next to the grain boundary. [38] This is depicted in Figure 2-16. The carbides can form as discrete isolated particles or as semi-continuous or continuous sheets depending on the heat treating conditions. [35] Several studies have shown the onset of sensitisiation with the presence of carbides at grain boundaries. [36] [35] [40] [37] [41] [42]

Yanliang et al used atomic force microscopy (AFM) to study sensitization by identifying carbides at grain boundaries in the heat affected zone of a AISI 304 martensitic stainless steel weld. [40] Figure 2-17 shows the AFM micrographs of six samples heated at 700°C for different periods. [40] Yanliang measured the width of the grain boundary carbides and the length the carbides occupy at the grain boundaries, and calculated the ratio of the occupancy. This was then used to evaluate the sensitisation to some extent quantitatively which is shown in Table 2-5.

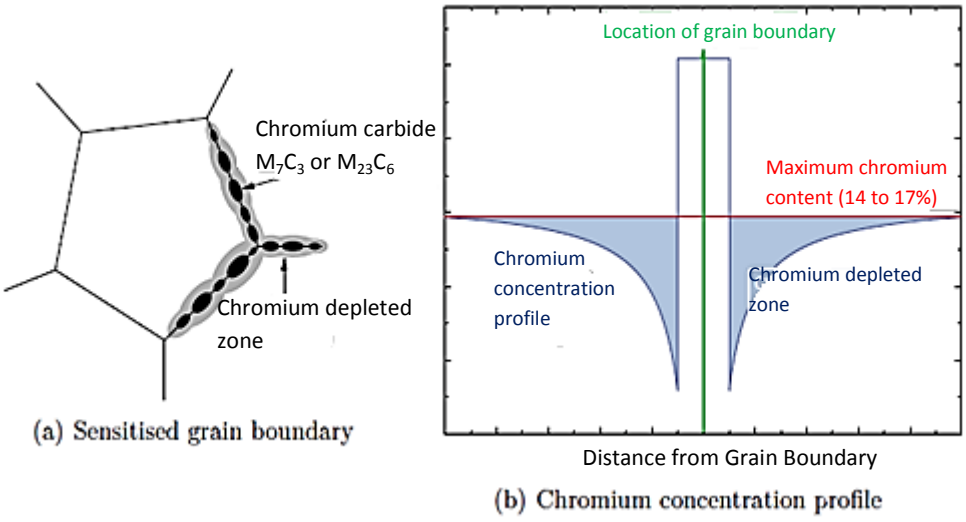

Figure 2-16: Schematic representation of chromium depleted zone of alloy 600 [36]

Yanliang found the size of the carbides increased with the increase of heat treatment duration, and the nodules of the carbides become almost continuous along some boundaries, indicating severe degree of sensitisation. This showed that the heat treatment and duration has a direct impact in the formation of chromium rich precipitates at the grain boundaries resulting in a sensitised material.

Hall et al [36] showed significant chromium depletion at grain boundaries in the vicinity of carbides for samples aged at 50 and 100 hours at 650°C and 100 and 300 hours at 700°C with lower grain boundary chromium values observed at 650°C than at 700°C for 361LN stainless steel. The carbides identified were $M_{23}C_6$. Hall et al showed the carbide distribution was not uniform but varied between grain boundaries possibly as a result of grain boundary misorientation.

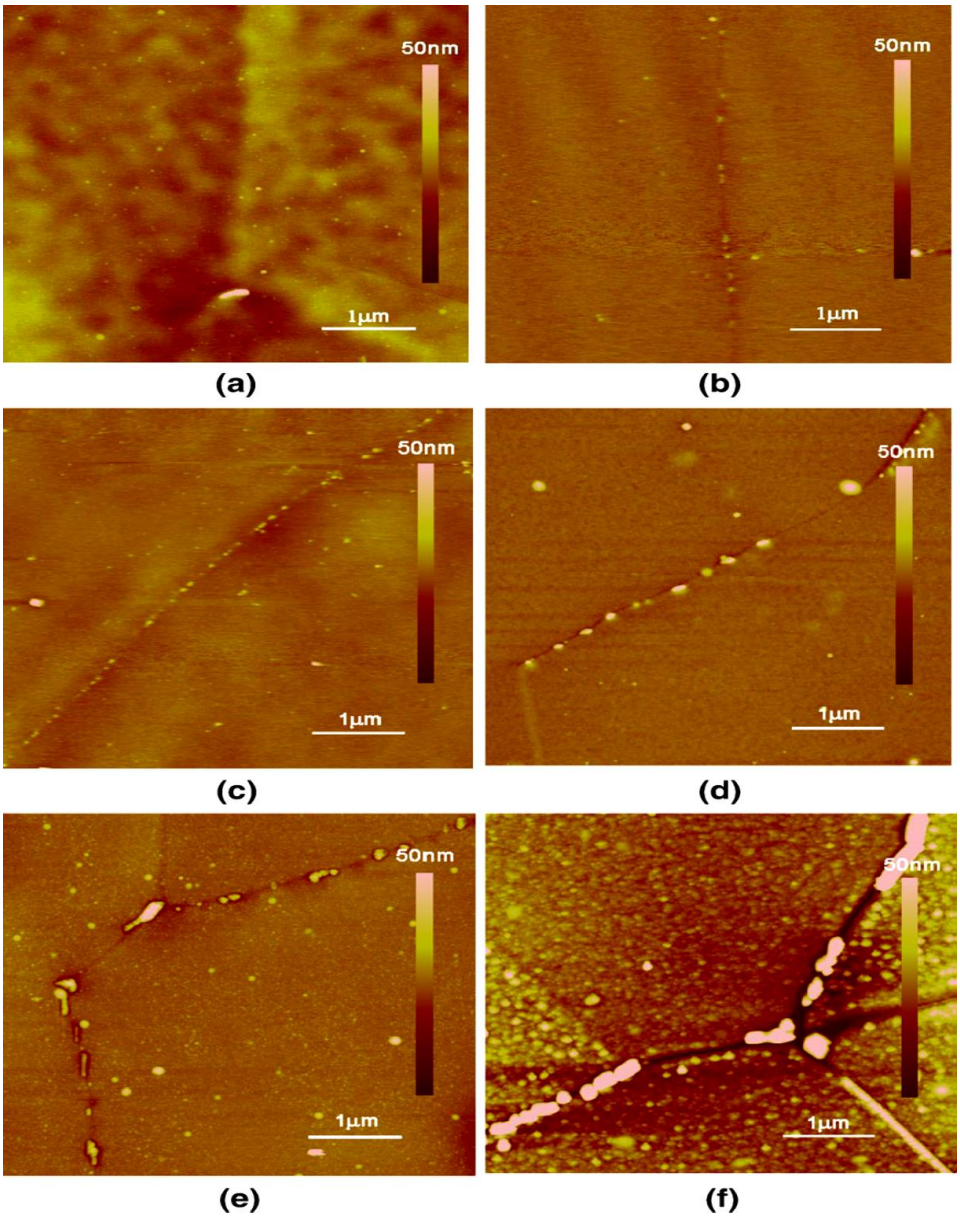

Figure 2-17: AFM images of the electrochemically etched sample surfaces. From (a) to (f), samples were heat-treated at 700 °C for 5, 15, 30, 60, 300 and 600 min [40]

Sample number	A	B	C	D	E	F
Number of carbides		10	22	17	23	17
Characteristics of carbides		Small	Small	Medium	Large	Large, continuous nodules
Measured length of grain boundaries	7.8	5.2	7.2	6.4	8.1	10.3
Number of carbides per 10µm grain boundaries		1.9	3.1	2.7	2.8	1.7

Table 2-5: The number of carbides along measured length of grain boundaries - (A) to (F), samples were heat-treated at 700 °C for 5, 15, 30, 60, 300 and 600 min [40]

Figure 2-18 shows the chromium profile normal to grain boundaries in the vicinity of carbides. In the vicinity of the carbide the chromium percentage is less when compared to the bulk material chromium profile. As the distance from the grain boundary in the vicinity of the carbide increases the chromium percentage increases. [36] This indicates the material is sensitised at the grain boundary in the area of the precipitates.

Stawstrom and Hillert [43] proposed that stainless steel is susceptible to corrosion only when a zone of less than approximately 13 percentage Cr and of width greater than 20 nm existed at the grain boundaries. Stawstrom and Hillert also postulated the corrosion properties of the material can be returned after prolonged heating the temperature range which the material was initially sensitised at. They referred to this process as "healing". They found that healing could be attributed for by the increase in matrix chromium content at the carbide-matrix interface caused by changes in the carbon activity in the steel. Their model has significant deficiencies and did not account for grain boundary misorientation and the associated chromium distribution.

The process of healing of stainless steels with prolonged duration at a particular temperature and increasing temperature have been supported by Tavres and Mayo. [44] [35]

Tavres et al. [44] studied the intergranular corrosion behaviour of Ph14 – a 17% Cr steel commonly used in power-generation applications. Tavres et al. also showed that specimens which are heat treated at 495°C exhibited sensitisation and intergranular SCC. Increased tempering temperature results in a greater quantity and number of precipitates by diffusion of chromium from a point further away in the material – so restoring the material's stainless properties at the grain boundaries.

Chial et al. investigated the electrochemical properties of 15Cr17Ni2 and noted a decrease in the material's sensitisation at tempering temperatures above 550°C. [45] They concluded that tempering at 400-600°C results in the sensitisation and embrittlement of the stainless steel due to precipitation of $M_{23}C_6$ chromium-rich precipitates.

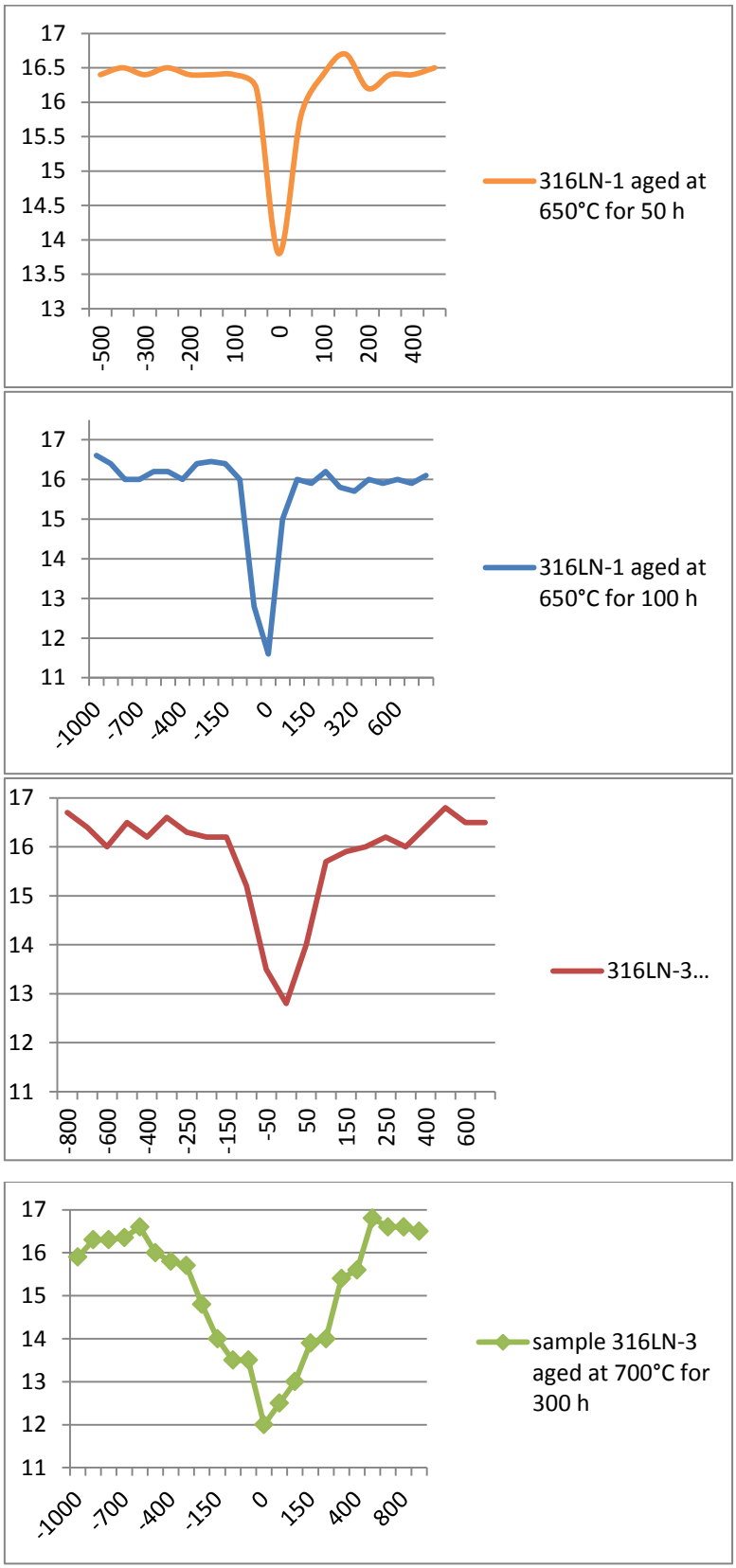

Figure 2-18: Chromium composition profiles normal to grain boundaries in the vicinity of M23C6 carbides for (a) sample 316LN-1 aged at 650°C for 50 h, (b) sample 316LN-1 aged at 650°C for 100 h, (c sample 316LN-3 aged at 700°C for 100 h, and (d) sample 316LN-3 aged at 700°C for 300 h. Solid line at left of each figure indicates bulk composition. [36]

Mechanism	Description	Fractrographic Features
EAC Mechanisms		
Hydrogen Embrittlement	A form of environmentally-assisted cracking which acts to embrittle a material. The introduction of atomic hydrogen into a metal can significantly reduce the ductility and toughness of a material.	• Voids ahead of crack • Slip at crack tips
Stress Corrosion Cracking	The slow, environmentally induced crack propagation of a metal under the action of a tensile stress.	
SCC Mechanisms		
Film rupture mechanism	The passive film ahead of a crack tip is ruptured by an initially applied stress. The exposed metal is subject to anodic dissolution, and the crack propagates.	• Crack arrest mark on surface • Intergranular SCC
Active path Corrosion/ Sensitisation	Compositional differences in the microstructures cause accelerated corrosion along a path which is more susceptible than the bulk material.	• Intergranular SCC
Corrosion Tunnel Model	Corrosion tunnels are formed by active corrosion. Dissolution of metal in the tunnels leads to fracture of the dissolved regions by ductile overload.	• Microvoid coalescence on peaks • Transgranular morphology of cracks • Grooved fracture surface
Film Induced Cleavage	If a brittle layer forms on a crack during corrosion, the brittle layer can inject a microcrack into the substrate before being arrested.	• Crack arrest marks • Discontinuous crack propagation • Cleavage-like features • Brittle cracking in metal

Table 2-6: Overview of main SCC mechanisms in steels

2.3.4.4 Crack initiation [32]

Crack initiation for SCC can occur from the following on a metal surface:

- Mechanical features;
- Pit;
- Crevice;
- Local galvanic cells; and
- Initiation at stress-induced area

Mechanical features such as scratches and dents are often initiation sites for cracking. The localised area will act as a stress raiser – promoting initiation of SCC by causing damage to the passive protective film or enhancing dissolution.

The local chemistry conditions which prevail in a pit may accelerate SCC. The pitting potential of a metal is often correlated to the SCC potential of the material. [34]

Local galvanic cells may be formed due to differences in material composition. The local corrosive effects will cause a particular phase of material to be dissolved preferentially. This will compound the localised stress accelerating crack initiation in the metal.

Crevice corrosion refers to preferential attack of a material due to stagnant solutions at a crevice. Differences in local chemistry at the crevice areas and the bulk environment cause an electrochemical reaction to take place at the respective areas.

A slip line intersecting a metal surface provides local anodes at the surface and disrupts the local film on the metal surface – so exposing the bare metal to anodic dissolution.

The local chemistry at the crack tip – as shown in Figure 2-19 – has an effect on the crack growth propagation. The conditions of the local crack chemistry can accelerate anodic SCC and hydrogen embrittlement.

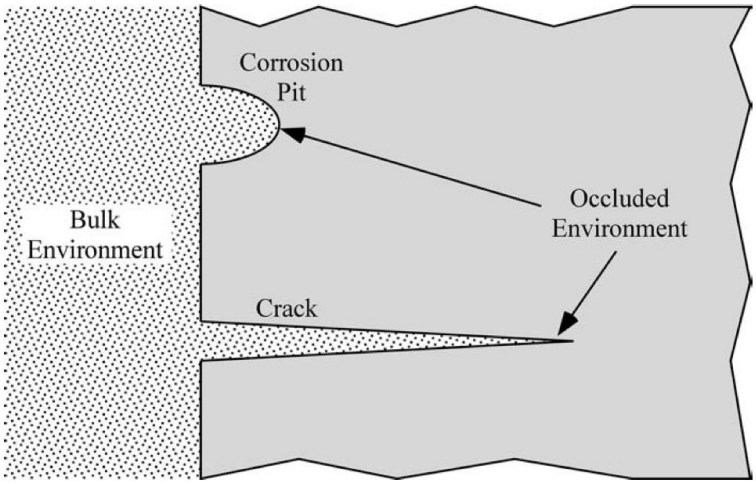

Figure 2-19: The local environmental conditions which prevail at the crack tip and corrosion pit differ from the bulk environment [32]

2.3.4.4. *SCC cracking morphology*

SCC cracking morphology is transgranular or intergranular as seen in Figure 2-20. The cracking morphology may exhibit a single planar crack or a branched network. The SCC cracking morphology depends on the SCC mechanism, the material, and the environment. [32]

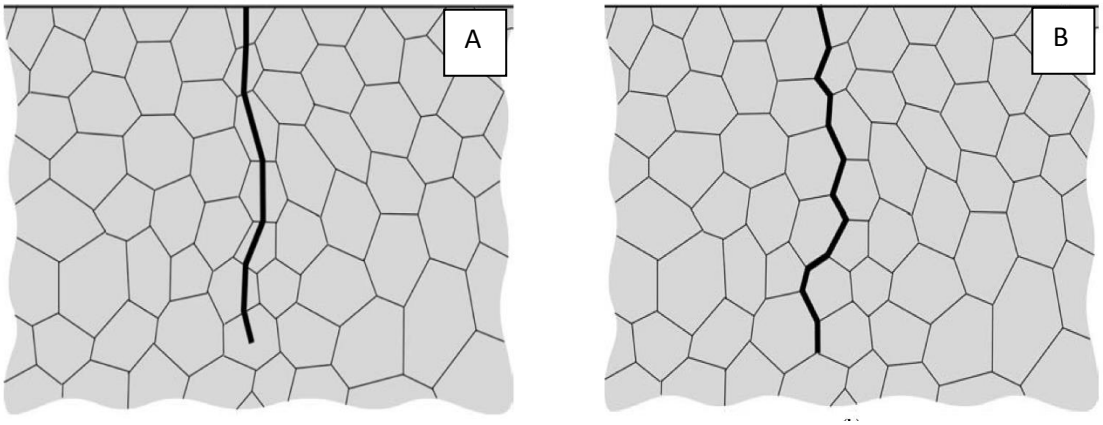

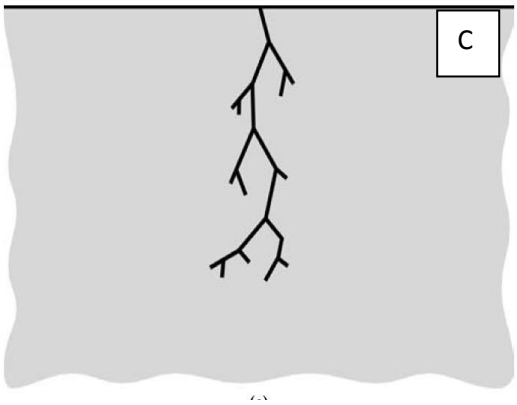

Figure 2-20: SCC morphology: a) transgranular SCC; b) single planar intergranular SCC; c) cracking branching which may be intergranular or transgranular [32]

2.3.4.5. *Effect of tempering temperature on SCC behaviour*

SCC of 12-13% LP turbine blades have been investigated by numerous researchers. [3] [4] [6] [34] Schleithoff et al. investigated the SCC of 13% Cr steels commonly used for manufacture of LP pressure steam turbine blades – namely X20C13, X22CrNoV121, X10CrNiMOV. These steels were tempered at 250°C, 420°C, 480°C, 600°C and 700°C. The tempered cylindrical test specimens were immersed in various test solutions. [46]

Schleithoff et al. showed that samples of X20C13 tempered above 600°C exhibited a SCC time to failure of greater than 4000 hours, while samples tempered between 420-480°C for both X20Cr13 and X22CrMoV121 were extremely susceptible to SCC with a time to failure of less than 10 hours seen in Figure 2-21. Schleithoff et al. also showed that SCC is also evident at varying applied stresses for the 250°C and 450°C temper samples – as seen in Figure 2-22.

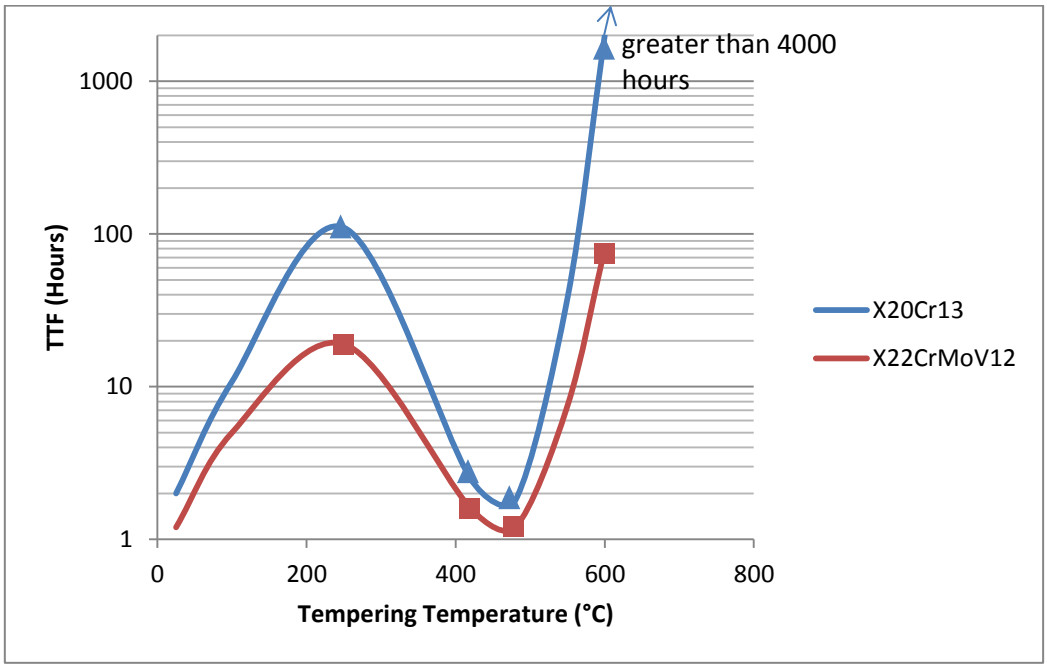

Figure 2-21: a) SCC time to failure of 13% Cr steels tested in 3% boiling NaCl; with an applied stress of 40% $R_{p0.2}$ [46]

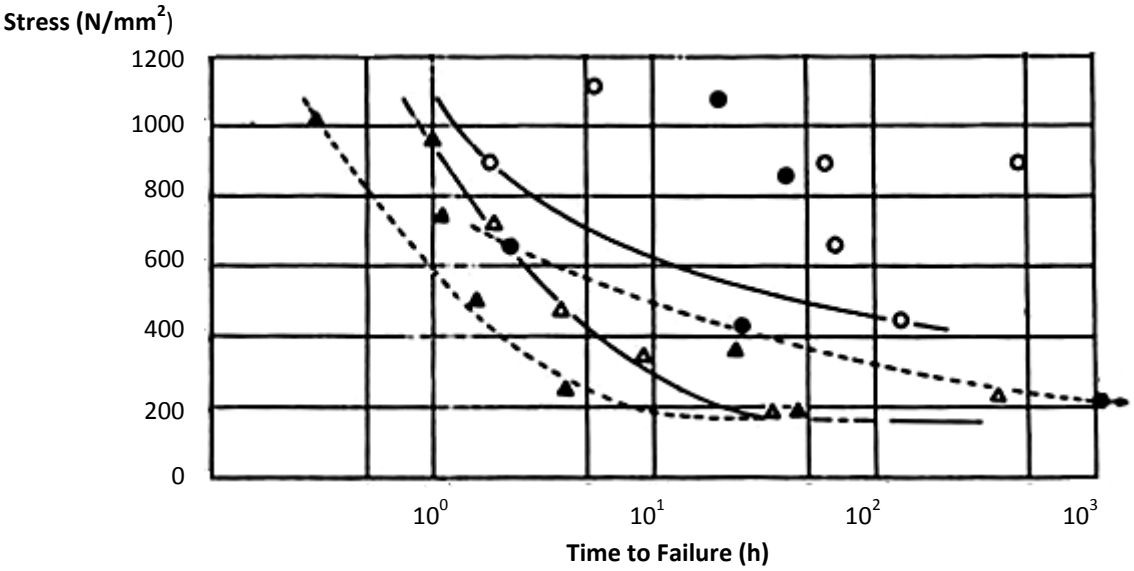

Figure 2-22: Evidence of SCC at low applied stresses [46]

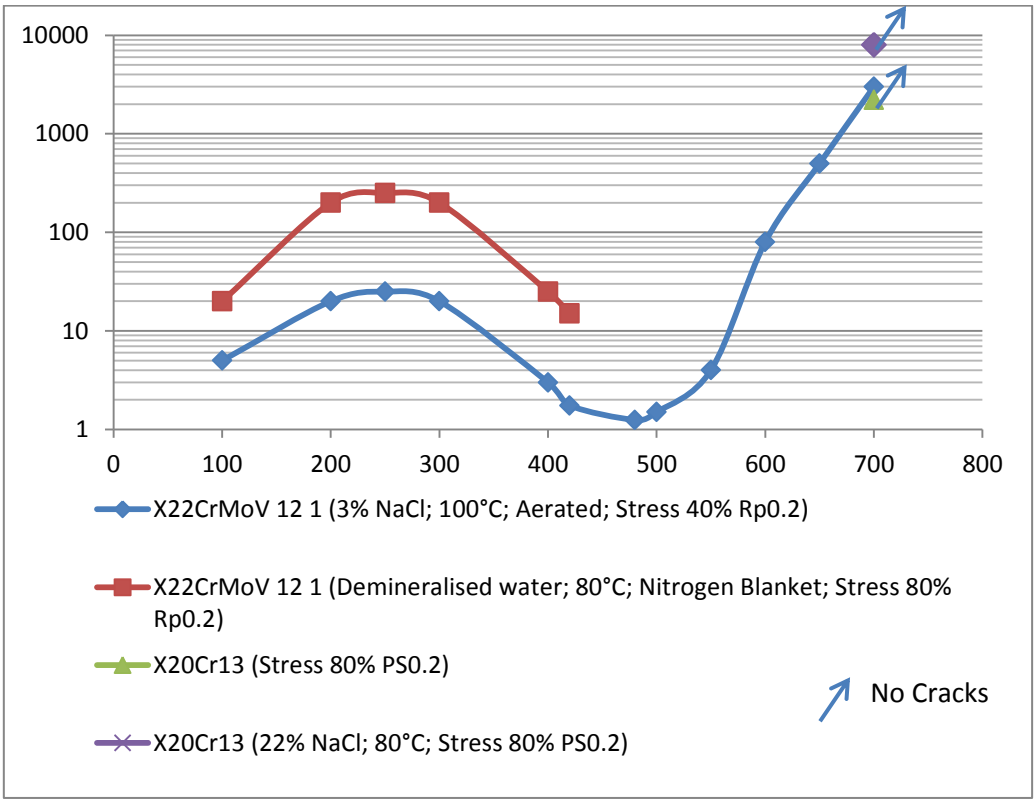

Figure 2-23: Effect of tempering temperature on SCC time to failure for 13% Cr steels [47]

Turnball et al. carried out SCC tests on FV566 samples tempered at 650°C. They found that for a SCC test environment of aerated 300 ppb Cl^- and 300 ppb SO_4^{2-}, the minimum K_{1SCC} was 42 to 52.9 MPa√m. The researchers noted crack growth rates in these environments and material temper conditions were at a minimum.

The effect of stress intensity factor on crack growth rate of FV566 in simulated steam turbine environments, is shown below in Figure 2-24. From Figure 2-25 and Figure 2-26 it can be seen the dependence of the crack growth rate on the chloride concentration and applied stress intensity factor. The crack growth rate increased with an increased stress intensity factor. From Figure 2-24 and Figure 2-25 it can been seen the environment has a significant impact on the crack growth rates. In Figure 2-26 deaerating the environment caused the crack growth rate to drop to less than 50µm/year. This crack growth rate is considered to represent K_{1SCC} crack growth and to have been arrested.

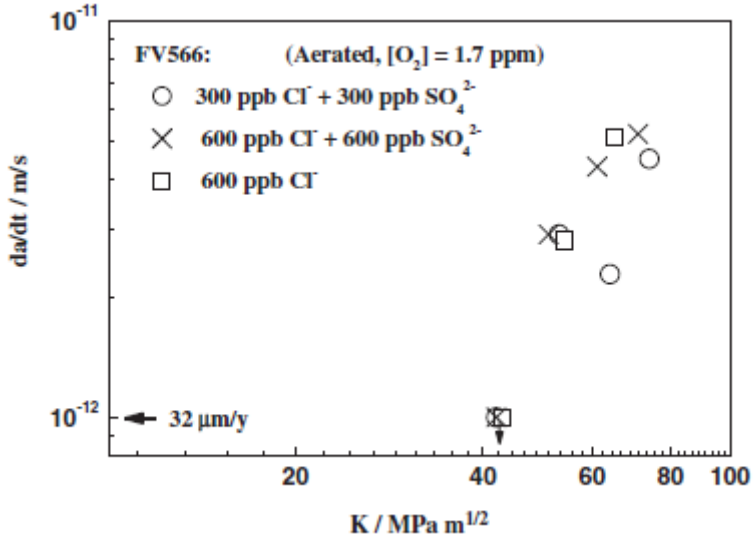

Figure 2-24: Effect of stress intensity factor on crack growth rate for FV566 steel in simulated steam turbine condensate solutions at 90°C [8]

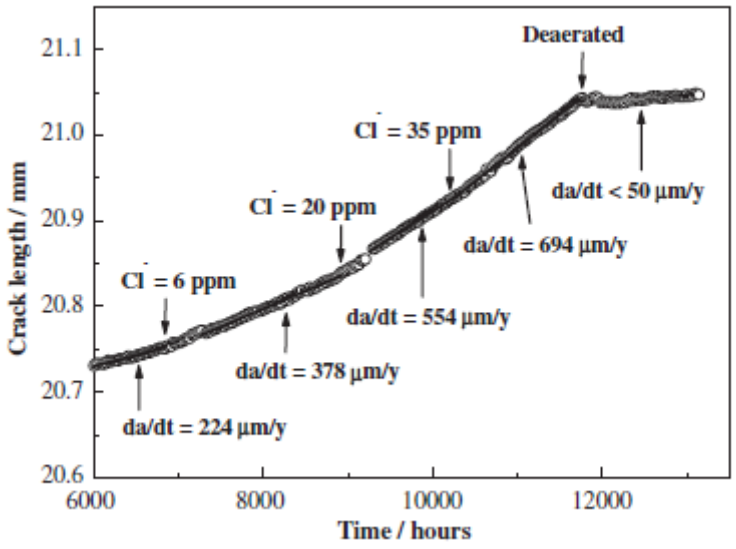

Figure 2-25: Impact of chloride concentration on crack growth rates for FV566 steel, with initial K value of 65 MPa√m (final value 67 MPa√m) and initial Cl^- concentration of 600 ppb [8]

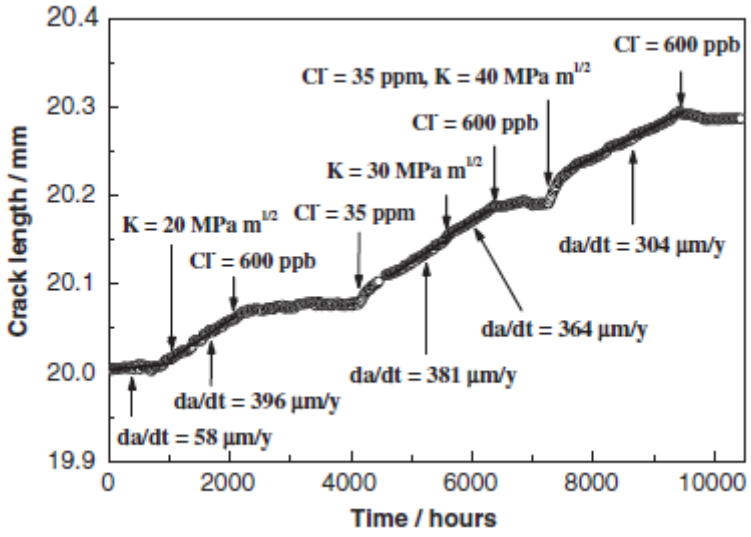

Figure 2-26: Effect of environment excursions on crack extension for FV566 steel in aerated solution at 90°C; the initial value of K was 16 MPa√m, and initial concentration of Cl^- was 35 ppm [8].

2.4. Fracture mechanics and SCC

Fracture mechanics is a branch of solid mechanics dealing with crack propagation in materials. Fracture mechanics' theory assumes an existing flaw is present in the material. A quantitative relationship between crack length and the material's inherent resistance to crack growth at particular applied stress is established. [48]

Fracture mechanics is a macro-mechanical approach which is used to characterise the SCC behaviour of materials. [48] The relationship between crack-growth data and applied stress is determined for SCC.

The fracture mechanics' approach used for SCC analysis assumes that the stress corrosion cracks are brittle – i.e. crack propagation occurs at stresses below the yield strength of the material and the cracks propagate in an elastic body, although local plasticity may occur at the crack tip. [48] This branch of study is termed Linear Elastic Fracture Mechanics (LEFM), and is commonly used in studying SCC and determining stress intensity at the crack tip.

2.4.1. Linear Elastic Fracture Mechanics (LEFM)

The LEFM model suggests three types of crack fracture modes: modes I, II and III. These can be seen in Figure 2-27 below. Mode 1 is a tensile or opening mode which is used to characterise SCC using LEFM. Mode II is in-plane shear mode, and Mode III is an out-of-plane shear crack opening mode. [48]

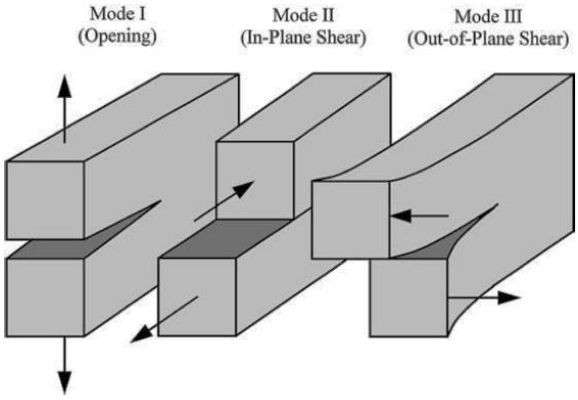

Figure 2-27: The modes of loading that can be applied to a crack tip [32]

The stress field ahead of a crack tip for mode I, can be characterised from the following equations: [49]

$$\sigma_x = \frac{K1}{\sqrt{2\pi r}} \cos\frac{\theta}{2}\left(1 - \sin\frac{\theta}{2}\sin\frac{3\theta}{2}\right) + \ldots\ldots \quad \text{Equation 2-1}$$

$$\sigma_y = \frac{K1}{\sqrt{2\pi r}} \cos\frac{\theta}{2}\left(1 + \sin\frac{\theta}{2}\sin\frac{3\theta}{2}\right) + \ldots\ldots \quad \text{Equation 2-2}$$

$$\tau_{xy} = \frac{K1}{\sqrt{2\pi r}} \cos\frac{\theta}{2}\cos\frac{3\theta}{2}\sin\frac{\theta}{2} \ldots\ldots\ldots \quad \text{Equation 2-3}$$

Where σ = stress

T = plain strain

K_1 = stress intensity factor

r and θ = geometrical factor of the crack tip

At points close to the crack tip, for $r \leq 0.1a$, the second and higher terms of equations are negligible.

2.4.2. Stress intensity factor and crack growth relationship

Crack growth for stress corrosion cracking occurs in the highly stressed region at the crack tip. The crack tip stress and displacement fields for an isotropic elastic body, can be characterised in terms of K, the crack tip stress intensity. [50] The crack tip stress intensity factor determines the intensity or magnitude of the local stresses at the crack tip. [50] K_1 represents the stress intensity factor for mode 1. Stress intensity factor K_{1scc} is the minimum threshold stress intensity for which SCC is possible. [4]

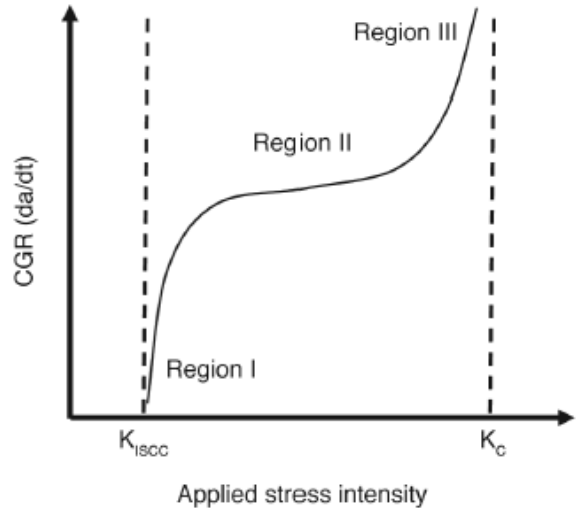

Figure 2-28: Schematic representation of the relationship between instantaneous stress intensity and crack growth rate [4]

The presence of an aggressive environment in SCC influences the relationship between crack growth rate and stress intensity.

Stress corrosion data are often plotted as a function of the applied stress intensity versus crack growth rate. The theoretical relationship between the instantaneous crack tip stress intensity and crack growth behaviour, is depicted in Figure 2-28 above. Three distinct regions can be seen. In region I the crack growth rate increases with increasing applied stress intensity; this region is near but above the critical K_1 value. In region II crack growth rate is semi constant and independent of the applied stress intensity; the crack growth rates are limited by corrosion kinetics in this region. In Region III as the applied stress intensity increases the crack growth rate increases sharply. The SCC mechanism is dominated by the mechanical component instead of corrosion, and fracture will occur in region III.

The stress intensity of a material depends on the applied stress σ, the initial crack length a, and the specimen geometry. Some plastic deformation will occur in a region near the crack tip. Given that the zone of plastic deformation is small compared to the crack size and specimen dimensions, the stress condition in the large specimen section will not be influenced. The elasticity solutions will represent an approximation of the stress near the crack tip. The small zone of plastically deformed material at the crack tip is contained within the surrounding elastic material, and therefore the behaviour in this region would be determined by the surrounding elastic material and be characterised by the crack-tip stress-intensity factor K. [50]

Close-form solutions for K_1 have been derived for a wide range of specimen geometries. [32] For mode 1, the stress intensity factor of a crack in a plate of infinite length, subject to tensile stress, is given by:

$$\boldsymbol{K_1 = \sigma\sqrt{\pi a}} \qquad \text{Equation 2-4}$$

The stress intensity at the crack tip is proportional to the applied stress and the square root of the crack length. This equation is applicable to a plate of infinite length. To determine the stress intensity factor for different geometries, the compliance of the equation must be known. Compliance is defined as the inverse of the deflection of the component for each crack length. [32] Compliance is specific for each material and specimen geometry combination. Compliance relationships are available for conventional geometry fatigue and SCC specimens.

2.4.3. Kinetics of crack growth

The study of stress corrosion crack growth using fracture mechanics-based specimens is largely categorised into three main groups:

- Constant load or increasing K_1 specimens;
- Constant displacement or decreasing K_1 specimens; and
- Constant K_1 specimens.

For this study, the constant displacement or decreasing K_1 specimen was utilised.

Crack growth for stress corrosion cracking is often described by Figure 2-28 above. While this schematic represents crack growth kinetics, it does not account for a number of non-steady-state crack growth phenomenon. Wei and Novak [51] concluded that crack growth occurs in six different stages:

- Incubation period;
- Initial transient crack growth;
- Crack acceleration;
- Crack growth on rising load;
- Steady state crack growth; and
- Onset to failure or crack instability.

Lei et al., Barsom, Landes and Wei [50] all studied the crack extension on loading and initial transient growth. The initial crack growth from loading – as shown in Figure 2-29 below – is followed by a

second incubation period in which the crack length remains nearly constant. This is followed by accelerating crack growth. The crack growth rate is also dependant on the applied stress intensity K.

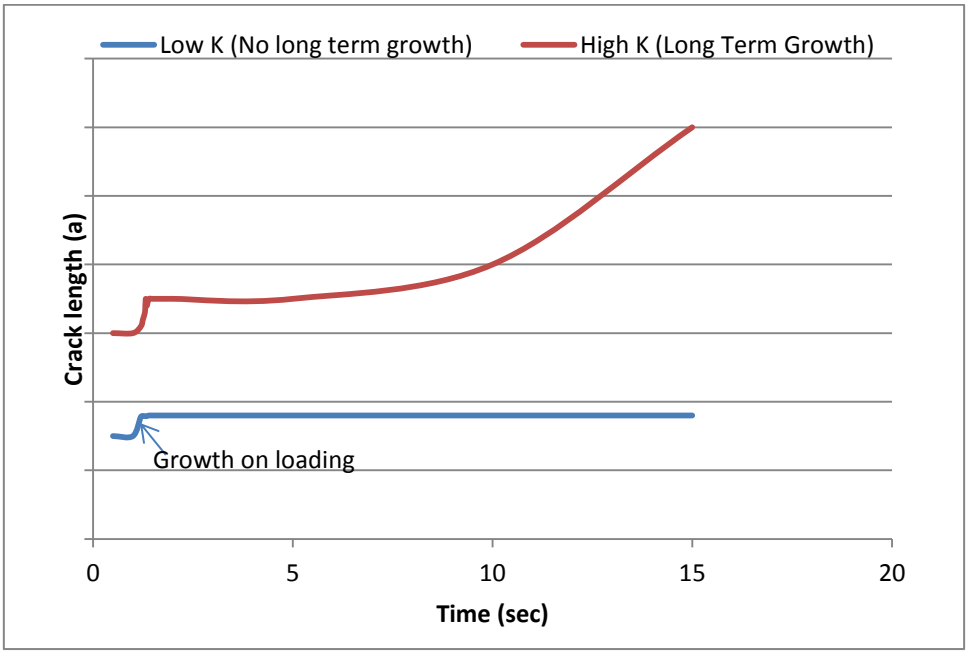

Figure 2-29: Schematic illustration of sustained load crack growth behaviour [50]

This period of accelerating non-steady crack growth rate, is followed by steady-state crack growth.

Hudak and Wei [51] studied the non-steady crack growth behaviour for AISI 4340 steel in distilled water. Wei and Hudak [51] carried out stress corrosion tests under constant load and showed that non-steady crack growth was present for the steel. Transient periods of crack growth were noted before steady-state crack growth.

Zanpeng Lu et al. [52] carried out various tests on cold-worked 316L SS specimens in high temperature pure water at different loading modes. Zanpeng et al. postulated that transient crack growth can be related to the initial bulk conditions of the test, the initial crack tip condition, and previous specimen history or testing history. [52] Zanpeng et al. showed that changing the test parameters, in terms of the test temperature, affected the crack growth rate shown in Figure 2-30.

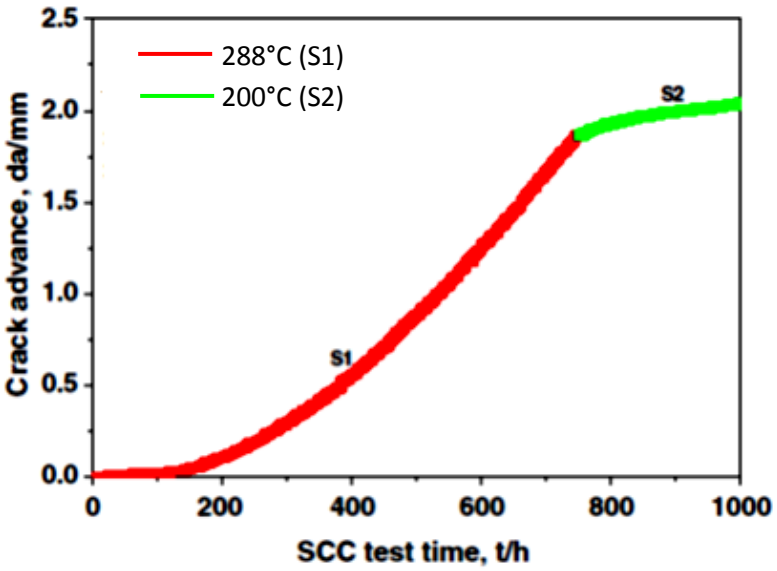

Figure 2-30: Crack growth kinetics for each test condition for CW316L stainless steel in pure water, with 2 ppm DO under trapezoidal wave loading at different test temperatures. [53] Test conditions: high purity water; DO=2ppm (inlet),316L CW YS=760MPa, K and K =30MPa.m; trap loading: 12h CL+60s/R=0.7 unloading/reloading [52]

2.4.4. Crack closure

In 1970 Elber [32] discovered an irregularity in the elastic compliance of several fatigue-loaded specimens. At low loads the compliance for fracture mechanics' specimens was close to that of an uncracked specimen, and did not agree with standard formulae. Elber postulated that this was due to the "crack closure" or contact between the two crack surfaces.

Elber postulated that crack closure reduced the effective stress intensity and hence the crack growth rate. He deduced that the stress intensity below the crack opening stress intensity (K_{op}) does not play a role in fatigue crack growth – as there is no difference in the crack-tip strain. He defined the effective stress intensity as:

$$\Delta K_{eff} = K_{max} - K_{op} \qquad \text{Equation 2-5}$$

Where K_{eff} = effective stress intensity factor

K_{max} = Maximum applied stress intensity factor during fatigue loading

K_{op} = Opening stress intensity factor

This is displayed in Figure 2-31.

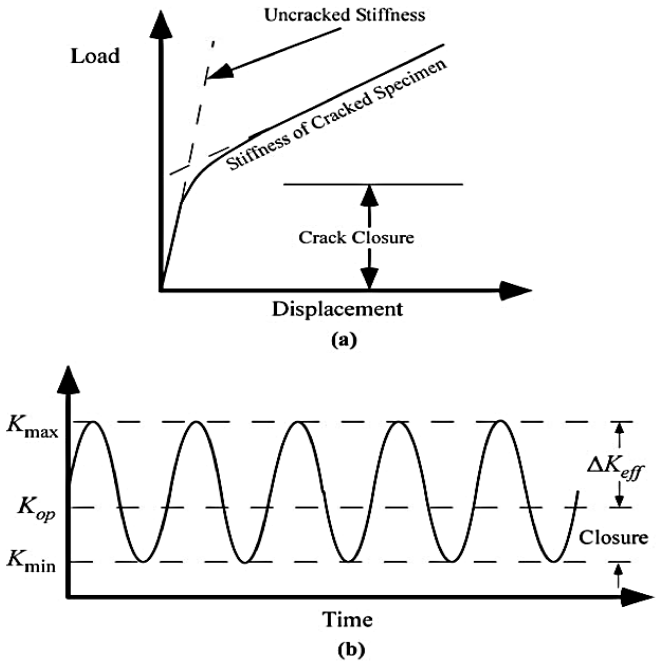

Figure 2-31: Crack closure during fatigue crack growth: a) the crack faces contact, which results in a reduced effective stress intensity factor; b) definition of the effective stress intensity factor [32]

Suresh et al. acknowledged five different mechanisms for crack closure – seen in Figure 2-32. [32] These mechanisms are: plasticity-induced closure; roughness-induced closure; corrosion product-induced closure; closure induced by a viscous fluid; and transformation-induced closure.

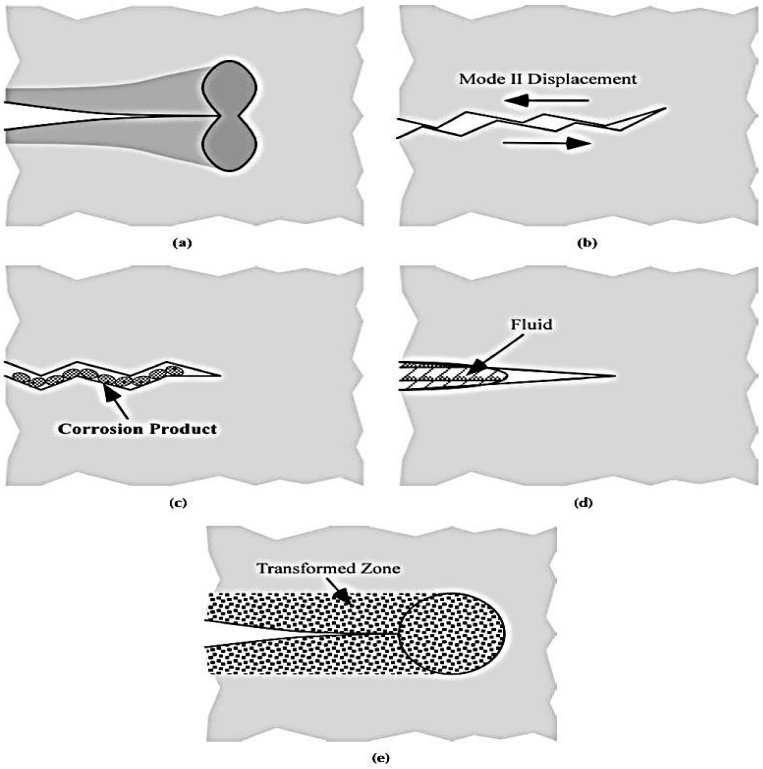

Figure 2-32: fatigue closure mechanisms for various specimens by: a) plasticity-induced closure; b) roughness-induced closure; c) corrosion product-induced closure; d) closure induced by a viscous fluid; and e) transformation-induced closure [32]

2.4.5. Crack wedging

Mechanisms C, D and E in Figure 2-32 entail cracking wedging of the specimens. These mechanisms are interchangeably referred to as wedging or closure. In Figure 2-33 below, an ideal wedge open loaded specimen is depicted. It is assumed that the crack conforms perfectly to the wedge and all faces of the wedge are in contact with the crack when no load is applied. A stress intensity of K_{wedge} is present when no external stress is applied. When the load is applied, the applied stress intensity factor does not change until the applied K is greater than the K_{wedge}. The effective applied stress intensity is defined as:

$$\Delta K_{eff} = K_{max} - K_{wedge}$$

A more realistic depiction of crack wedge opening is depicted in Figure 2-34, where the crack is filled with particles of various sizes. As the applied stress is reduced, the slope of the CMOD versus load curve decreases. A constant CMOD is eventually achieved as the applied stress decreases to zero – assuming the particles are rigid. The effective stress intensity is hence more complex and the final slope of the CMOD versus load curve will reflect the elasticity of the wedge product.

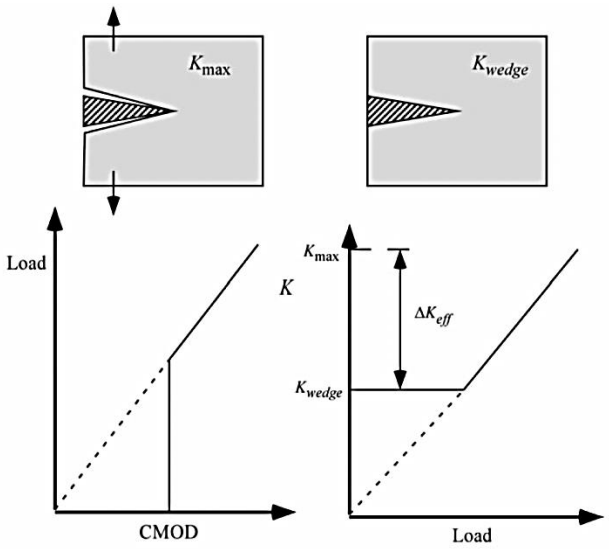

Figure 2-33: Load displacement behaviour and ΔK_{eff} for an ideal wedge loaded specimen [31]

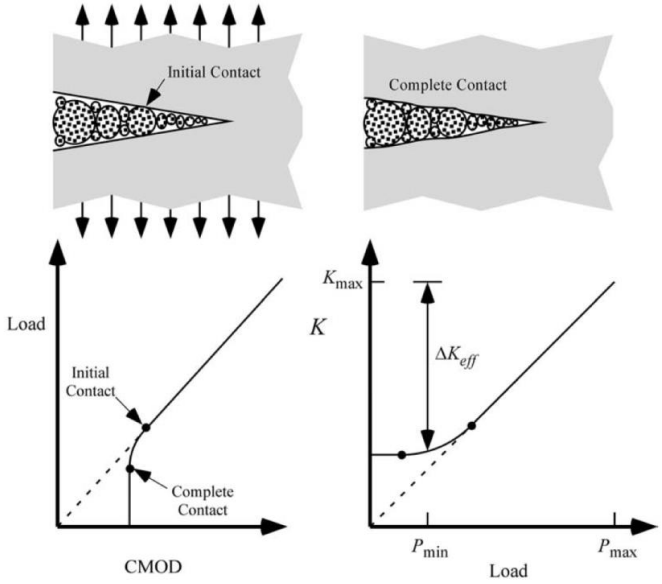

Figure 2-34: Load displacement and ΔK_{eff} for a crack enclosed with particles of various sizes [32]

2.4.6. Crack-tip overloading

Overloading of a fatigue precrack in air can result in crack-tip blunting. The plastically deformed crack tip is compressed by the surrounding elastically strained material, and this produces residual stresses. This has an adverse effect upon the incubation times for stress corrosion. [53] Hanish and Burck [54] studied the effect of crack-tip overloading in an aluminium alloy. The study showed that the incubation period increased with increasing percentage overloads, and that this effect was more pronounced at high residual stress intensity levels. Carter [55] showed that overloading of precracks in

AISI 4340 steel, prior to environmental testing, increased the apparent threshold intensity factor for cracking. This was attributed to the development of residual compressive stresses.

3. Experimental Methodology

This chapter aims to describe the experimental and characterisation techniques and methodologies used in the study. The experimental methodology can be summarised as follows:

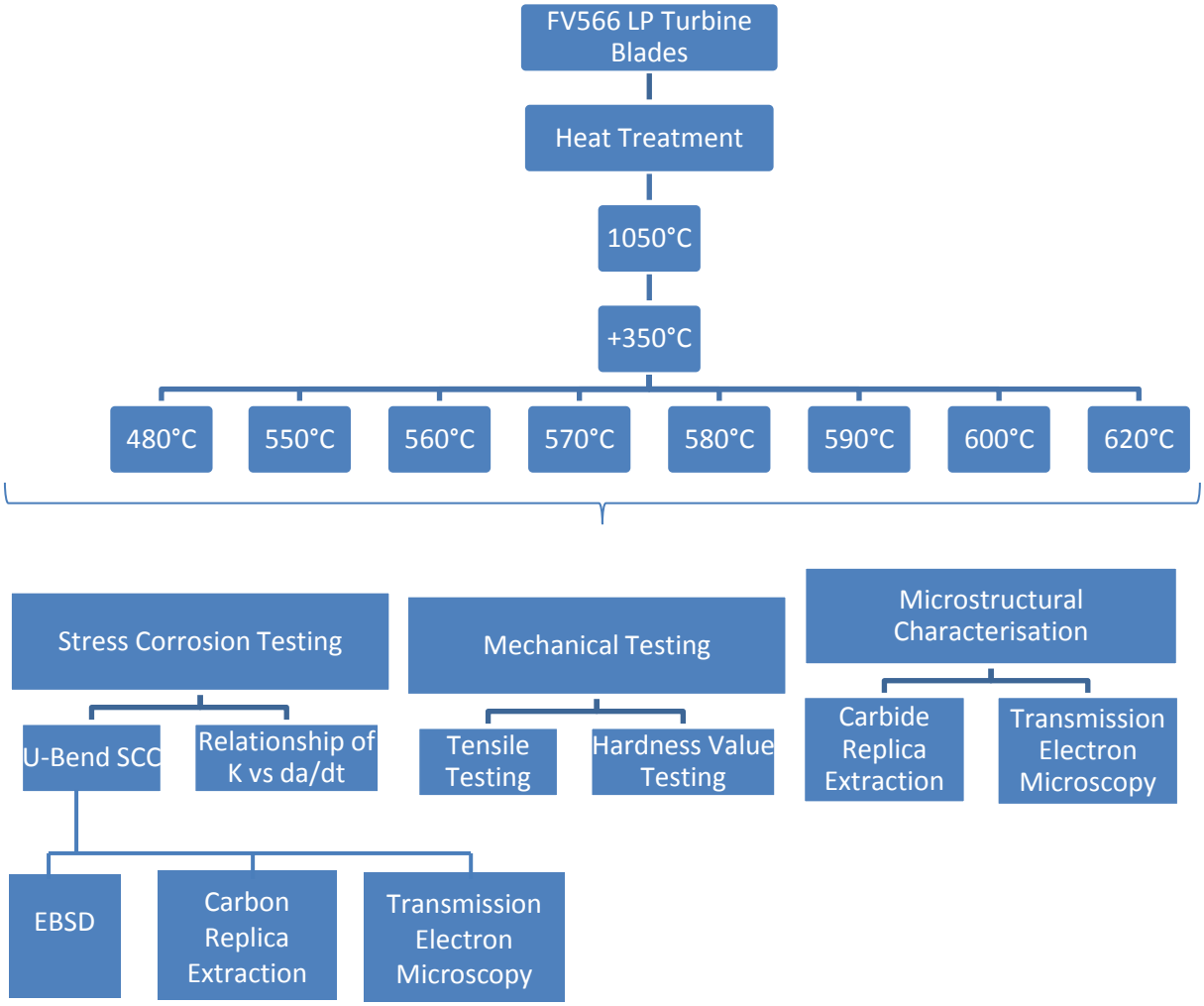

3.1. Heat treatment

The heat treatment of the steel consists of steps of austenitising, quenching and double tempering. Austenitising is carried out at 1050°C for one hour, which is sufficiently long to generate a fully austenitic matrix and dissolve carbon completely. Subsequently, the material is quenched in air. The high amount of alloying elements ensures the complete martensitic transformation with carbon atoms trapped in the matrix and distributed homogeneously. This is followed by a double temper heat treatment accompanied with intermittent air quenching. The first temper treatment is carried out at 350°C for one hour. This is followed by tempering of the material in the range of 480-620°C which enhances the ductility and toughness. Tempering replaces the solid solution strengthening of the dissolved carbon with precipitation strengthening by carbides.

The tempering temperatures selected are 480°C, 550°C, 560°C, 570°C, 580°C, 590°C, 600°C and 620°C. The tempering range was chosen to investigate the impact a marginal change in the tempering temperature will have on the microstructure, mechanical properties and SCC properties.

The specimens are coated before heat treatment with Foseco Isomol ceramic coating to prevent decarburisation and oxygenation of the material at higher temperatures. Samples were heat treated in a box furnace with the use of two external thermocouples to measure the sample temperature to account for any error in the box furnace temperature reading.

Figure 3-1: Coating of samples with Foseco Isomol and box furnace with additional thermocouples

3.2. Specimen orientation

The material examined in this study is from forged turbine blades. The turbine blades are of a fir tree design. All specimens for the experimentation are obtained from the root of the blade. Specimens were polished, etched with Vilella's Reagent and examined under the light microscope for grain structure directionality. Microstructural investigation did not indicate directionality in the grain structure or aluminium oxide inclusion.

Data received from industry indicated stress corrosion cracking propagates in a direction normal to the fir tree connection, shown in Figure 3-2. Specimens were therefore manufactured with the applied principal tensile stress normal to the crack propagation i.e. cracks 1, 2, 3, 4 depicted in Figure 3-2.

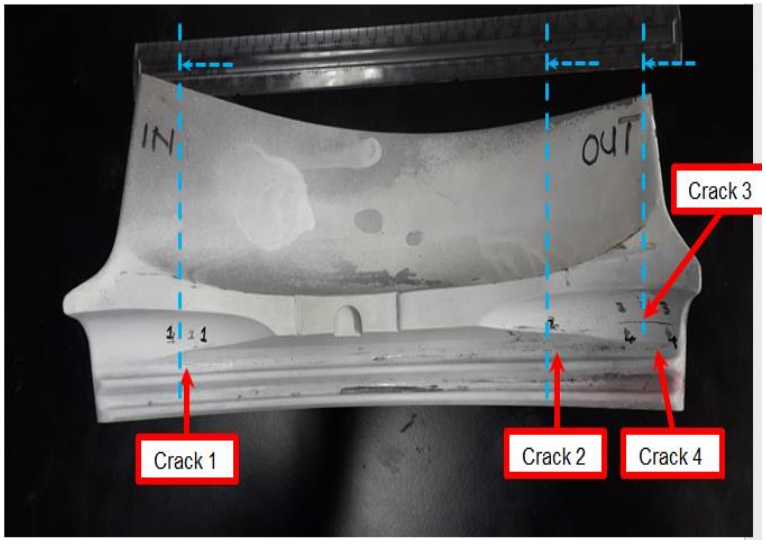

Figure 3-2: Data received from industry for crack propagation direction [11]

3.3. Mechanical properties testing

Mechanical properties testing included hardness testing and tensile testing. Mechanical properties were evaluated at heat treatment levels as per section 3.1. These properties were used to evaluate the appropriate starting stress intensity (K_{10}) applied during threshold stress intensity determination tests. The results of the mechanical testing were additionally used to evaluate the comprehensive effect of tempering on the material properties.

3.3.1. Hardness value testing

Hardness testing was carried out on a Vickers macro-hardness testing machine with a testing load of 30kg. Specimens were taken from the root of the LP turbine blade and polished to a 0.25µm surface finish. Four specimens were assessed for each heat treatment level and the data compared to a previous study by van Rooyen. [3]

3.3.2. Tensile testing

Tests were carried out in accordance to ASTM E8/EM8-11. [56] Tensile tests were conducted to failure on two specimens of each heat treatment level using a Zwick tensile testing machine fitted with a 200kN load cell. Tests were carried out in accordance to ASTM E8/EM8-11. A preload of 200N and a strain rate of 10^{-1}s were applied. A specimen with a gauge length of 26mm with diameter of 6mm and dimensions as shown in Figure 3-4 were utilised.

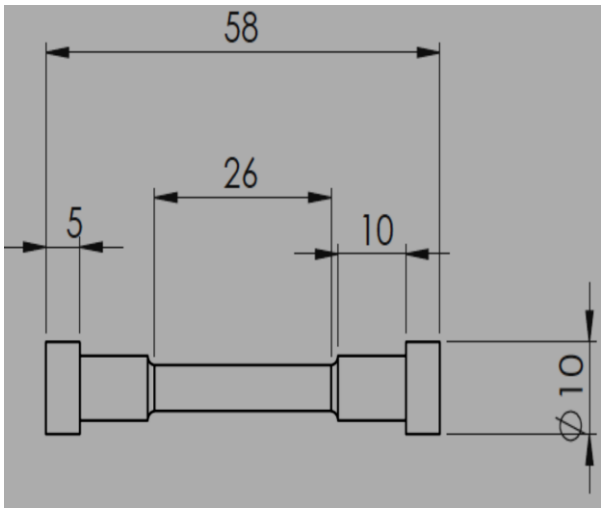

Figure 3-3: Dimensions of tensile testing specimen

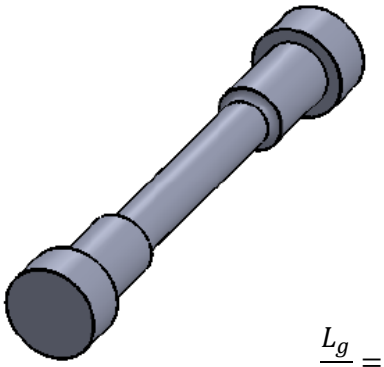

$$\frac{L_g}{D_g} = 4.33$$

L_g = Gauge Length

D_g = Gauge Diameter

Figure 3-4: Pictorial view of specimen

3.4. Microstructural characterisation

Microstructural characterisation was carried out using various techniques, including: light microscopy, scanning electron microscopy, transmission electron microscopy, electron backscattered diffraction, X-ray diffraction, and carbide replica extraction. The techniques were used to determine the effect of the tempering temperature on the microstructure of the material.

3.4.1. Sample Preparation

Sample preparation was necessary before microstructural characterisation. Samples were grinded and polished as per Table 3-1. After each step of polishing samples were cleaned with soap and rinsed with distilled water. The final polishing step with a colloidal silica polish sufficiently etched the surface for the light microscopy and EBSD.

Step	Force (N)	Rotation (rpm)	Time (min)
Grind – 800grit	As required	200	3-5
Grind – 1200grit	As required	200	3-5
Polish - 6µm DiaDuo diamond suspension and lubricant	20	150	10
Polish - 3µm DiaDuo diamond suspension and lubricant	20	150	12
Polish - 1µm DiaDuo diamond suspension and lubricant	20	150	5
Polish - 0.25µm DiaDuo diamond suspension and lubricant	10	150	8
Polish - OP colloidal silica suspension	10	150	2

Table 3-1: Sample preparation for microstructural characterisation

3.4.2. Light microscopy

Heat treated specimens were polished, etched in Vilella's Reagent (5ml hydrochloric acid, 1g picric acid in 100ml ethanol) and examined under bright field mode using a Leica Reichart MeF2. Etching revealed martensite lathes, grain boundaries and inclusions. Forging directionality was investigated. The inclusion content was analysed with EDS. The results are presented in section 4.3.1

3.4.3. Energy dispersive X-ray spectroscopy

Energy Dispersive X-ray Spectroscopy (EDS) is a characterisation technique which allows for elemental identification and its relative proportions in a material. EDS operates on the principle that each element has a unique atomic structure. A high energy beam of electrons are focused on the material in question. [57] The energy of the X-ray emitted from the material is measured by an energy dispersive spectrometer. The energy of the emitted X-ray is unique to the atomic structure of each element. The elemental composition of the material can therefore be determined. [57]

Inclusions content for FV566 steel were analysed using a EDS on Nova NanoSem 230. An accelerating voltage of 10kV and a spot size of 5µm were used in the analysis. Results are presented in section 4.3.2.

3.4.4. Carbon extraction replica

Two main methods for replication techniques are available. These methods can be classified as surface replication or extraction replication. Surface replication provides an image of the surface topography whereas extraction replication lifts particles from the surface of the specimen. [58] Carbon extraction replica was used to extract carbide precipitates embedded in the matrix of the specimen surface. These particles were later analysed using the Transmission Electron Microscope (TEM).

Direct carbon replica extraction process was used. Heat treatment samples were grinded to a 1200 SiC grit surface finish. Samples were then etched in Vilella's Reagent which attacks the matrix of the material rendering the particles loose and in relief on the surface of the specimen. [59] Carbon is thereafter evaporated under a vacuum environment onto the surface of the specimen. Squares are scribed on the surface of the specimen to accelerate the attack of the material. [60] The specimens are thereafter etched again through the carbon coating in Villella's Reagent for 30-60 seconds. The scribed squares which contain the carbon coating and carbide precipitates float in the etchant. These are carefully removed with copper mesh screens and washed in distilled water. The precipitates are examined in the TEM. The magnetic ion matrix is removed hence the CER samples do not affect the electromagnetic lenses of the TEM.

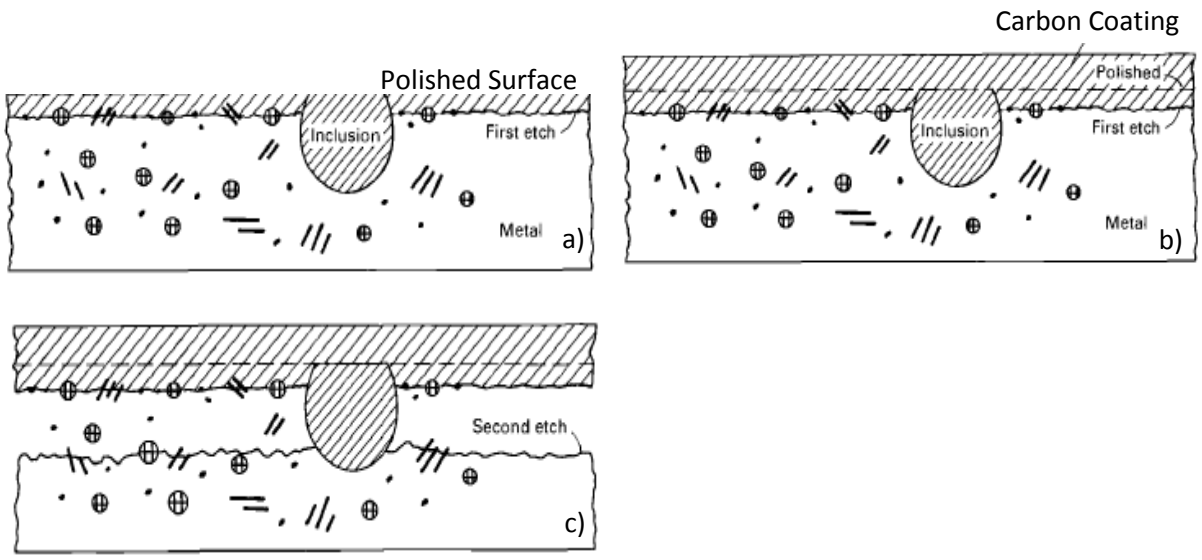

Figure 3-5: Carbon extraction replica: a) polished sample etched; b) etched sample coated with carbon; c) carbon-coated sample etched again to loosen precipitates from matrix [58]

3.4.5. Transmission Electron Microscopy (TEM) [61]

Transmission electron microscopy was used to analyse the effect of tempering on the location and formation of chromium rich particles.

TEM is characterisation technique which utilises a high voltage beam of electrons emitted by a cathode. The beam of electrons which is partially transmitted through the material interacts with the specimen forming and image. An imaging device such as a CCD camera is used to focus and magnify the image. The contrast of the TEM image is as a result of the absorption of electrons in the material.

TEM samples were extracted from the 550°C, 580°C and 600°C temper sample across prior austenite grain boundaries. Energy filtered TEM mapping was carried out to determine the location of the chromium rich precipitates in the specimen. These samples were chosen to compare a low, medium and high tempering temperature used in this study.

TEM utilises particularly thin specimens of approximately 100nm in thickness or less. Samples for TEM analysis of the different temper treatments were prepared using CER, focused ion beam and Argon milling.

Focused ion beam samples utilised Ga+ particles to mill material from a bulk sample using the SEM. These samples are removed and placed onto a TEM grid. TEM lamellae of 5X5X0,1µm^3 in size were prepared using a Helios NanoLan FIB SEM. A carbon layer is deposited on sample surface to protect the sample from the milling steps. Thereafter trenches are milled on either side of the carbon layer. The sample is thereafter removed from the bulk material by attaching the probe and cutting the

lamella free from the sample as described in Figure 3-6. The sample is then attached to the TEM grid using carbon deposition. The lamella is then polished down to a thickness of less than 100nm as per Table 3-2.

Samples prepared by TEM were of approximately 5X5µm^2 in size. This small sampling area inhibits the size of the precipitates which are analysed. This limitation is overcome with the use of CRE samples which are of the size of 2X2mm^2 as described in section 3.4.4.

The samples which were prepared by Argon milling did not produce samples of satisfactory quality and were not utilised in the study. Only samples obtained using the focused ion beam with Ga+ utilised for milling were used for TEM analysis.

Samples were analysed using a JOEL JEM 2100 (Lab6) and Joel Double Cs-corrected Atomic resolution Microscope (ARM) 200F.

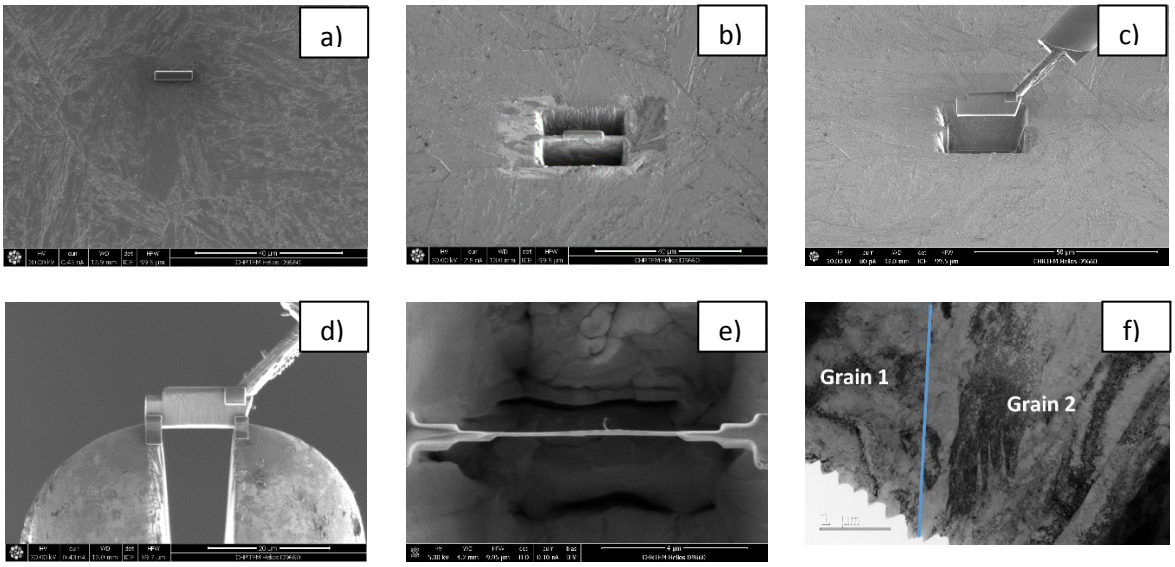

Figure 3-6: Secondary electron images of the stages in FIB-SEM sample preparation: a) carbon deposition; b) milling of trenches; c) removal of lamella; d) attachment of the sample to the TEM grid; e) polishing of the sample to 100nm; f) bright field TEM image of a grain boundary

Final thickness (nm)	Accelerating voltage (kV)	Ion beam current (nA)
2000	30	47, 9, 2.5
500	30	0.79
200	30	0.23
<100	5	0.041
<100	2	0.023
<100	0.5	0.011

Table 3-2: FIB SEM polishing parameters

3.5. Stress corrosion testing

Stress corrosion testing was divided into two categories. The first set of tests were carried out to determine the materials susceptibility at different heat treatments to stress corrosion cracking, the time taken for specimens to fail under stress corrosion cracking, and the mechanism of SCC. These tests were carried out with U-bend specimens.

The second set of tests was conducted to determine the threshold stress intensity as a function of crack growth rate for each heat treatment. SCC tests methods using fracture mechanics can largely be classified as: [62]

a) constant load (increasing stress intensity specimens);
b) constant displacement (decreasing stress intensity specimens); and
c) constant stress intensity specimens.

Constant load specimens are frequently associated with elaborate and large testing fixtures e.g. dead-weight-loaded cantilever beam specimens. To eliminate the high economic costs associated with this type of fixtures and for practical reasons the constant displacement type of testing is used. These were tests were accomplished with the use of wedge-open loaded (WOL) specimens. Both the experimental techniques are described in detail in the subsections below.

3.5.1. Stress corrosion testing environment

During normal operating conditions of a steam turbine the quality inlet water chemistry is maintained at a high standard with low impurities. The liquid film which forms on the turbine blades may have anionic impurities less than or about 300 ppb sulphate and 300 ppb chloride. [6] Excursions in the impurity level in the inlet water conditions may lead to magnified levels of impurity in the condensate film. [6] Studies showed there is 1% wetness on the LP blade surface the concentration

will be 100 times the impurity level in the steam and this will form the liquid layer on the metal surface [6]. This analysis is showed in Figure 3-7. It can only be approximate because it assumes that the condensed layer is dominated by the concentration in the steam phase with no evaporation.

Analysis of deposits on the surface of fractured blades by the Electric Power Research Institute (EPRI) revealed chloride contents of 0.2-12% and sodium oxides of up to 30% can be recognised as potential corrosive constituents. [63] A NaCl environment would thus be suitable for laboratory SCC testing. Stress corrosion testing was carried out in 3.5% NaCl solution. An aggressive environment was used to accelerate stress corrosion testing times, to achieve crack initiation and growth within the time frame of this project.

The test solution was refreshed weekly. Test temperature was maintained at 90±2°C. This corresponds to the regime of early condensation and establishment of a thin liquid film. [8] Test temperature and pH level were monitored daily. No measures were taken to change pH levels.

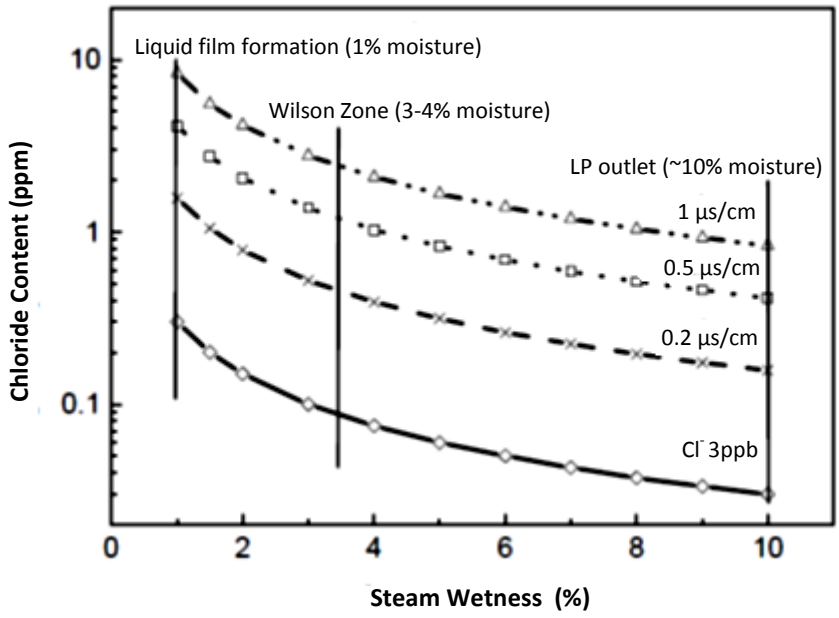

Figure 3-7: Chloride content in the water phase as a function of steam wetness at various cation conductivities of the inlet steam. A specific example for an inlet steam containing 3 ppb chloride is shown [6]

3.5.2. Susceptibility stress corrosion testing

U-bend stress corrosion testing is a simple, economical testing method which allows a large number of specimens to be tested simultaneously. U-bend stress corrosion testing was performed in accordance to ASTM G30-97 [64] and ASTM G123-00. [65] The time taken for cracks to develop and the sample to fail is monitored. The test provides an understanding of the materials resistance to stress

corrosion cracking in the specified environment. The specimens were continuously immersed in the environment described in section 3.5.1 above.

The U-bend specimen is a constant deformation type of specimen. The specimen contains both elastic and plastic strain.

The stresses present in a U-bend specimen are non-uniform for various reasons: [64]

a) The stress varies through the thickness of the specimen with a maximum tension on the outer surface and a maximum compression on the inner surface;
b) The stress varies from zero at the ends of the specimen to a maximum at the centre of the specimen; and
c) The stress may vary across the width of the specimen.

The stresses present in a U-bend sample are hence complex and depends on the method of fabrication and bend conditions.

The total strain (ε) on the outside of the bend can be evaluated from: [64]

$$\varepsilon = \frac{T}{2R} \quad if\ T \ll R$$ Equation 3-1

where T = thickness of the U-bend
R = bend radius.

3.5.2.1. Sample geometry, fabrication and preparation

U-bend stress corrosion test samples were manufactured in accordance to ASTM G30-97. [64] The U-bend specimen is a rectangular strip bent 180° around a predetermined radius and maintained in this constant strain during the stress corrosion test. [64] Un-notched U-bend stress corrosion samples were used.

Specimens were fabricated after final heat treatment and surface preparation. The specimens were ground to achieve a surface finish of 0.76µm or better as per ASTM standard G30-97. [64] The surface finish of each specimen is listed in Table 3-3. The sides of the specimen were polished to achieve the same surface finish as the faces.

A two stage stressing method was used to form the U-bends. This method involves forming of the U-bend shape in a tensile testing machine as depicted in Figure 3-8. The elastic stress is then allowed to completely relax and test stress is achieved by means of a bolt and nut depicted in Figure 3-9. Samples were produced using a 200kN Zwick tensile testing machine fitted with a 3 point bending jig. A mandrel diameter of 9.8mm was used to form the shape of the U-bend. The bolt and nut were

coated with a neoprene polymer based paint to electrically isolate the specimen and prevent crevice corrosion. Additionally insulating washers made from plastic were used.

Specimen width, length and thickness were determined by the form of the material available, stressing method used, strength and ductility of the material. [64] Specimens were manufactured from the root of the turbine blade. High strength steels with a yield strength in excess of 1400 MPa prove difficult to bend if the thickness of the specimen is greater than 3mm. [64] Experimental fabrication of U-bend samples with FV566 material confirmed this. A specimen thickness of 1mm was hence used to allow for ease of fabrication of the specimens. Specimens were manufactured to dimension shown in Figure 3-10.

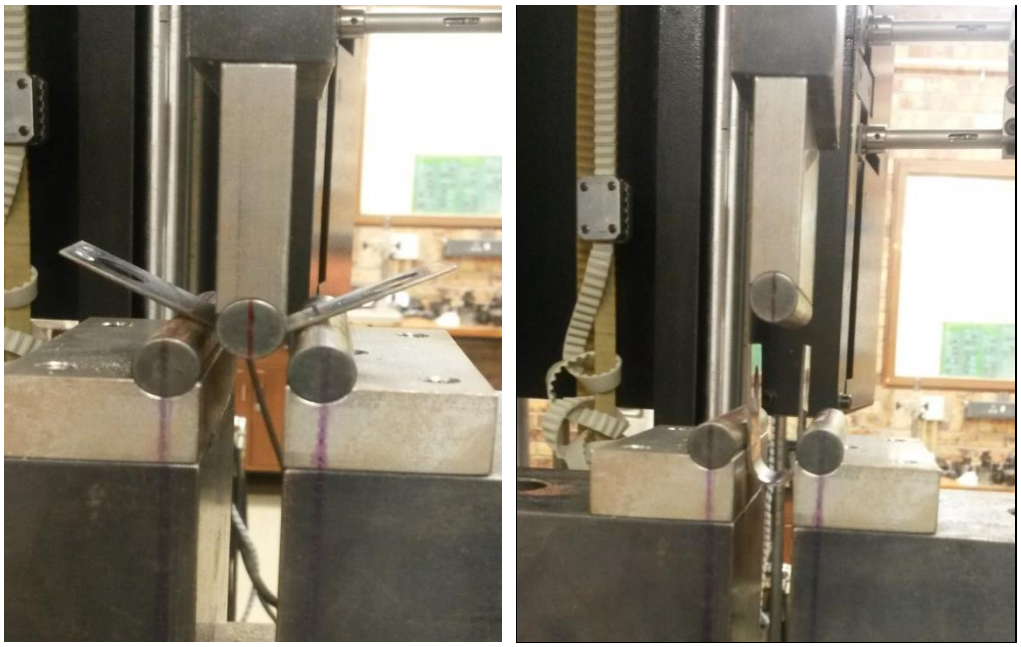

Figure 3-8: Fabrication of U-bend samples in a tension testing machine, stage 1 of 2 stage stressing method

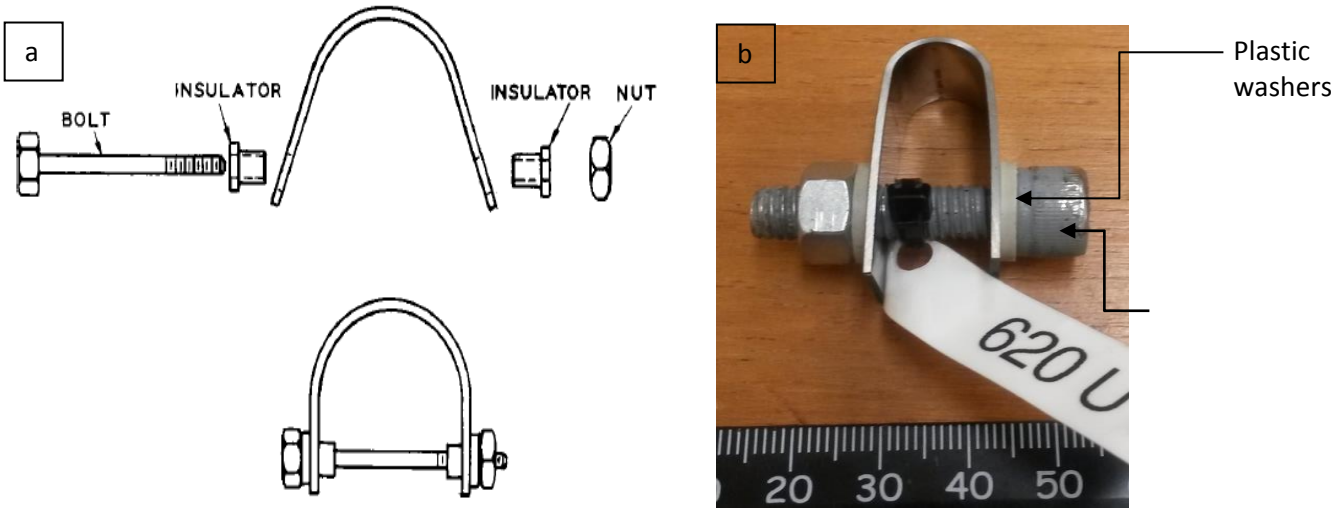

Figure 3-9: a) 2-stage stressing method [63] ; b) final U-bend specimen

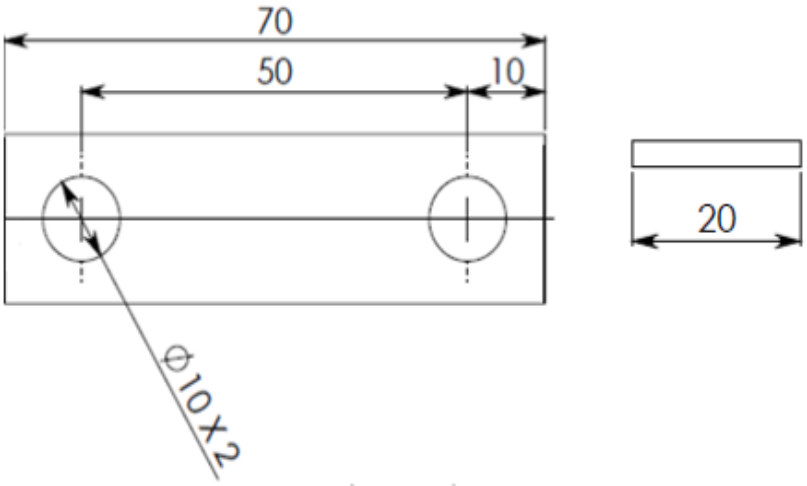

Figure 3-10: Specimen dimensions for U-bend samples

Heat Treatment	Surface Roughness Measurement (µm)		
	Reference specimen	6.07	
	Reference specimen measurement	5.81	
	Test 1	**Test 2**	**Test 3**
480°C	0.11	0.19	-
550°C	0.10	0.15	0.19
560°C	0.19	0.14	0.16
570°C	0.28	0.15	-
580°C	0.21	0.16	-
590°C	0.07	0.12	-
600°C	0.11	0.19	-
620°C	0.09	0.14	-

Table 3-3: Surface roughness of U-bend test specimens

The total strain on the outside on the bend, as evaluated from equation 3-1, is given in Table 3-4

T = Specimen thickness; R = Bend radius

Heat Treatment (°C)	Test 1			Test 2			Test 3		
	T (mm)	R (mm)	ε	T (mm)	R (mm)	ε	T (mm)	R (mm)	ε
480	1	6.5	0.08	1.1	6.5	0.08			
550	0.9	6.5	0.07	1	6.5	0.08	0.98	6.5	0.08
560	1.1	6.5	0.08	1.1	6.7	0.08	1	6.6	0.08
570	1	6.6	0.08	1	6.6	0.08			
580	1.1	6.5	0.08	1	6.6	0.08			
590	1.1	6.7	0.08	1.1	6.5	0.09			
600	1	6.2	0.08	1	6.5	0.08			
620	1.1	6.4	0.09	1	6.7	0.08			

Table 3-4: Calculated total strain on the U-bend samples

3.5.2.2. Test procedure

U-bend specimens described above were used for the SCC susceptibility tests. Samples were degreased ultrasonically prior to testing and inspected under a light microscope at a magnification of 5X for cracks and defects. Specimens were immersed continuously in 3.5% NaCl solution at a temperature of 90±2°C. Solution test temperature and pH were monitored daily.

The solution volume to sample surface area used is 15:1. Specimens were periodically removed for a maximum duration of 30 minutes and examined under the light microscope at a magnification of 5X for crack initiation and growth. The frequency of inspection was:

a) Twice a day for the first 7days;
b) Daily for the following 7 days;
c) Every 48 hours for the following 7 days; and
d) And weekly thereafter

The error in the time to failure readings of the U-bend specimens will be directly related to the frequency of the inspections. After SCC failure specimens were removed from the environment cleaned and examined. The fracture surface was examined optically using a Leica DFC 280 light microscope and a Nova NanoSem 230. The results are presented in section 4.4. The mechanism of SCC failure was additionally investigated using Electron Backscattered Diffraction (EBSD).

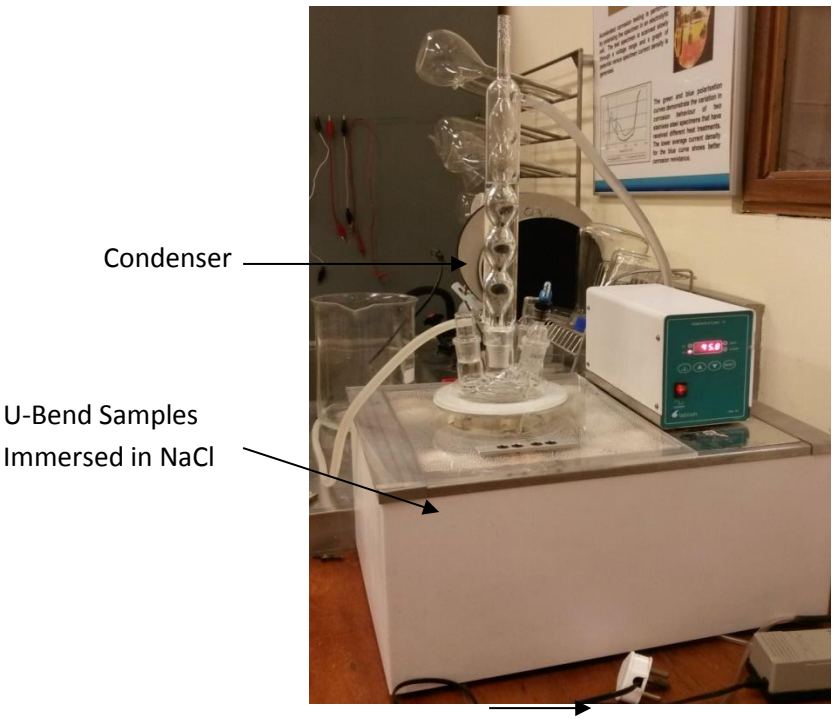

Figure 3-11: U-bend SCC testing rig

3.5.2.3. Data evaluation and analysis

The mechanism of SCC cracking was investigated using light microscopy, scanning electron microscopy and electron backscattered diffraction (EBSD).

EBSD is a characterisation technique which offers quantitative microstructural information regarding the crystallographic nature of metals, minerals, semi-conductors and steels. Grain size, grain boundary character, orientation texture and phase identification can be carried out using EBSD. [66]

EBSD is commonly used for SCC characterisation to distinguish between transgranular and intergranular SCC mechanisms. This is achieved with the use of Orientation Imaging Microscopy (OIM) and Image Quality (IQ) maps. For cracks propagating along grain boundaries EBSD is used to detect if there is a unique character shared by the cracked boundaries in relation to the overall distribution of grain boundaries. Misorientation angle distribution is frequently used in this aspect. OIM can be used to plot local orientation variations which are suggestive of the residual stress present in the material. These residual stress areas are possible initiation sites for SCC. [67]

EBSD was carried out using a Jeol JSM-700IF SEM. U-bend fracture samples were ground and polished as per Table 3-1. An accelerating voltage of 15kV with a probe current of 13 was utilised. EBSD data was analysed using *Channel 5, HKL Technology* software. Misorientation analysis was carried out along the crack path. Euler maps were plotted to distinguish between intergranular and transgranular SCC. Results are presented in section 4.4.1.8.

The 590°C tested U-bend sample was analysed using TEM as described in section 3.4.5. Samples were obtained using the FIB SEM and analysed. The U-bend samples exhibited crack growth in a direction perpendicular to the applied stress. The samples were obtained from the failed U-bend specimens with the applied stress perpendicular to the position of the specimens. The specimens were taken ahead of crack tips.

3.5.3. Threshold stress intensity testing

The relationship between stress intensity and crack growth rates were determined according to ASTM E1681(E)-03(2008). [9] Wedge open loading (WOL) specimens were utilised in the stress corrosion testing.

The WOL specimen belongs to a group of fracture mechanics specimens denoted as crack-line loaded (CLL) specimens. The WOL specimen was originally developed by Manjoine and Wessel. [68] [69] Modifications and studies of the original specimen design have been presented by various

researchers. [70] [71] The WOL specimen design used in this study was developed by Novak and Rolfe. [71] Various inter-laboratory studies have shown this specimen to be suitable for determining the relationship between stress intensity factor and crack growth rate in high strength steels. [72] [73]

The WOL specimen is a crack arrest type of SCC test sample. In a crack arrest type of specimen the crack opening displacement (COD) is maintained at a constant level by a bolt. As the crack growth develops the load, crack tip stress intensity and the crack growth rate decrease. The stress intensity decreases from the initial applied value (K_{10}) to the threshold stress intensity (K_{1SCC}). [71] [53] The initial stress intensity (K_{10}) applied exceeds the threshold stress intensity (K_{1SCC}) therefore crack growth rate is initiated rapidly, this decreases the total test time. A disadvantage of the WOL specimen is if the initial applied K_{10} is below K_{1SCC} there will be no determinable crack growth rate leading to extensive testing durations.

The specimen is self-loading by means of a bolt. Self-loading allows a great number of specimens to be tested simultaneously eliminating the need for the multiple expensive equipment. A minimum number of specimens are required to determine the relationship between the stress intensity factor and crack growth rate. This is beneficial economically, logistically and reduces the total test time required.

Two specimens per heat treatment level were tested for reproducibility.

3.5.3.1. Specimen geometry, fabrication and preparation

The fracture mechanics properties of the specimen are determined by the height: width (H/W) ratio and the method of loading of the specimen. The compliance of the specimen remains constant for a known H/W ratio irrespective of the individual specimen H/W dimensions. [70] Specimens with an H/W ratio 0.486 were used in the testing. For valid measurements of stress intensity it is recommended the ratio of the specimen width to breath is 2:1 ($1 \leq W/B \leq 2$). [9] Further dimensional constraints are discussed under the subsection data evaluation and analysis. A sample thickness of 11 mm was utilised.

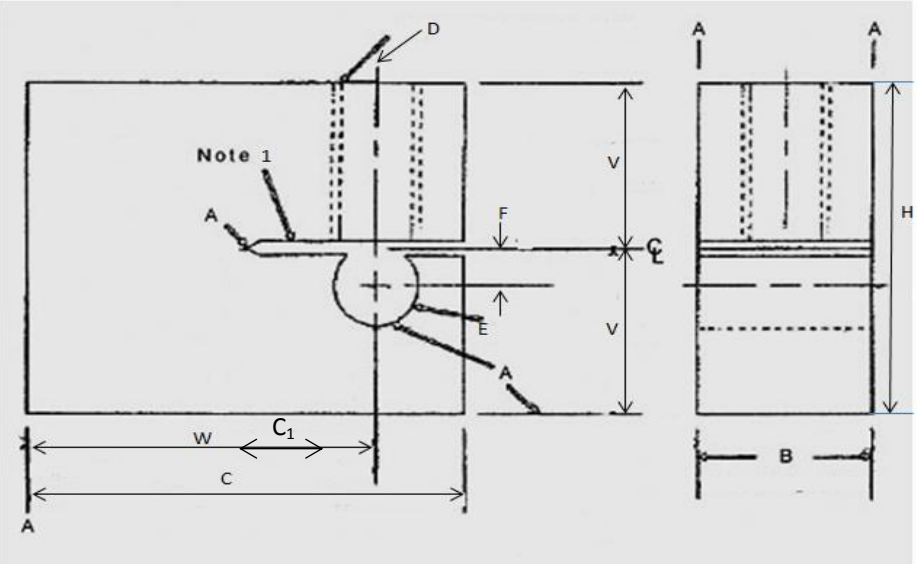

Figure 3-12: Dimension of WOL specimen (H/W=0.486) [65]

Figure 3-13: Loading Tup for WOL specimen

Specimens were manufactured from the root of FV566 turbine blades. The notch was machined using electric discharge machining (EDM). The notch was orientated as per section 3.2. The loading tup and bolt were manufactured from FV566 to prevent crevice corrosion.

Heat treatment procedures were carried out before final surface preparation. WOL specimens were grinded to achieve a 2400 grit SiC finish and cleaned in an ultrasonic bath. One face of the specimen was scribed with 1mm markings to assist with crack growth readings.

3.5.3.2. Test Procedure (9) (72) (73)

Samples were fatigue precracked under cyclic loading with a R ratio of 0.1 in a ESH fatigue testing machine fitted with 150kN loading cell. Jigs were manufactured to enable to the WOL specimen to be fitted to the fatigue testing machine. The stress intensity of the final 1mm of precrack should not

exceed 60% of the expected K_{1SCC} ($K_{PC} \leq 0.6K_{1SCC}$). [65] This can lead to extended periods of fatigue precracking. A K-decreasing or force shedding method was thus used for fatigue precracking. An initial precracking stress intensity of 24MPa√m was used for the first 1mm of precracking. This was followed by a 10% reduction in stress intensity for each 1mm of subsequent crack growth. [74]

The precracking stress intensity is computed from: [71] [72]

$$K = \frac{P\sqrt{a}}{Bw}\left(30.96 - 195.8\left(\frac{a}{w}\right) + 730.6\left(\frac{a}{w}\right)^2 - 1186.3\left(\frac{a}{w}\right)^3 + 754.6\left(\frac{a}{w}\right)^4\right) \quad \text{Equation 3-2}$$

where *P*=applied load

a=crack length measured from loading line

B=specimen thickness

w=specimen width.

The precrack length was measured using a Leica DFC 280 light microscope. The average crack length (a_o) is measured from the two surfaces of the specimen. This value is used to calculate the crack mouth opening displacement (V_0) desired. The initial V_0 is computed from: [71] [72]

$$\boldsymbol{V_0 = \frac{K_{10}}{E}\sqrt{a_o}\frac{C_6\left(\frac{a_0}{W}\right)}{C_3\left(\frac{a_0}{W}\right)}} \quad \text{Equation 3-3}$$

Where $C_6\left(\frac{a}{w}\right) = exp\left[4.495 - 16.130\left(\frac{a}{w}\right) + 63.838\left(\frac{a}{w}\right)^2 - 89.125\left(\frac{a}{w}\right)^3 + 46.815\left(\frac{a}{w}\right)^4\right]$

$$C_3\left(\frac{a}{w}\right) = 30.96\left(\frac{a}{w}\right) - 195.8\left(\frac{a}{w}\right)^2 + 730.6\left(\frac{a}{w}\right)^3 - 1186.3\left(\frac{a}{w}\right)^4 + 754.6\left(\frac{a}{w}\right)^5$$

K_{10}=Desired starting stress intensity

E=Young's Modulus

a_0=initial crack length as measure from loading line.

The K_{10} level to be applied was determined with the use of the tensile strength data as well experimentally. The V_0 values for each heat treatment varied. The in values are listed in Appendix C on page 139.

The loading bolt and tup are coated with petroleum jelly. The sides of the specimen are affixed with plumbers tape to protect the specimen from damage. Knife edges are attached to the specimen. The

specimen is bolt-loaded to the calculated V_0 using a calibrated clip gauge. The sample is then immersed in the test solution.

Figure 3-14: Precracking of the WOL specimen

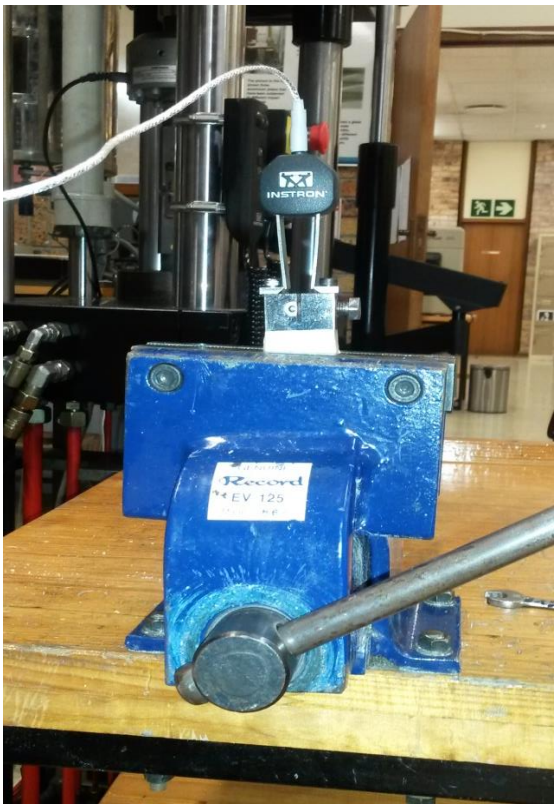

Figure 3-15: Loading of WOL samples with the use of a calibrated clip gauge

Samples were removed periodically for a maximum period of 30 minutes to measure crack growth. Crack growth was measured optically with the use of a Leica DFC 280 light microscope. The frequency of inspection was:

a) Twice a day for the first 7days;
b) Daily for the following 7 days;
c) Every 48 hours for the following 7 days;
d) And weekly thereafter.

The crack lengths represent averages of measurements on the two specimen surfaces.

Tests were terminated when the crack growth rate was less than 10^{-4}mm/h or the final crack length (a_f) was greater than 0.8w. At test termination the change in crack mouth opening displacement is measured from the loaded to the unloaded state. The specimens are subsequently loaded in a

fatigue testing machine to the measured crack opening displacement and the load recorded. This final load (P_f) is used to compute K_{1SCC}.

3.5.3.3. Data evaluation and analysis [9] [72] [73]

Compliance equations are available for analysis for the WOL specimen. The applied load during the SCC test is computed using these equations. A rigid bolt analysis assumes the crack mouth opening displacement at the loading remains constant for the duration of the test. The applied load is computed from:

$$P_i = \left[\left(\frac{a_0}{a_i}\right)\left(\frac{a_i + C_1}{a_0 + C_1}\right)\right]\frac{EBV_0}{C_6\left(\frac{a_i}{W}\right)}$$ Equation 3-4

where P_i = instantaneous load

a_0=initial crack length measured from loading line

a_i=instantaneous crack length measured from loading line

B=specimen thickness

W=specimen width

C_1= defined in Figure 3-12.

The stress intensity calculations are valid provided plain strain conditions are present at the crack tip. The WOL specimen dimensions and crack length must specific requirements are listed in ASTM1681 (E)-03. [9] These requirements are listed below:

a) $B, a \geq 2.5(K_{1SCC}/\sigma_y)$

b) $0.45 \leq a_f/W \leq 0.80$

c) $W-a \geq 2.5(K_{1SCC}/\sigma_y)$

Where σ_y is the specimen yield strength.

4. Results

4.1. Overview of material testing and characterisation

FV566 LP turbine blade material was studied to determine the change in mechanical and SCC behaviour after heat treatment at various tempering temperatures. Changes in microstructure associated with the heat treatment were also investigated.

Hardness and tensile tests were carried out to characterise the mechanical behaviour. SCC testing was achieved with the use of U-bend and Wedge Open Loading samples – to determine the SCC cracking mechanism and crack propagation rates as a function of stress intensity.

Light microscopy, SEM imaging, EBSD and TEM, were utilised to analyse the cracking morphology and material microstructure.

4.2. Mechanical testing

4.2.1. Hardness Value (HV) testing

Hardness value testing was carried out – as described in section 3.3.1. The experimental findings are presented below.

Vickers hardness values decrease with increased tempering temperature. The hardness decreases from an average value of 480 HV to 355 HV at tempering temperatures of 480°C and 620°C respectively.

This typical decrease in the hardness value is attributed to the effect of secondary hardening in chromium-rich martensitic steels – and which occurs during tempering. The solid solution strengthening of the material which occurs before tempering is replaced by precipitation strengthening during tempering. [13] This leads to softening of the material and a decrease in hardness values, as the tempering temperature increases.

Tempering temperature (°C)	HV1 (30kg)	HV2 (30kg)	HV3 (30kg)	HV4 (30kg)	Estimated average hardness HV (30kg)	95% Confidence Interval
480	476	484	482	479	480	3.4
550	440	445	445	433	441	5.6
560	451	447	441	450	447	4.4
570	402	416	406	411	409	6.0
580	398	395	392	392	394	2.8
590	387	383	377	382	382	4.0
600	378	373	368	372	373	4.9
620	358	353	352	359	355	3.4

Table 4-1: Vickers hardness values for FV566 stainless steel – as a function of tempering temperature measured at room temperature. The 95% confidence interval values are referenced above.

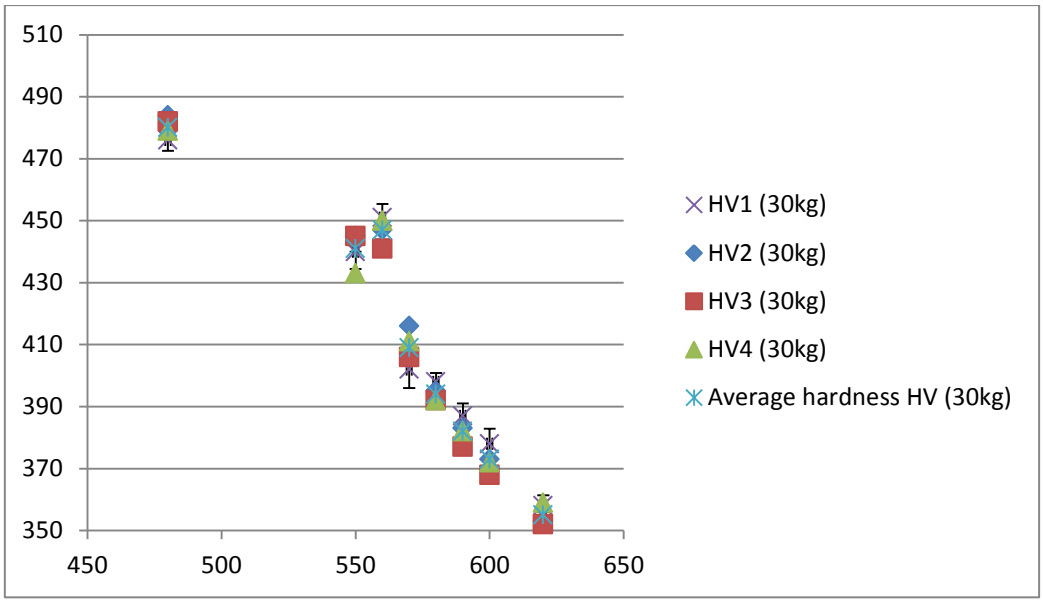

Figure 4-1: Tempering temperature versus average Vickers hardness – showing the softening of the material as the tempering temperature increases

4.2.2. Tensile testing

Tensile testing was carried out as per experimental procedure 3.1.2. All tensile specimens were strained to failure. The variations of the 0.2% proof strength with tempering temperature are summarised below.

The 0.2% proof strength of the material decreases with an increase in tempering temperature. The 0.2% proof strength decreases from an average of 1136.1 MPa to 925.0MPa at tempering temperatures of 480°C and 620°C respectively. This decrease in strength is associated with an increase in ductility and toughness – which occurs during tempering.

The values of the tensile tests were utilised in determining the starting stress intensity (K_{10}) for the stress corrosion testing.

Heat treatment (°C)	Test 1		Test 2		Average	
	0.2% PS (MPa)	UTS	0.2% PS (MPa)	UTS	0.2% PS (MPa)	UTS
480	1132.2	1376.6	1140.0	1386.1	1136.1	1381.4
550	995.1	1226.4	1013.5	1249.1	1004.3	1237.7
560	924.8	1195.8	1071,0	1384.8	997.9	1290.3
570	946.3	1223.3	1068.4	1381.1	1007.4	1302.2
580	831.9	1149.5	833.2	1151.2	832.6	1150.4
590	950.2	1153.6	970.0	1177.6	960.1	1165.6
600	930.0	1097.5	950.0	1121.1	940.0	1109.3
620	920.0	1013.0	930.0	1024.0	925.0	1018.5

Table 4-2: Tensile strength of FV566 as a function of temperature

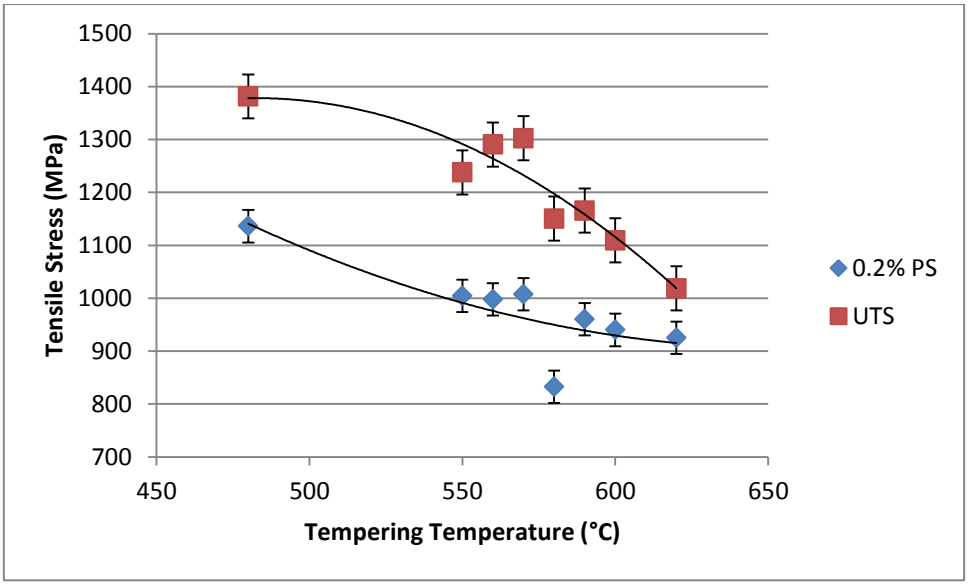

Figure 4-2: Change in Proof and Ultimate Tensile Strength with Tempering Temperature

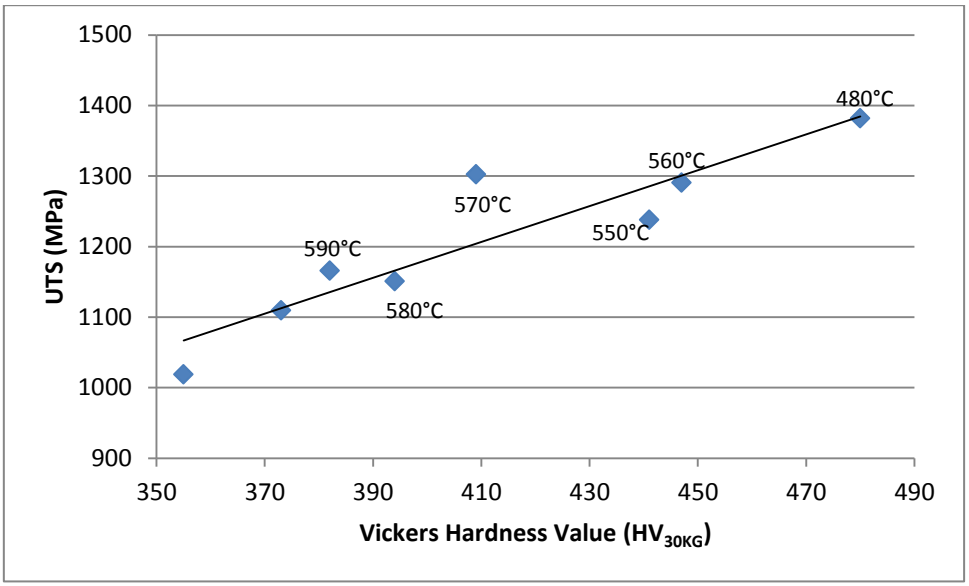

Figure 4-3: Correlation between Hardness Values and Ultimate Tensile Strength

4.3. Microstructural characterisation

Light and electron microscopy were used to analyse the material microstructure before stress corrosion testing. Variation of material microstructure attributed to the tempering procedure was investigated, and the results are presented below.

4.3.1. Material microstructure

The microstructure of the as received material which was used in service at the Eskom power fleet was investigated using conventional light microscopy and EBSD investigation. The microstructure of FV566 was determined as tempered martensite with aluminium oxide and manganese sulphide inclusions. The inclusion content is listed below, in detail, in section 4.3.2. See Figure 4-4 and Figure 4-5.

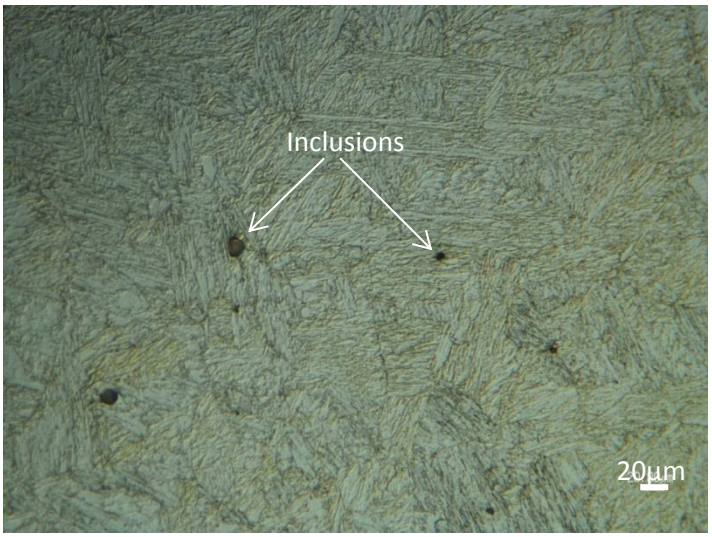

Figure 4-4: Light micrograph image of FV566 as received material from the power plant, etched with Villella's reagent, and showing the tempered martensite microstructure and inclusions

Prior austenite grain boundaries can be identified visually from the EBSD Euler map – as seen in Figure 4-5. Misorientation angles were calculated using *HKL channel 5 software* [76] across the grain boundaries – to distinguish between prior austenite grain boundaries and martensite lath boundaries.

There were no discernible differences visible in the microstructure of the different heat treatments. Carbide precipitates were not identifiable using the SEM. Carbide extraction replica and the TEM were used to further analyse the microstructure for identification of the precipitates. The elemental analysis of the different heat treatments did not vary significantly.

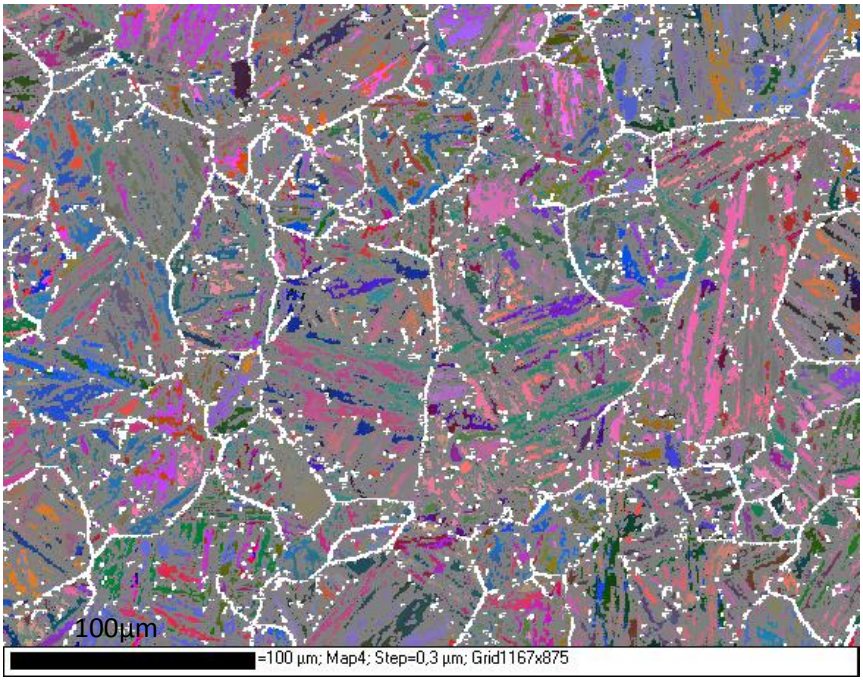

Figure 4-5: All Euler Map of as received turbine blade at 20 keV. Grain boundaries between 17° and 40° are shaded white, and represent the prior austenite grain boundaries in the martensitic steel FV566.

The root of the turbine blade used for experimentation was investigated for grain orientation directionality. There was no evidence of directionality in grains from light microscopy and EBSD data. Furthermore, the inclusion content of the steel did not exhibit any directionality.

4.3.2. Inclusion content elemental analysis

Elemental analysis was carried out to identify the inclusion content present in the steel using EDS. The analysis was carried out on the as received root of the turbine blade. The inclusions were identified to be most likely aluminium oxide and manganese sulphide as shown in Figure 4-6 and Figure 4-7. The EDS beam not only excited the inclusion but also the background material.

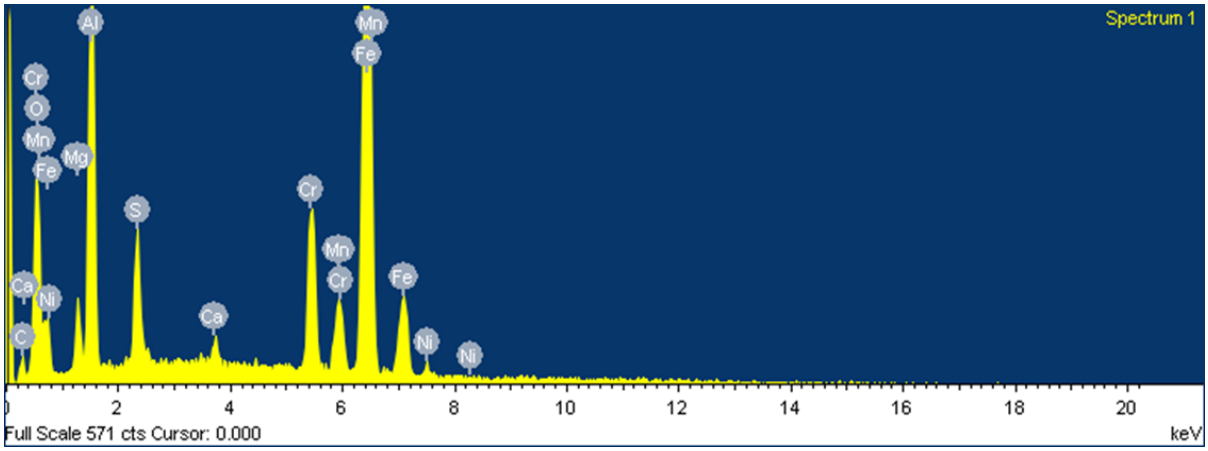

Figure 4-6: SEM EDS analysis of inclusion content on as received FV566 turbine steel – which indicates the presence of aluminium oxide (AlO) inclusions. Area scanned = 40µm x 50µm

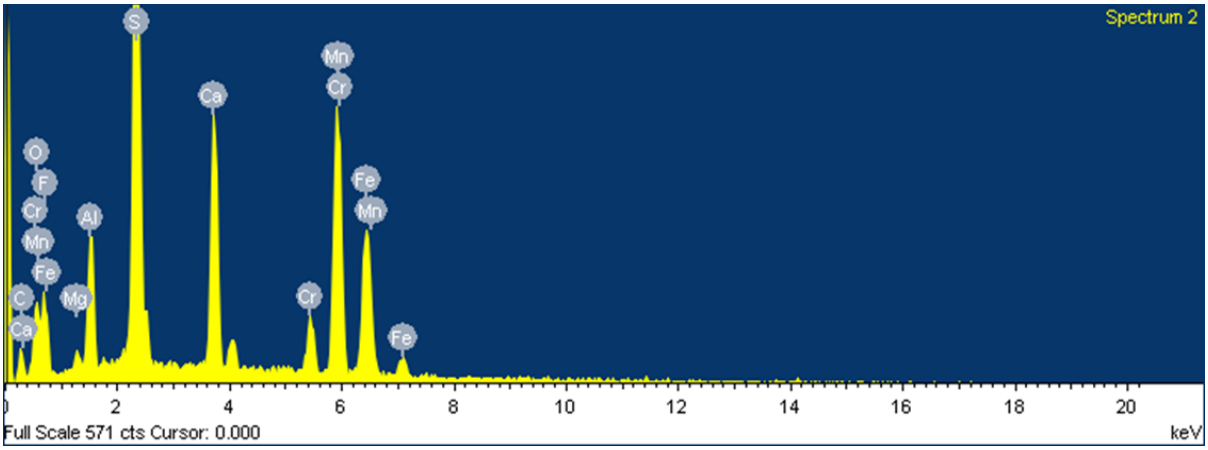

Figure 4-7: SEM EDS analysis of inclusion content on as received FV566 turbine steel – which indicates the presence of manganese sulphide (MnS) inclusions (40µm X50µm)

4.3.3. Precipitate characterisation using Transmission Electron Microscopy [61]

Transmission electron microscopy was undertaken on heat-treated samples to analyse the effect of tempering on the formation and location of precipitates. FIB samples were taken across prior austenite grain boundaries for the 550, 580 and 600°C temper samples. CER were taken for all the heat treatments – except the 570°C temper specimen.

For the TEM samples obtained using CER without the sectioning of the iron matrix, the following results were obtained: The size of the precipitates increased as the tempering temperature increased; these results were based on the limited number of samples and areas investigated. The main types of precipitates identified from the CER samples were: Al-N, Cr-rich $M_{23}C_6$ clustered together, Cr-rich $M_{23}C_6$ platelet precipitates, and Cr rich precipitates which were not identified. The results are summarised below in Table 4-3 on page 75.

The precipitate density and type varied for each treatment. Results between replicas from the same specimen also displayed variability. The results of the carbon extraction replicas are presented below in Figure 4-8 to Figure 4-14 on pages 75-77.

For the 480°C temper specimen, no precipitates were detected. Si-O was detected on the surface – possibly as a result from manufacturing or contamination. For the 550°C specimens, AlN inclusions were discovered. This agrees with the SEM elemental analysis in section 4.3.2. $M_{23}C_6$ clustered precipitates were observed in isolated areas for the 550°C temper specimen.

For the 560°C temper specimen AlN precipitates were found primarily in the matrix – with isolated areas in the matrix containing $M_{23}C_6$ clustered precipitates and Cr-rich $M_{23}C_6$ platelet precipitates. The 580°C temper specimen contained AlN particles and type C Cr-rich $M_{23}C_6$ platelet precipitates, with Cr-rich precipitates at the grain boundaries which were not identified.

The 590°C temper specimen contained AlN particles and primarily Cr-rich $M_{23}C_6$ platelet precipitates, with Cr-rich precipitates at the grain boundaries which were not identified.

The 600°C temper specimen contained primarily $M_{23}C_6$ clustered precipitates and Cr-rich $M_{23}C_6$ platelet precipitates, with Cr-rich precipitates at the grain boundaries which were not identified.

The 620°C temper specimen contained primarily Cr-rich precipitates aligning preferentially at the grain boundaries, in addition to Cr-rich $M_{23}C_6$ platelet precipitates distributed throughout the matrix of the specimen.

Sample	Al-N	$M_{23}C_6$ clustered precipitates	$M_{23}C_6$ platelet precipitates	Cr-rich unidentified precipitates
480	None	None	None	None
550	Primarily noted	Sparsely noted	None	None
560	Primarily noted	Sparsely noted	Sparsely noted	None
580	Sparsely noted	None	Primarily noted	Sparsely noted
590	Sparsely noted	None	Primarily noted	Sparsely noted
600	None	Primarily noted	Primarily noted	Sparsely noted

620	None	None	Primarily noted	Primarily noted

Table 4-3: Summary of precipitates noted for CER samples of the different temper specimens

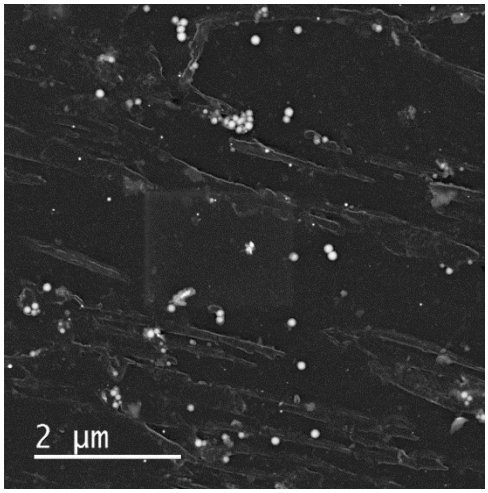

Figure 4-8: HAADF-STEM image of 480°C temper specimen, showing no precipitates other than Si-O particles on surface due to possible contamination

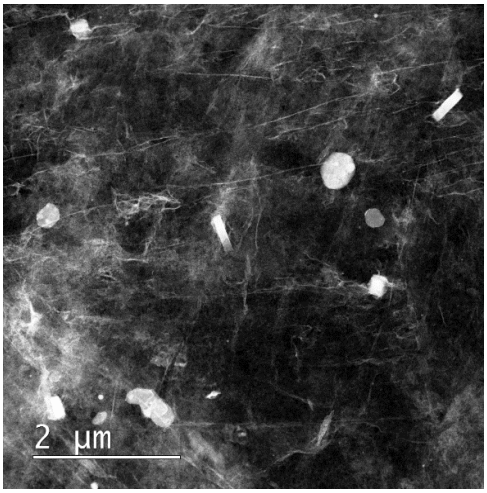

Figure 4-9: HAADF-STEM image of 550°C temper specimen, showing AlN inclusion with isolated $M_{23}C_6$ clustered precipitates

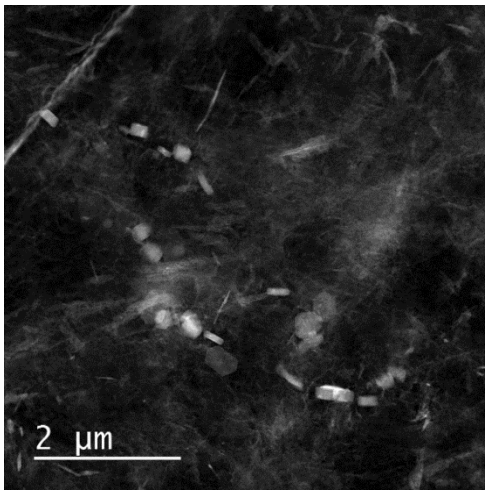

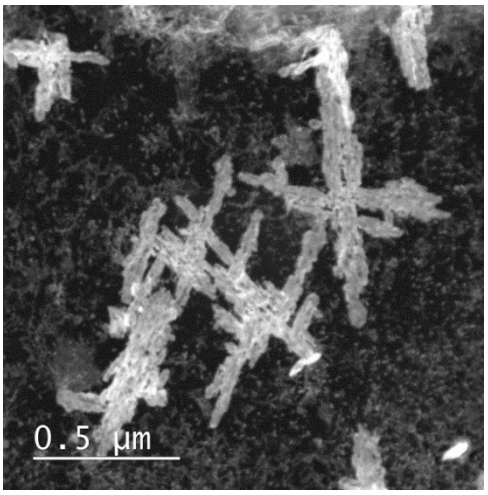

Figure 4-10: HAADF-STEM image of 560°C temper specimen, showing primarily AlN precipitates with isolated areas of $M_{23}C_6$ clustered precipitates and $M_{23}C_6$ platelet precipitates

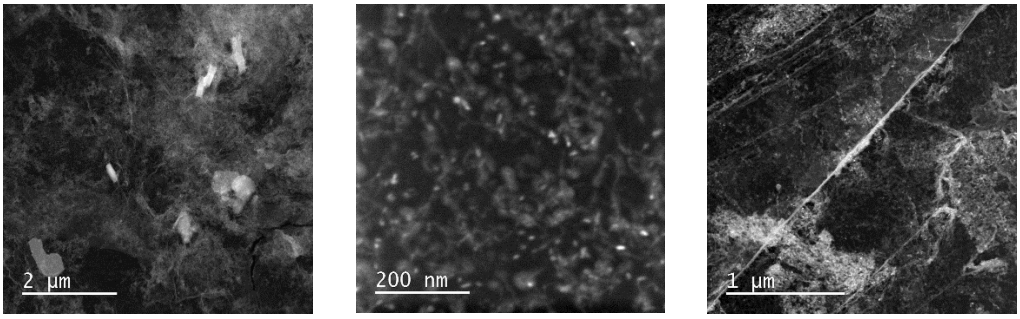

Figure 4-11: HAADF-STEM images of 580°C temper specimen, showing precipitates of primarily AlN + $M_{23}C_6$ platelet precipitates with Cr-rich precipitates at grain boundaries

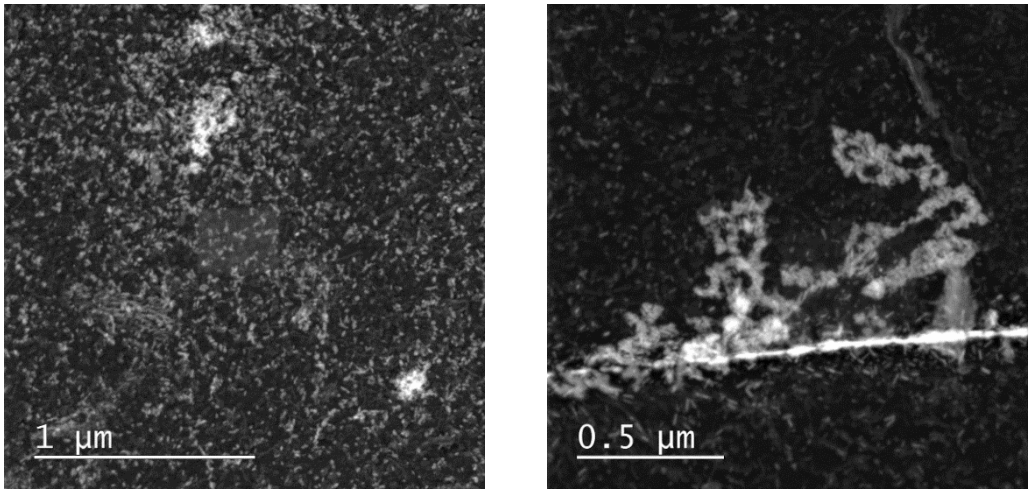

Figure 4-12: HAADF-STEM image of 590°C temper specimen, showing precipitates of primarily $M_{23}C_6$ platelet precipitates and AlN and Cr-rich precipitates at the grain boundary

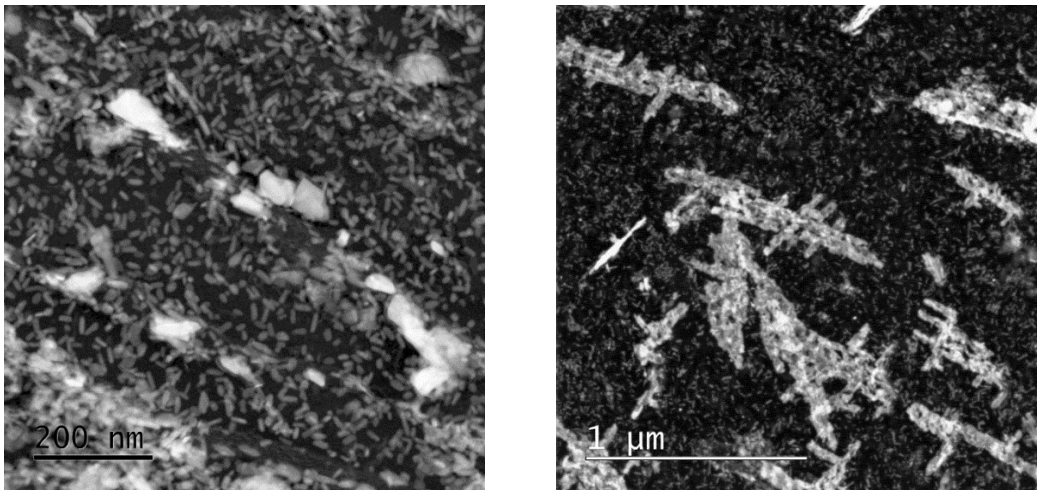

Figure 4-13: HAADF-STEM image of 600°C temper specimen, showing precipitates dominated by $M_{23}C_6$ platelet precipitates and $M_{23}C_6$ clustered precipitates, and with Cr-rich precipitates along the grain boundary

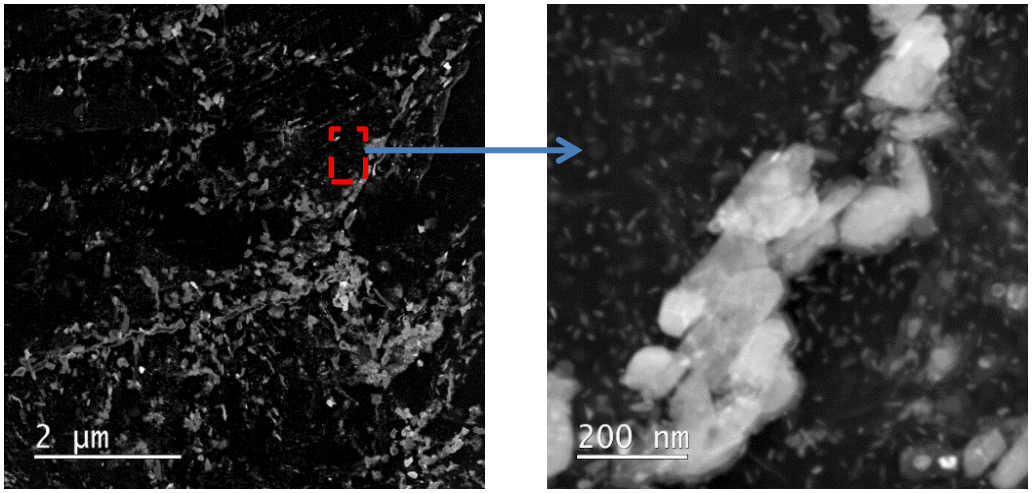

Figure 4-14: HAADF-STEM image of 620°C, showing structure dominated by Cr-rich precipitates aligning preferentially at the grain boundary – in addition to $M_{23}C_6$ platelet precipitates distributed throughout the sample

FIB samples were taken on heat-treated samples to analyse the precipitate noted from CER. Results obtained for samples acquired using the FIB SEM are presented below. Figure 4-15 shows the location of the TEM sample taken across the prior austenite grain boundary (a-c) and below the associated Cr-EFTEM map (d-e), showing the location of Cr-rich precipitates.

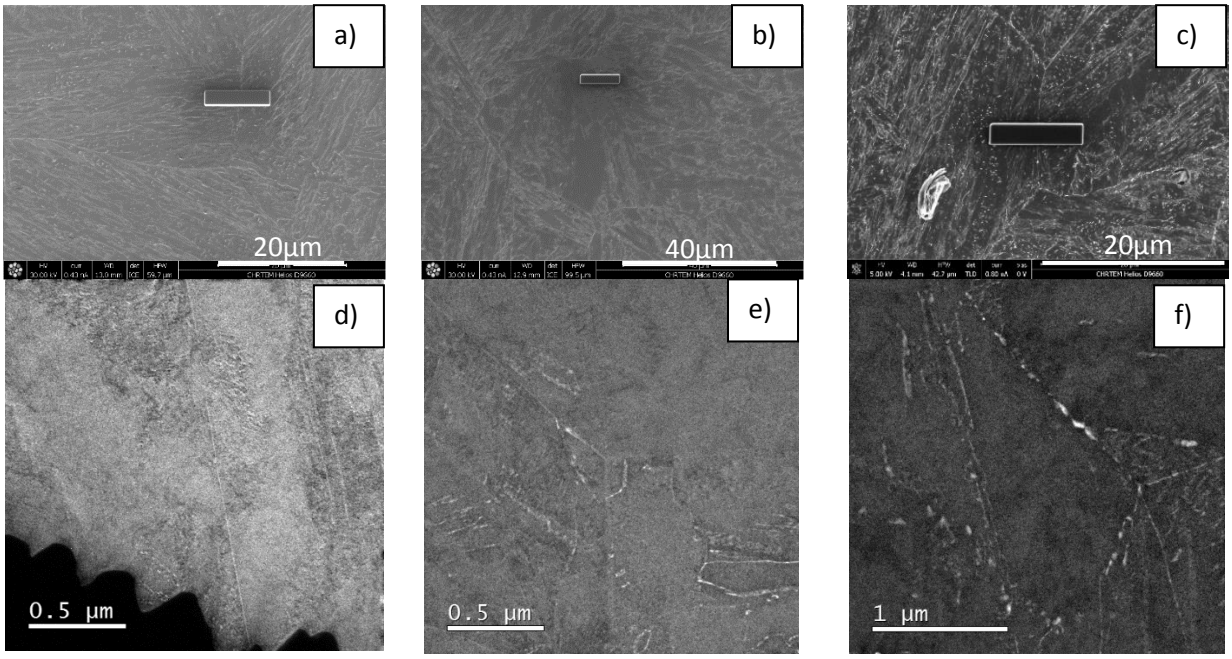

Figure 4-15: SEM Images showing the location of the TEM sample taken across a prior austenite grain and below the associated Cr-EFTEM map showing the location of Cr-rich precipitates for: a) & d) 550°C; b & e)580°C; and c & f)600°C specimens.

For the 550°C temper specimen a uniform chromium distribution was noted in the specimen matrix. For the 580°C temper specimen, chromium precipitates were noted along the sub-grain and grain boundaries. For the 600°C temper specimen, distinct chromium-rich precipitates were noted along the sub-grain boundaries – with larger precipitates noted along the prior austenite grain boundaries.

The precipitates were identified and measured using EDS. The 550°C and 560°C temper specimens consisted primarily of Al-N particles. The sizes of these particles typically ranged from 300nm to 100nm. These are the inclusions noted in section 4.3.2, which are formed as a result of the manufacturing process. These precipitates were not observed at the higher tempering temperatures.

The next type of precipitate which was noted, were the Cr-rich $M_{23}C_6$ clustered precipitates. EELS and EDS were used to analyse the composition of the precipitate, and the precipitates were Cr-rich. Analysis of these precipitates at higher magnitude showed that $M_{23}C_6$ clustered precipitates were composed of smaller elongated precipitates – joined together, as seen below in Figure 4-17 on page 73. The sizes of these precipitates were 200nm to 1500nm.

HRTEM and HRSTEM were used to determine the crystallographic information of these precipitates; analysis identified the precipitates to be $M_{23}C_6$ precipitates (F m-3 m: a_0 =10.607 Å) as shown in Figure 4-18 on page80.

The third type of precipitates analysed were distributed throughout the matrix of the samples were noted as $M_{23}C_6$ platelet precipitates. The size of the precipitates ranged from 10 to 30nm. The HRTEM, HAADF-STEM and power-spectrum analysis identified the precipitates as $M_{23}C_6$ – as shown in Figure 4-21 on page 75. To increase the sampling accuracy, a large area SAD ED pattern (500nm in diameter) was taken, as shown in Figure 4-20 on page 81. The VC (F m -3 m: a_0=4.172 Å) precipitate pattern matched the first two rings, but could not match the rest of the pattern. The $M_{23}C_6$ precipitate has many rings and therefore partially lines up with the experimental pattern.

Due to the uncertainty of the SAD analysis, several precipitates which were on or close to a zone axis were imaged using HRTEM. The FFT taken and the resulting power spectrum compared to simulated SAD patterns. In each case, a good match was found with the $M_{23}C_6$ precipitate and the VC possibility excluded due to the presence of large interplanar spacings.

In each case a good match to $M_{23}C_6$ precipitate was found. EDS and EELS analysis shown in Figure 4-23 on page 82 indicate that these precipitates consisted mainly of Cr. It is therefore concluded that the clustered structured of precipitates are comprised of these smaller platelet $M_{23}C_6$ precipitates.

The last precipitate which was analysed, consisted of a block-type precipitate which primarily was found on the grain boundaries of the material matrix. This precipitate was found mainly on samples tempered between 580°C and 620°C (predominately). Due to the substantial thickness of these particles, diffraction patterns could not be obtained during HRTEM imaging. The precipitate thickness ranged from 50nm to greater than 300nm. The size and quantity of the block-type precipitates increased with an increase in tempering temperature. Elemental analysis in Figure 4-23 and Figure 4-25 on page 84, shows that the precipitates were composed mainly of Cr, with some Fe.

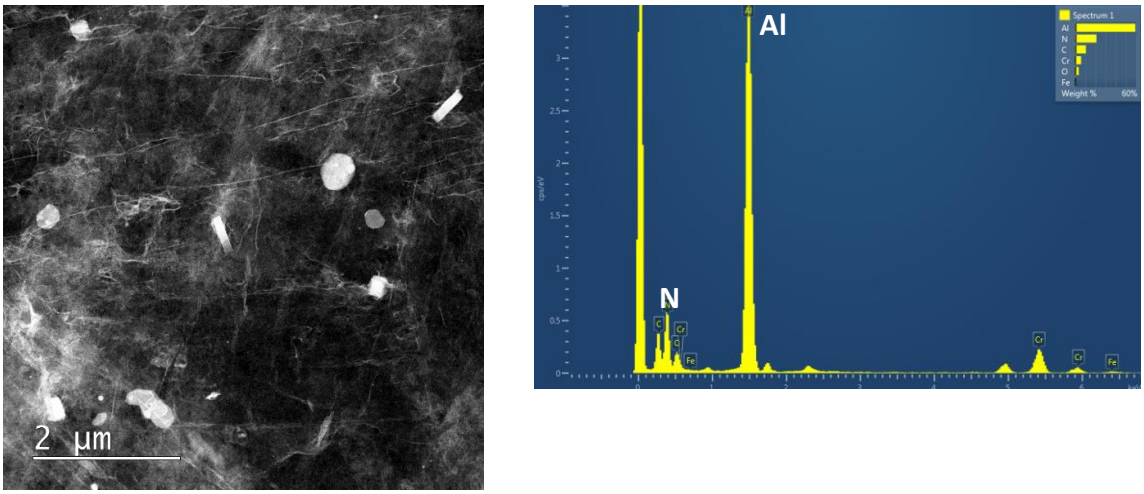

Figure 4-16: HAADF-STEM image of AlN precipitate, and EDS spectrum showing the dominance of Al-N

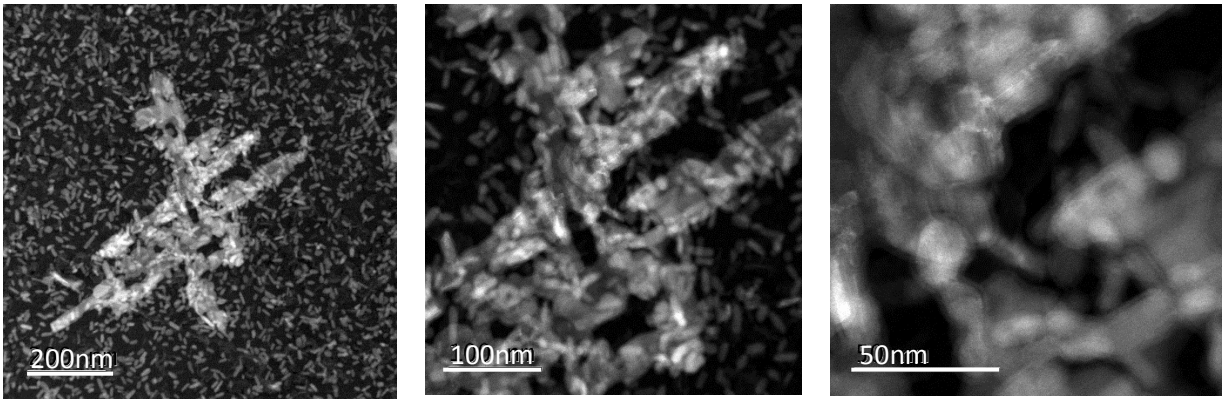

Figure 4-17: HAADF-STEM images, showing the composite structure of the $M_{23}C_6$ platelet precipitates

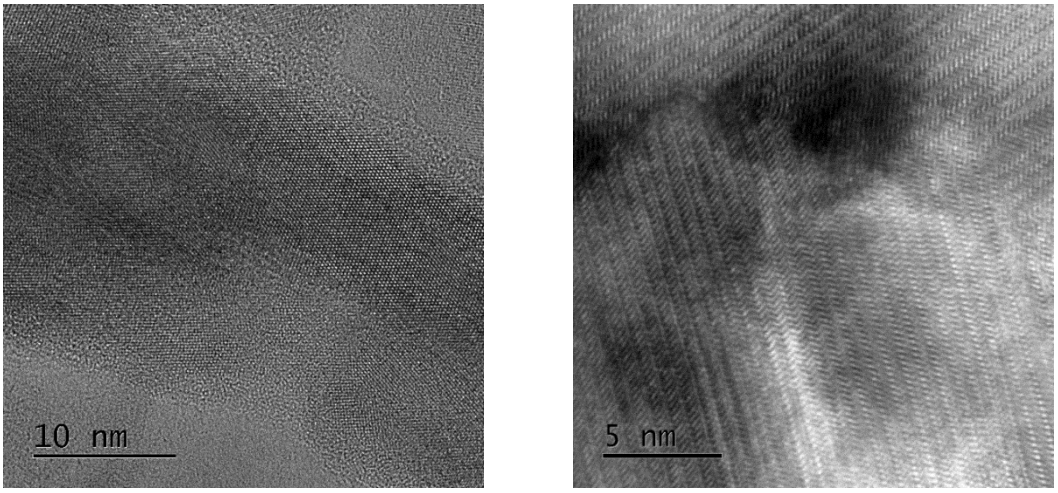

Figure 4-18: HRTEM and HAADF-HRSTEM images of the $M_{23}C_6$ clustered precipitates

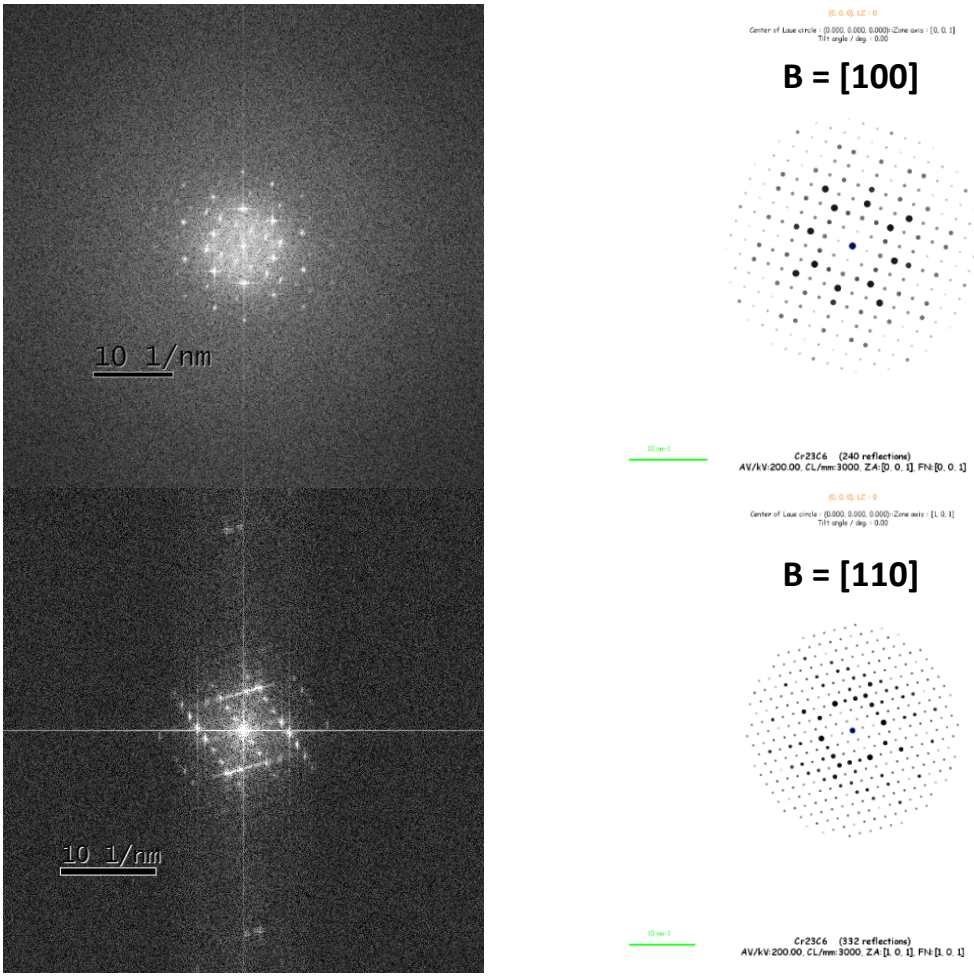

FFT of HR-images Simulated JEMS SAD patterns

Figure 4-19: FFT of the images showing the power spectrum and matched JEMS diffraction patterns – illustrating that the precipitate matches a $M_{23}C_6$ crystal structure.

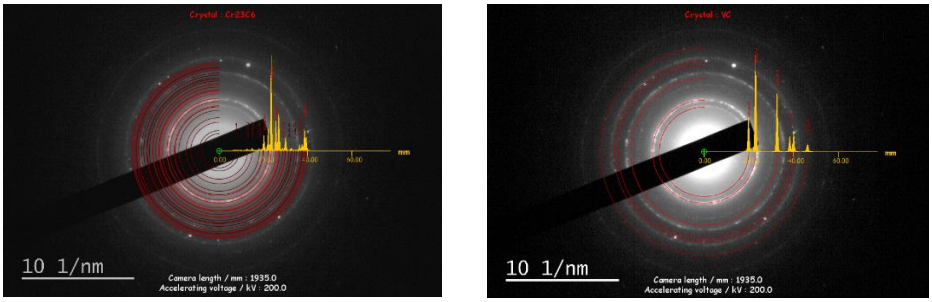

Figure 4-20: SAD of "rice" precipitates does not fully match VC, and partially matches $M_{23}C_6$

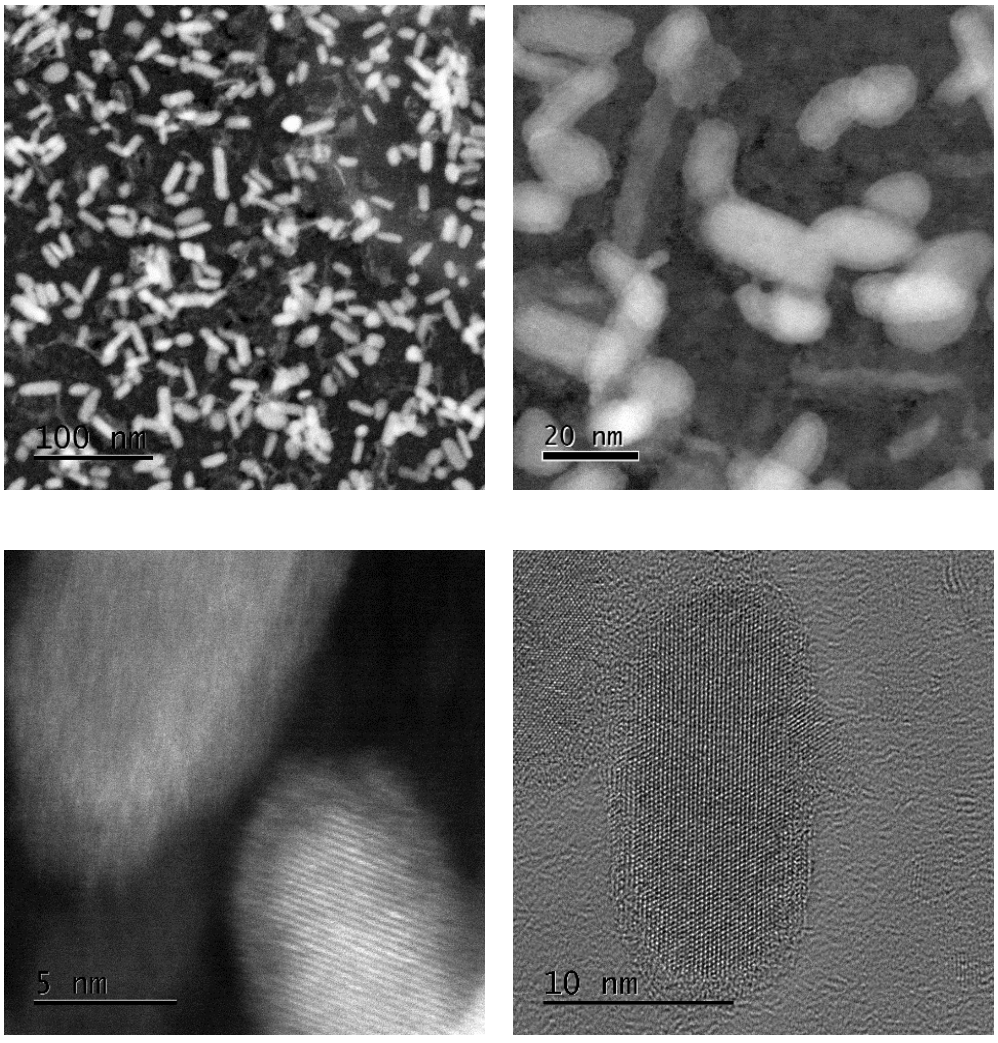

Figure 4-21: HAADF-STEM and HRTEM images of the $M_{23}C_6$ platelet precipitates

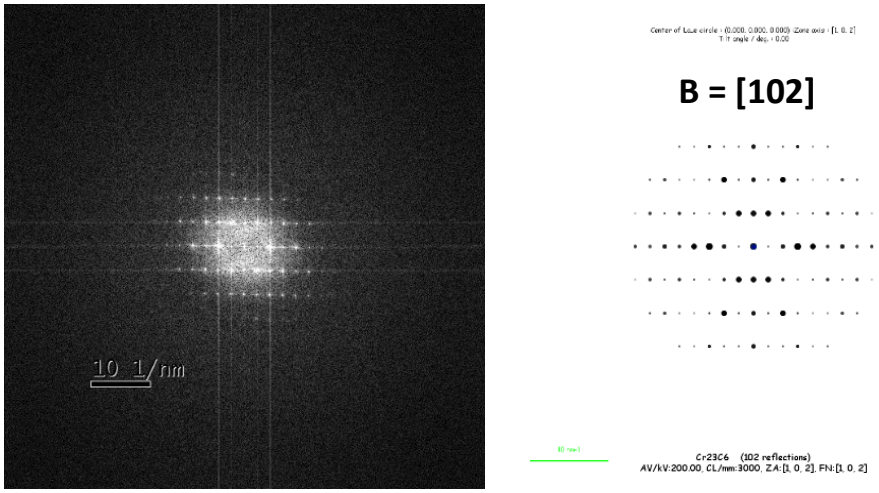

Figure 4-22: Power spectrum (FFT of HRTEM image) from one precipitate and simulated JEMS SAD pattern

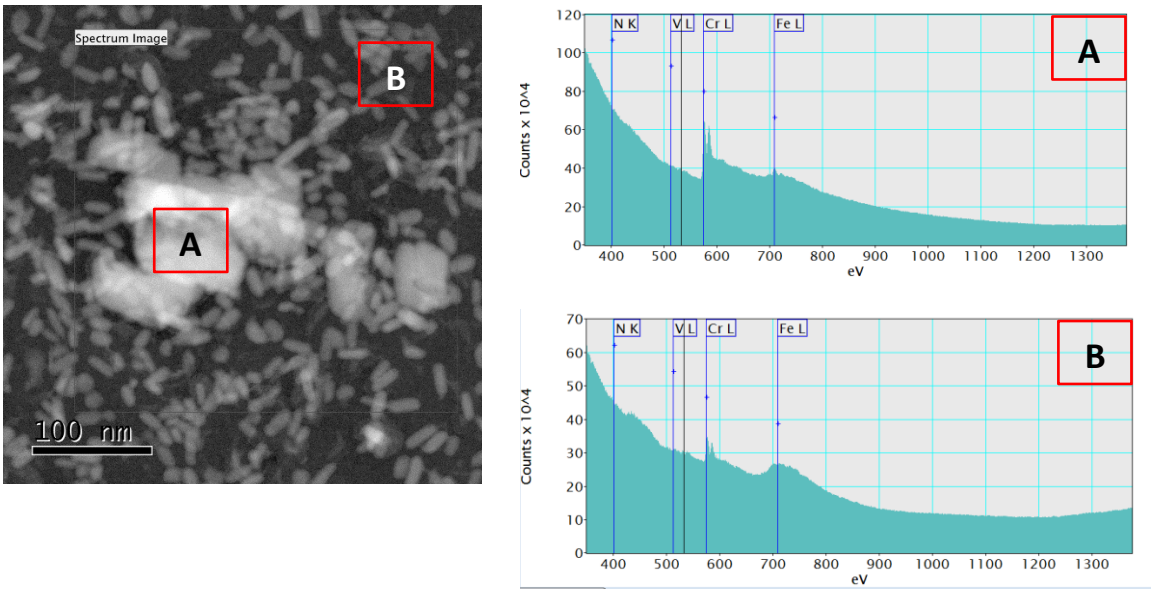

Figure 4-23: HAADF-STEM EELS elemental analysis of the $M_{23}C_6$ clustered precipitates and $M_{23}C_6$ platelet precipitates

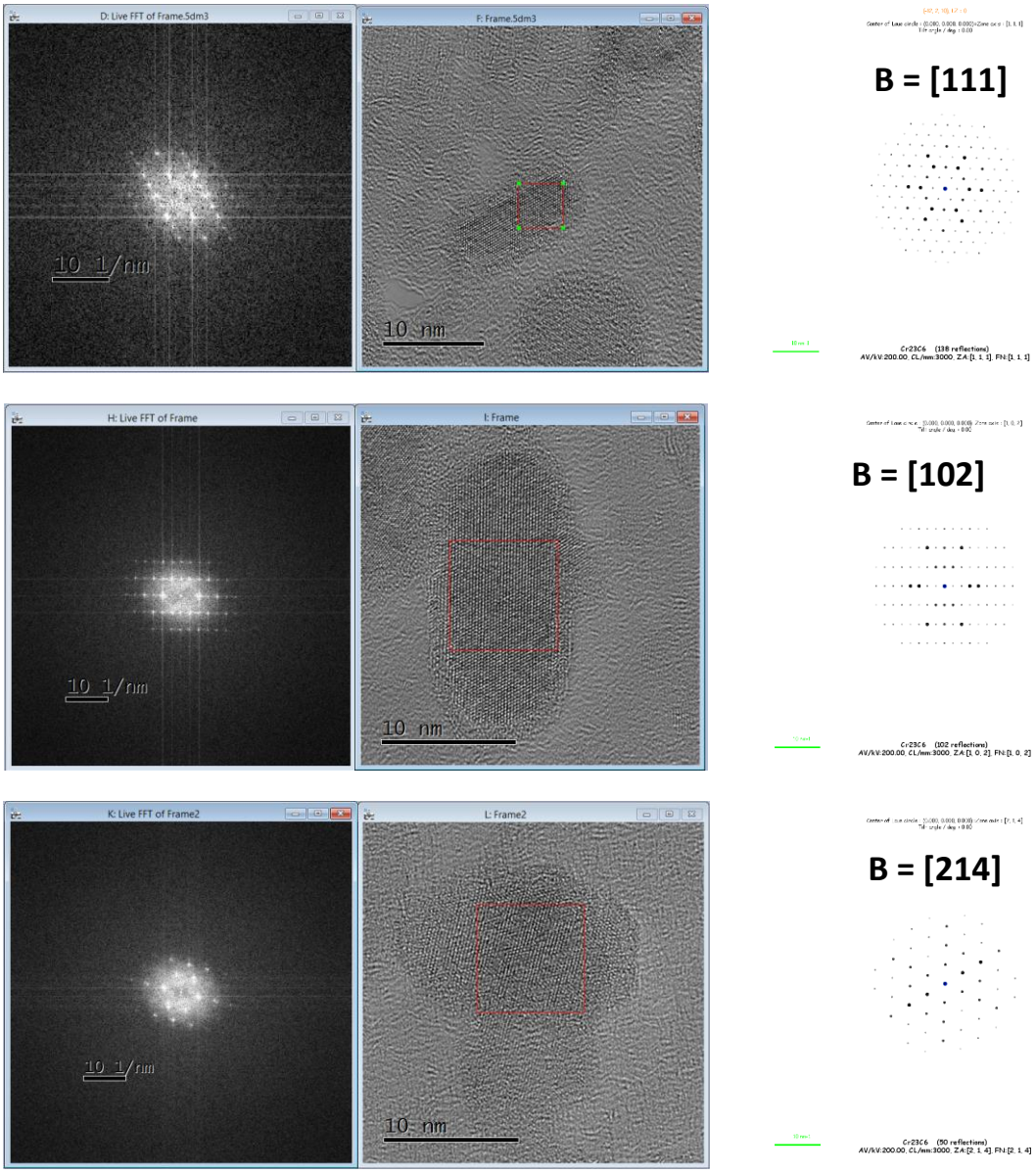

FFT (power spectrum) and HRTEM images | Simulated JEMS SAD

Figure 4-24: Three different platelet precipitates imaged with HRTEM, and comparison between power spectrum and simulated diffraction pattern – matching well with $M_{23}C_6$ types

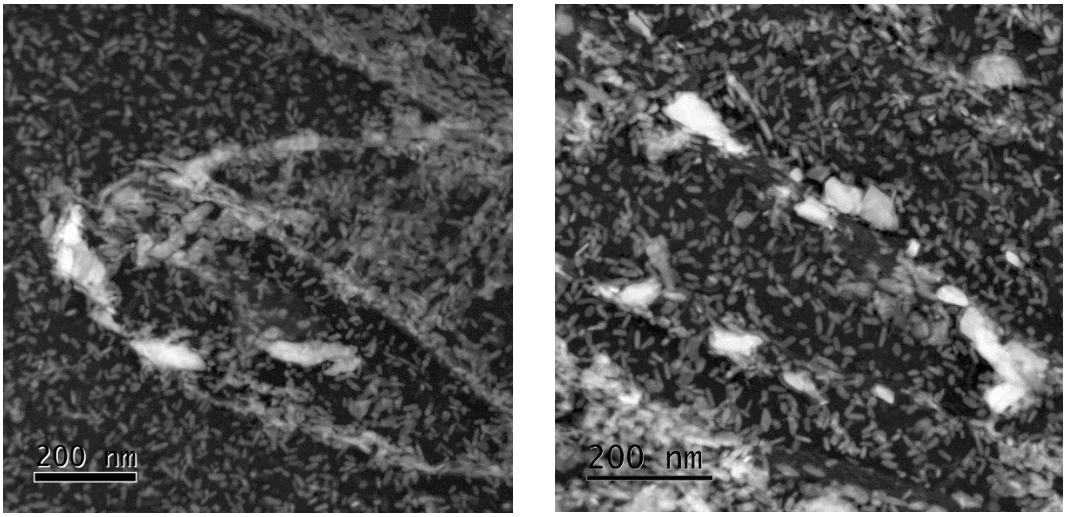

Figure 4-25: HAADF-STEM images of the Cr-rich precipitates at the grain boundaries

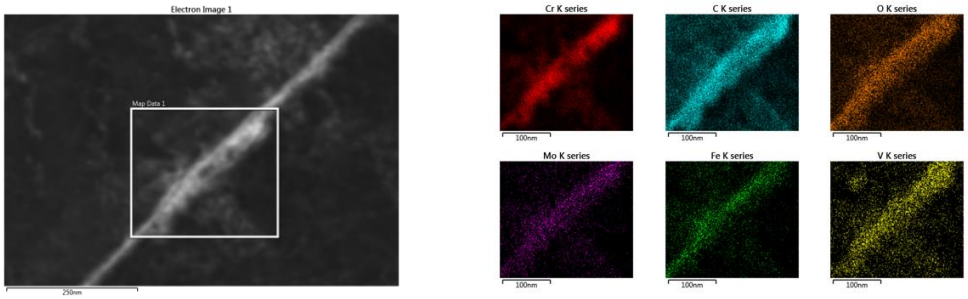

Figure 4-26: EDS mapping of Cr precipitates at the grain boundary

4.4. Stress corrosion testing

4.4.1. Susceptibility stress corrosion cracking

U-bend specimens were employed for qualitative metallography – to determine the SCC mechanism present in FV566 steel immersed in 3.5% NaCl at 90°C. The results of the susceptibility stress corrosion tests are presented below.

4.4.1.3. Strain on the outer surface of the U-bend

The total strain on the outer surface of the U-bend specimens, is measured as a function of the thickness of the specimen, using an equation from section 3.5.2.1. The total strain varied from 2.9% to 3.6% on the outer surface of the U-bend.

4.4.1.4. Time to failure

The times to failure for each heat-treatment variation of the U-bend specimens immersed in 3.5% NaCl at 90°C, were monitored. The results are summarised in Figure 4-27.

The 480°C temper specimen was the most sensitive to SCC, with an average failure time of 129 hours. The 550°C temper sample was similarly highly sensitive to SCC, with an average failure time of 175 hours. The 570°C temper test 2 sample failed after 210 hours; this result did not agree with the result of test 1 and test 3, and was therefore discarded.

The material's resistance to SCC improved with tempering temperature. The 600°C temper sample proved to be the most resistant to SCC. No discernible crack initiation and growth was observed after 4000 hours of testing.

4.4.1.5. Light microscopy of fracture paths on U-bend surfaces

Light optical micrographs were taken as the crack propagated through the surface of the material. The appearance of SCC was with crack propagation direction orientated perpendicular to the applied stress direction – as shown in Figure 2-28.

A single primary crack is observed with significant secondary crack branching on the 480°C, 550°C, and 560°C temper specimens.

Heat treatment (°C)	Time to failure of U-bend Specimens in 3.5% NaCl (Hours)				
	Test 1	Test 2	Test 3	Average	
480	138	120	-	129	
550	162	188	-	175	
560	307	378	-	342.5	
570	667	210	720	693.5	Result from test 2 was discarded due to substantial variation in result from tests 1 and 3; test 2 result was not used further.
580	1506	1600	-	1553	
590	520	427	-	473.5	
600	>4000	>4000	-	-	No discernible crack initiation was observed after 4000 hours of testing.
620	1890	-	-	-	

Table 4-4: Summary of time to failure of U-bend specimens immersed in 3.5% NaCl at 90°C

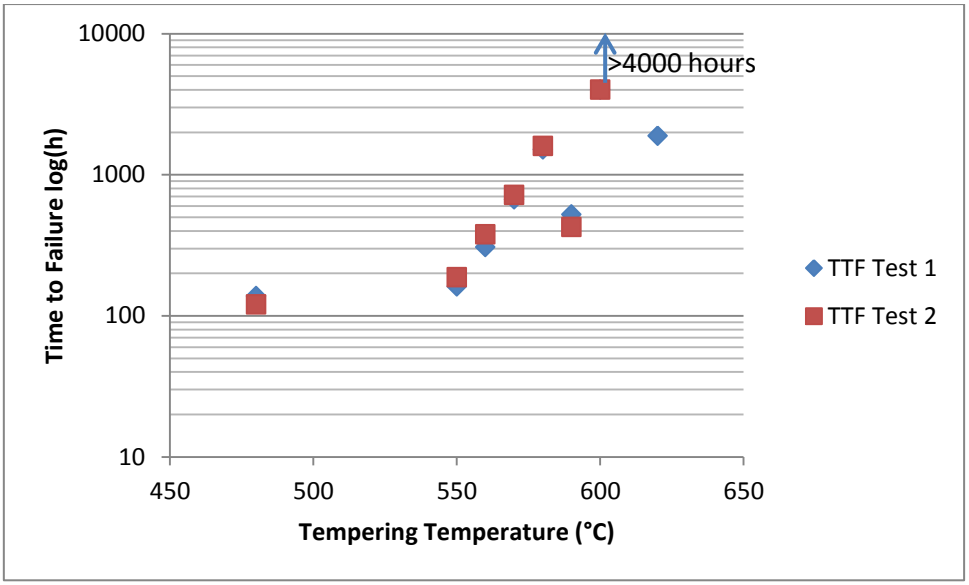

Figure 4-27: Time to failure of U-bend Specimens immersed in 3.5% NaCl at 90°C, indicating the material's resistance to SCC increases with increasing tempering temperature

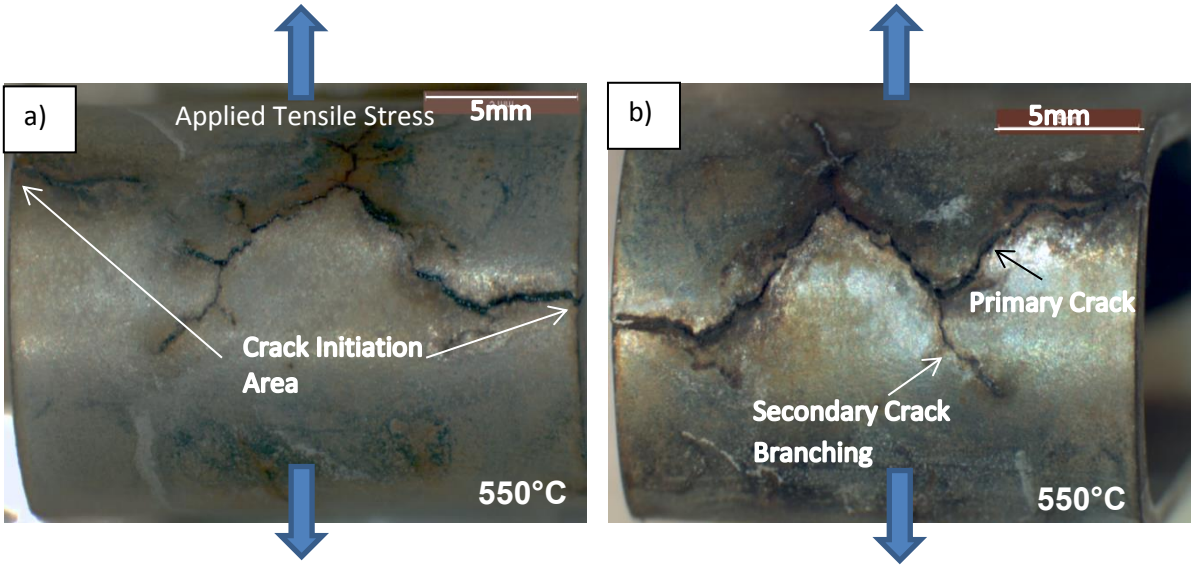

Figure 4-28: Light micrographs of 550°C temper U-bend specimen outer surface, showing: a) crack initiation areas; and b) secondary crack branching and crack propagation. The arrows indicate the direction of the applied tensile stress

Finer, shallower cracks were observed on the surface of the 570°C temper U-bend specimen, with secondary crack branching present. The magnitude of secondary crack branching was reduced, when compared to the 480°C, 550°C and 560°C temper specimens. No secondary crack branching was observed for the 580°C, 590°C and 620°C temper samples. SCC for the 620°C specimen was initiated from a pit, as shown in Figure 4-31. A rust-coloured corrosion layer was observed on the surface of U-bend test specimens.

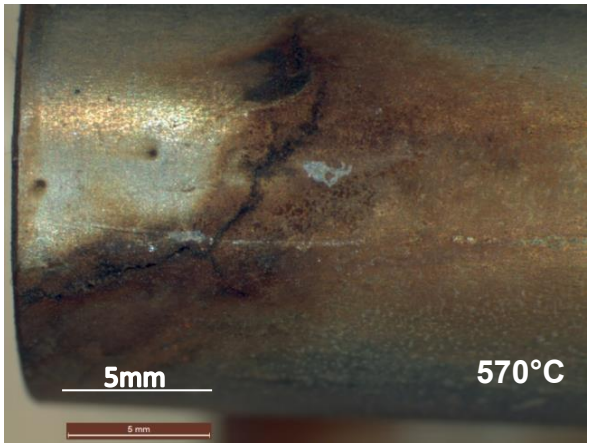

Figure 4-29: 570°C temper U-bend after immersion in 3.5% NaCl. Fine, shallow cracks were observed on the surface of the specimen.

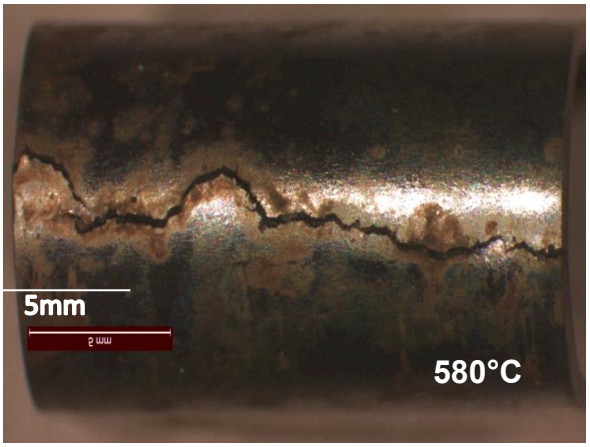

Figure 4-30: 580°C temper U-bend after immersion in 3.5% NaCl. A single primary crack with no secondary branching was observed.

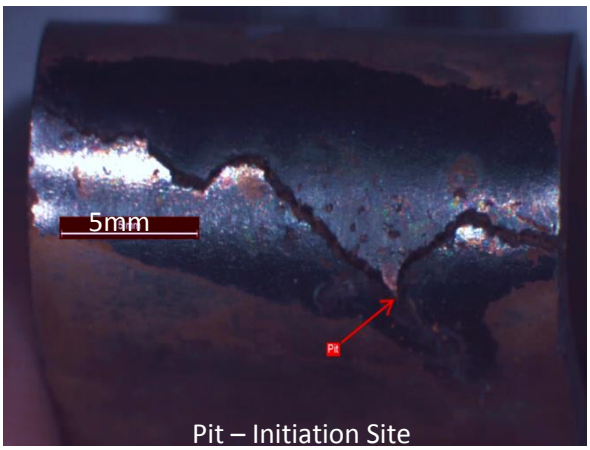

Figure 4-31: 620°C temper U-bend specimen after immersion in 3.5% NaCl, with crack initiation from a pit

The results are summarised in Table 4-5 on page 88:

U-bend Sample Temper (°C)	U-bend Surface and Crack Appearance
480	Single primary with significant crack branching. Rust-like oxide layer observed on the specimen surface.
550	Single primary with significant crack branching. Rust-like oxide layer observed on the specimen surface.
560	Single primary with significant crack branching. Rust-like oxide layer observed on the specimen surface.
570	Finer, shallower primary crack with crack branching. Rust-like oxide layer observed on the specimen surface.
580	Single primary crack with no crack branching. Black oxide layer observed on the specimen surface.
590	Single primary crack with no crack branching. Black and rust oxide layer observed on the specimen surface.
600	No discernible crack growth identified. Rust-like oxide layer observed on the specimen surface.
620	Single primary crack with no crack branching. Black oxide layer observed on the specimen surface.

Table 4-5: U-bend surface and fracture path appearance summary

Light micrographs were taken of the polished fracture surfaces in order to assist in determination of the fracture mechanism. The U-bend samples exhibited crack growth in a direction perpendicular to the applied stress. The samples were obtained from the failed U-bend specimens with the applied stress perpendicular to the position of the specimens. The specimens were taken ahead of crack tips.

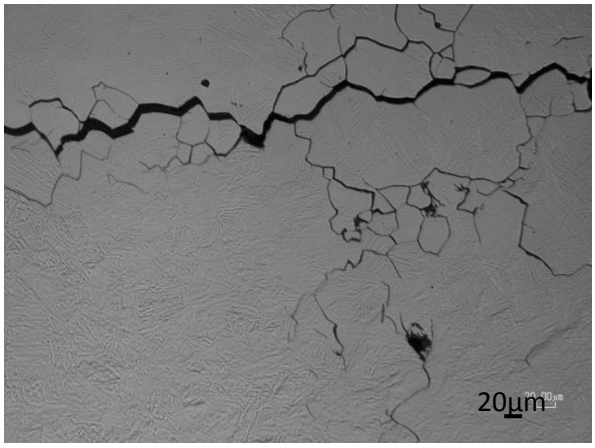

Figure 4-32: Light micrograph image of 480°C, showing secondary cracking and intergranular SCC

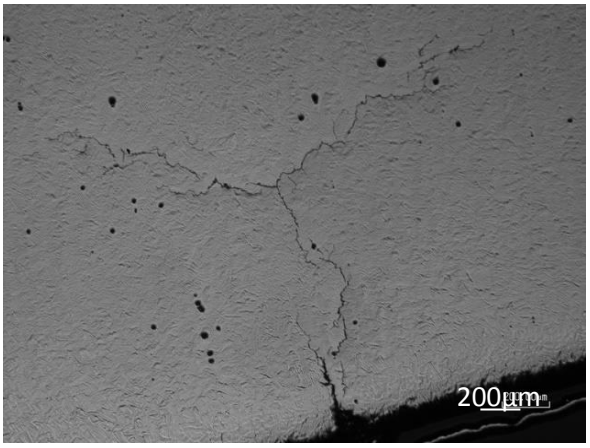

Figure 4-33: Light micrograph of 550°C temper U-bend specimen, showing secondary crack branching

The observations noted from the polished fracture surfaces agreed with those of

Figure 4-28-Figure 4-31 above. A single primary crack was noted in the direction perpendicular to the applied tensile, with secondary crack branching for the 480°C, 550°C and 560°C samples. The dominant fracture mechanism for each temper heat treatment appeared to be intergranular SCC. This was investigated further using SEM imaging and EBSD.

4.4.1.6. SEM Images of polished U-bend fracture surfaces

SEM Images were taken at higher magnifications to characterise the dominant fracture mechanism. The fracture mechanism was identified using SEM imaging as intergranular SCC along prior austenite grain boundaries, for the 480°C, 550°C, 560°C and 570°C temper conditions.

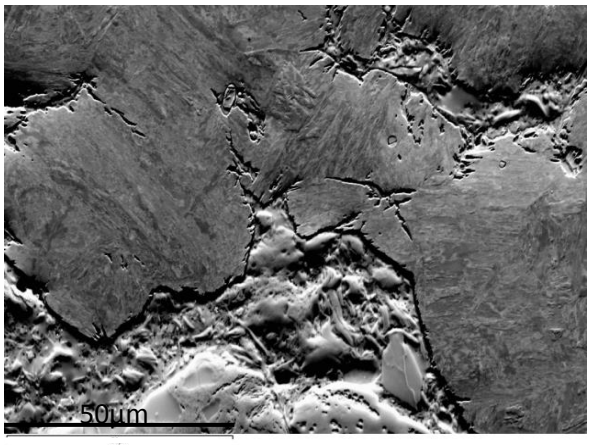

Figure 4-34: SEM image along primary crack path for the 550°C temper specimen

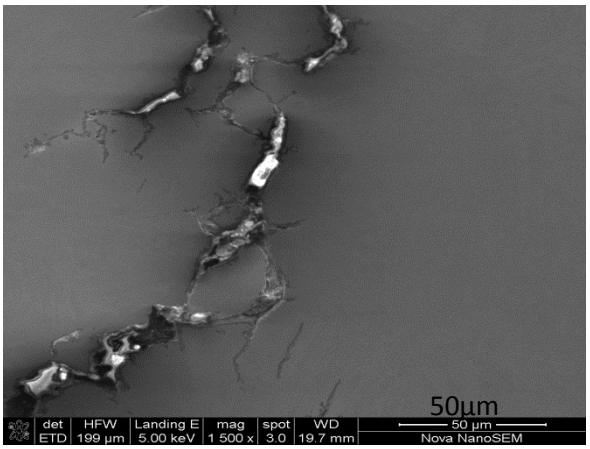

Figure 4-35: 570°C temper U-bend sample, showing secondary crack propagation using BSD image

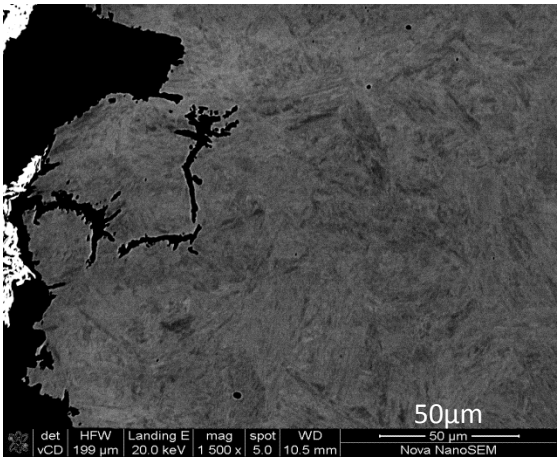

Figure 4-36: SEM Image of 570°C temper U-bend along primary crack path, with intergranular SCC along prior austenite grain boundary

4.4.1.7. Fractography

Fractography analysis was used to characterise the SCC crack growth and fracture morphology. The fractographs indicated that the dominant environmentally assisted fracture mode is intergranular SCC – primarily along prior austenite grain boundaries with secondary cracking along martensite lath boundaries.

Enlargement of the fracture surface area displays the well-defined grain boundary separation – as seen in Figure 4-38 and Figure 4-40.

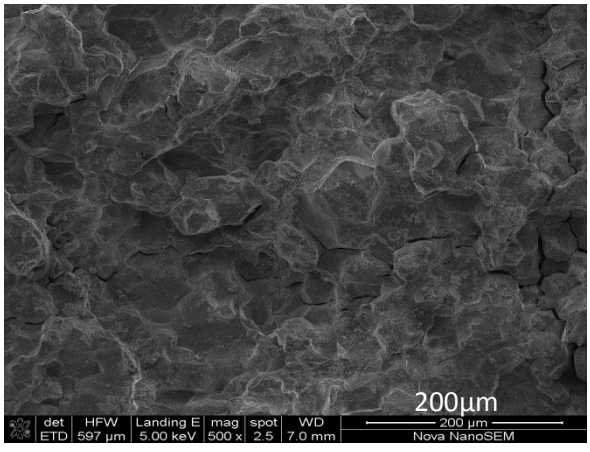

Figure 4-37: Fracture surface of 480°C temper U-bend specimen cracked in 3.5% NaCl, showing intergranular SCC and secondary cracking

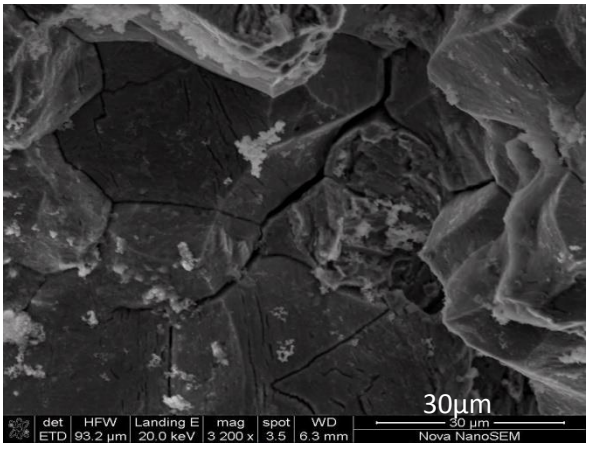

Figure 4-38: Fracture surface of 480°C temper U-bend specimen, showing grain boundary separation

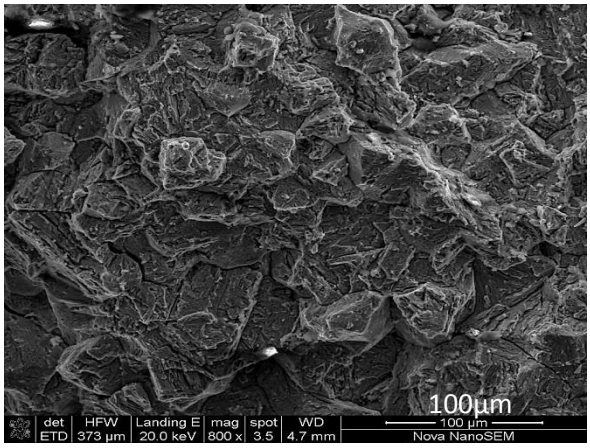

Figure 4-39: Fracture surface of 550°C temper U-bend specimen cracked in 3.5% NaCl, showing intergranular SCC and secondary cracking

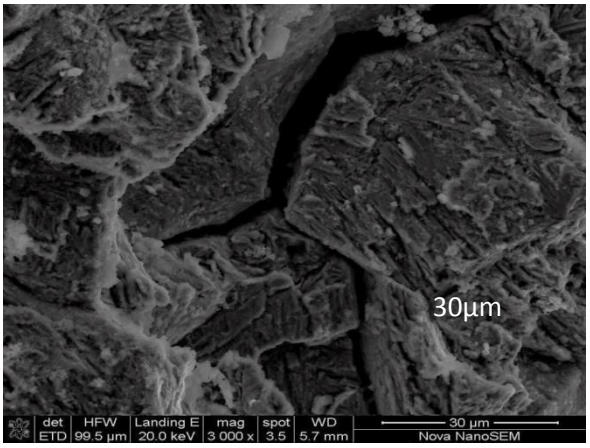

Figure 4-40: Fracture surface of 550°C temper U-bend specimen cracked in 3.5% NaCl, showing clear grain boundary separation

The extended duration of the 580-620°C U-bend tests resulted in a corrosion product layer being formed on the surface of the specimen, which obscured the view of the crack path, as seen in Figure 4-41 and Figure 4-41. These fracture surfaces were ultrasonically cleaned in SurTec 414 neutral activator.

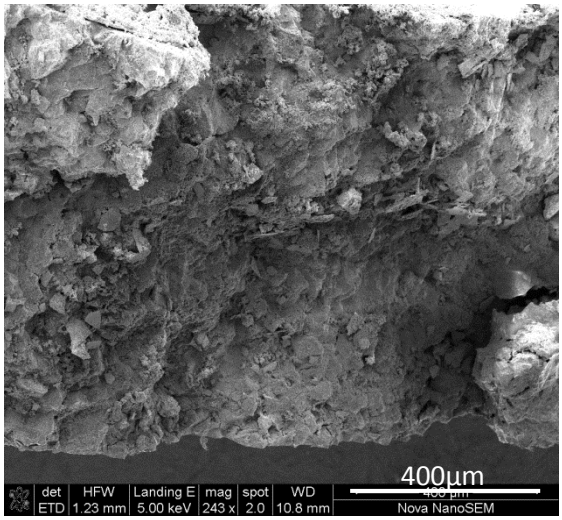

Figure 4-41: Corrosion product layer formation on fracture surface of 620°C U-bend specimen

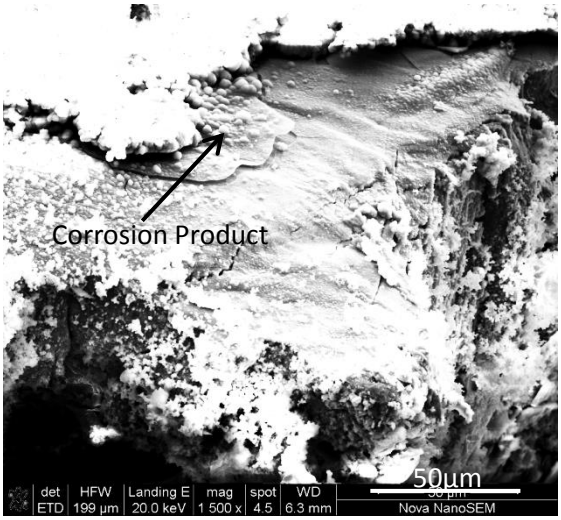

Figure 4-42: Corrosion product layer formation on fracture surface of 620°C U-bend specimen

Post-cracking surface corrosion attack occurred in the 580°C, 590°C and 600°C temper U-bend specimens – due to the prolonged testing times as seen in Figure 4-43 and Figure 4-44.

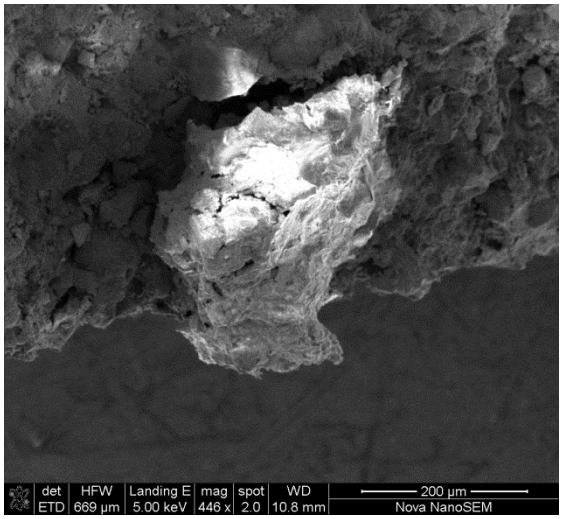

Figure 4-43: Post-cracking corrosion on fracture surface of 620°C temper U-bend specimen

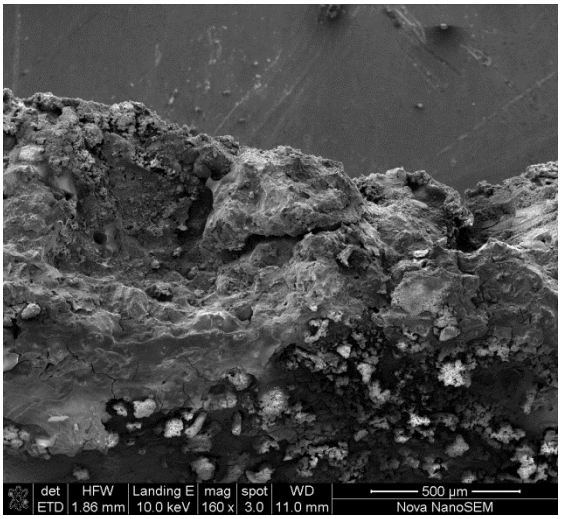

Figure 4-44: Post-cracking corrosion on fracture surface of 570°C temper U-bend specimen

4.4.1.8. Electron back scattered diffraction results

EBSD analysis was utilised to characterise the fracture morphology. EBSD was carried out on polished fracture surfaces of the various U-bend specimens. All angle Euler maps were plotted and analysed using *HKL Channel 5 Software.* [75] Misorientation angles were calculated across grain boundaries.

Figure 4-45 to Figure 4-53 on pages 93-95 show all angle Euler maps obtained for the 480°C, 550°C, 560°C, 570°C, 590°C and 620°C temper samples. Areas along crack paths from the U-bend surface were scanned. An indexing rate of 90% and higher with acceptable quality Kikuchi patterns was obtained during acquisition of the EBSD data.

FV566 stainless steel has a tempered martensite microstructure with a BCC crystal structure. Martensite lath boundaries were visible from the Euler colour maps; the SCC crack paths were clearly identified in all Euler maps. The crack paths are observed as un-indexed points which are indicated as black regions.

Crack paths were analysed by measuring the misorientation angle across the grain boundary. The misorientation angle distribution for the scanned area was plotted and evaluated. Low-angle grain boundaries which represent subgrains are typically calculated to be 2° to 15° misorientation. High-angle grain boundaries are all boundaries with an angle exceeding 15°. These boundaries can be distinguished between martensite lath- (and block-) boundaries (45°-63°), and prior austenite grain boundaries (up to 63°). Hence, every boundary with a misorientation angle of 15°-45 is representative of prior austenite grain boundaries in martensitic steels.

Analysis of misorientation angles along crack paths revealed predominantly angles of 20° to 40°, which represent prior austenite grain boundaries. Cracking was also found along martensite lath boundaries – as seen in Figure 4-48 on page 93.

The SCC cracking morphology was evaluated as primarily intergranular SCC – with cracking along martensite lath boundaries.

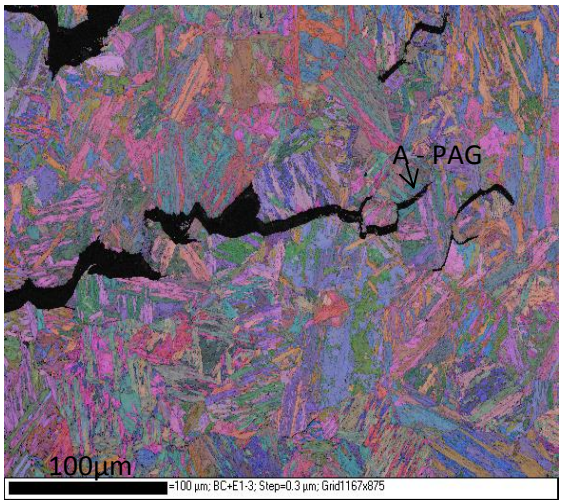

Figure 4-45: All Euler colour map of 480°C temper U-bend specimen, indicating intergranular SCC. Crack paths are indicated by non-indexed points which appear black in colour

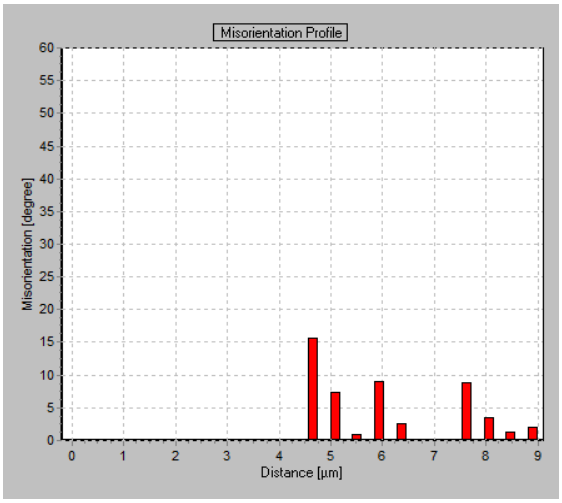

Figure 4-46: Misorientation profile across 480°C temper crack path at point A, indicating a prior austenite grain

Figure 4-47: All Euler colour map of 550°C temper U-bend specimen, indicating intergranular SCC; crack paths are indicated by non-indexed points

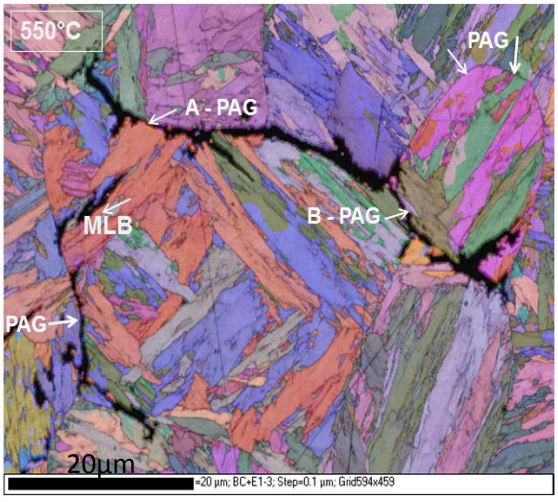

Figure 4-48: All Euler colour map of 550°C temper specimen (zoomed in), showing martensite lath boundaries and prior austenite grains

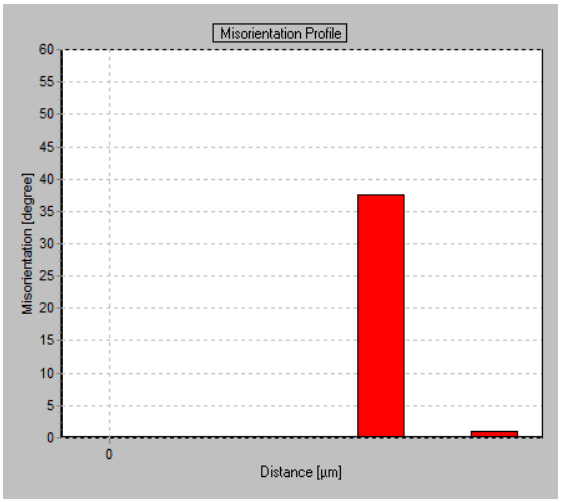

Figure 4-49: Misorientation across 550°C temper crack path at point A, indicating a prior austenite grain

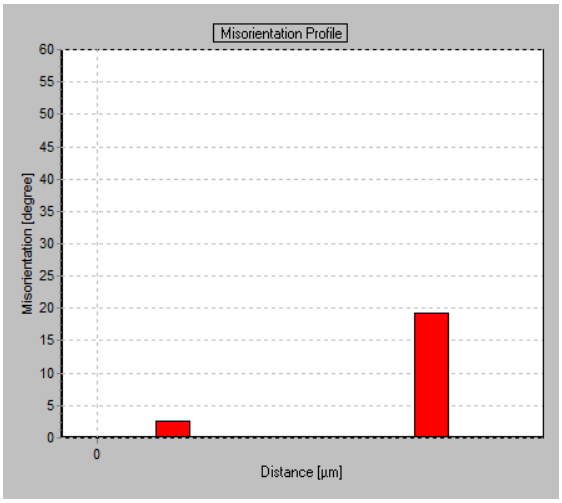

Figure 4-50: Misorientation profile across 550°C temper crack path at point B, indicating a prior austenite grain

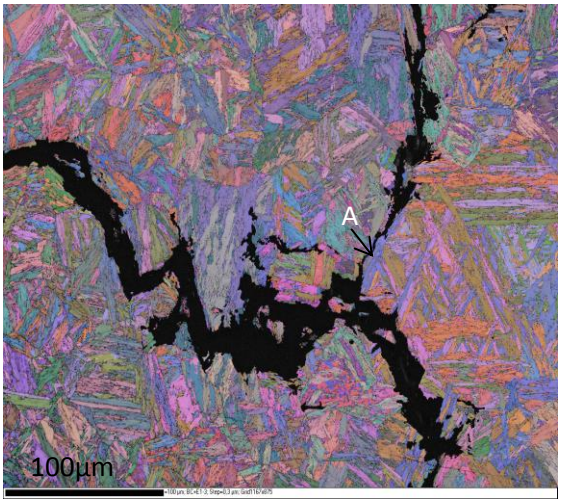

Figure 4-51: All Euler colour map of 570°C U-bend sample; the crack path is indicated by the non-indexed portion of the scan; prior austenite grain is indicated at point A

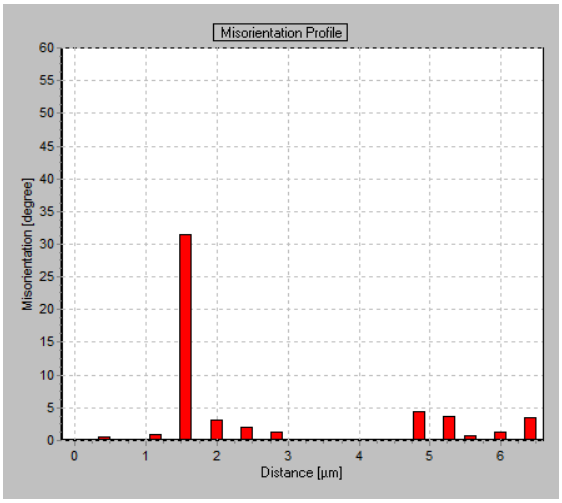

Figure 4-52: Misorientation profile of 570°C U-bend specimen at point A in Figure 4-51

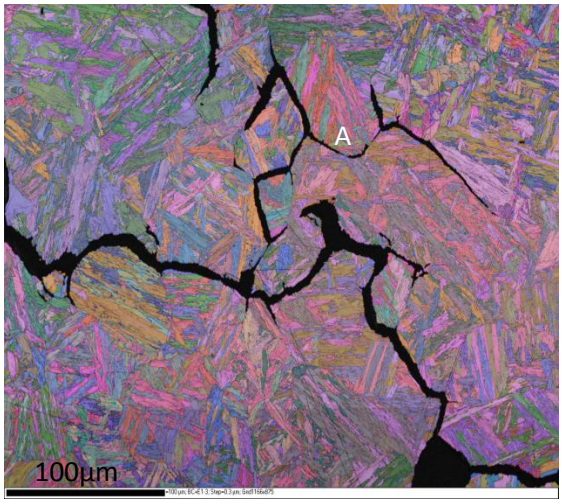

Figure 4-53: All Euler map of 590°C U-bend sample; crack path is indicated by un-indexed points denoted in black

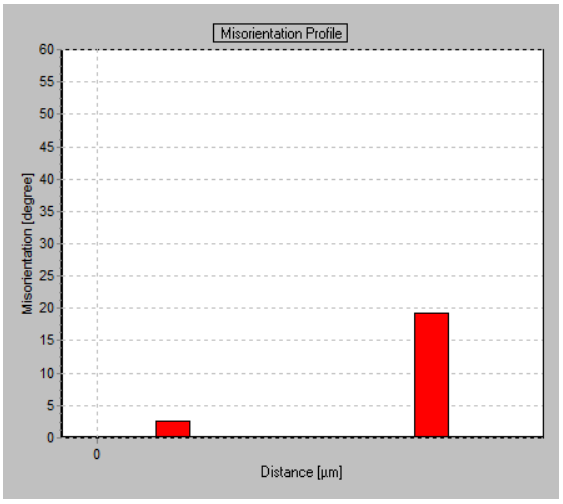

Figure 4-54: Misorientation profile across crack path for 590°C temper U-bend at point A, indicating a prior austenite grain

Figure 4-55: All Euler Map of 600°C U-bend Sample; crack path is indicated by unindexed points denoted in white

4.4.1.9. TEM Analysis of U-bend fracture path

TEM analysis was carried out on the tested 590°C U-bend sample. The crack path was determined to be primarily across the prior austenite grain boundaries – as shown in Figure 4-54 above. A TEM sample was taken cross-sectionally across the grain boundary, just ahead of the crack tip shown in Figure 4-56 below.

The specimen was then analysed using HAADF-STEM, with STEM_EELS spectrum imaging to map the elemental distribution surrounding the grain boundaries.

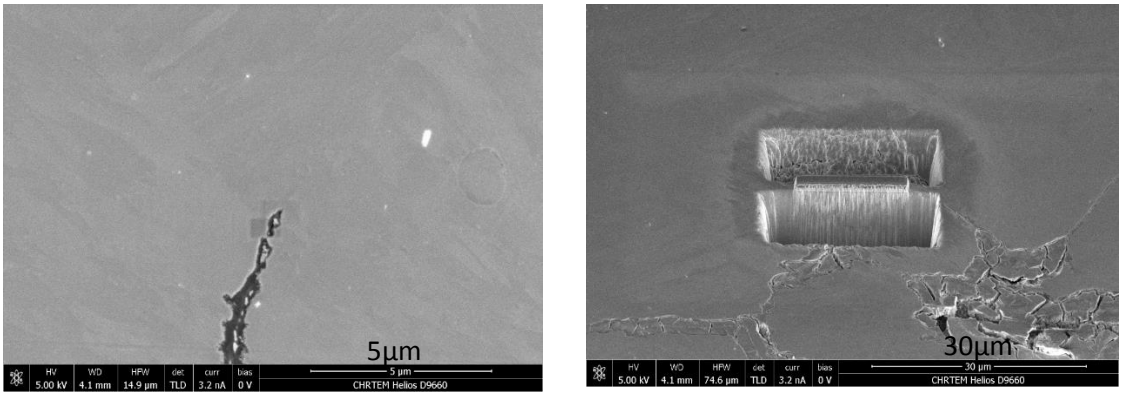

Figure 4-56: Secondary electron images of the crack-tip for the 590°C U-bend, and location of the TEM sample

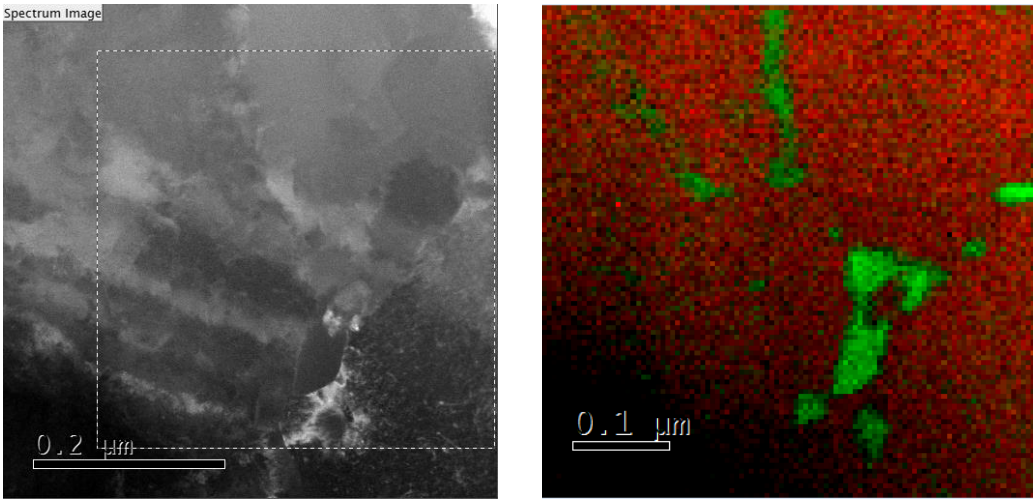

Figure 4-57: HAADF-STEM image of the prior austenite grain boundary and STEM-EELS elemental (Fe:red and Cr:green), showing chromium-rich precipitates along the grain boundaries (sub-grain + prior-austenite).

4.4.2. Stress intensity relationship results

The stress intensity and crack growth for different heat treatments of FV566, was determined using precracked wedge open loading samples (WOL) – as described in section 3.5.3. The WOL specimen is a crack arrest specimen in which the crack opening displacement (COD) is held constant at the load line. As the crack propagates, the load and stress intensity decreases until the threshold stress intensity K_{1SCC} is achieved. The results of the WOL tests are summarised below.

Samples were fatigue precracked using a K-stepping method, as described in the section 3.5.3, and then loaded to a predetermined starting stress intensity. The starting stress intensity K_{10} varied for each temper heat treatment. This value was determined using both the tensile strength of the material, and experimentally (refer to section 3.5.3 and to Appendix C for V_0 values). The loaded specimens were immersed in 3.5% NaCl at a temperature of 90°C.

Crack length rates were measured optically using a light microscope. The crack length represents the average of measurements on the two surface faces. Two or more tests for each temper treatment were carried out to ensure repeatability. The specimens from test 1 and 2 are referred to tempering temperature (1) and tempering temperature (2) respectively. (i.e. 480(1) and 480(2)).

4.4.2.1. Stress intensity (K), crack length and test time

Crack length is plotted as a function of the test time. The crack-tip stress intensity was calculated using compliance equations (equation 3.13, as a direct measurement of the load was impossible during the test. The results are summarised in Table 4-6.

480°C temper specimens

The starting stress intensity (K_{10}) for test 1 of the 480°C temper WOL specimen was 62.0 MPa√m. Crack growth was preceded by an incubation period of 46 hours for test 1. During the incubation period, the starting stress intensity is applied and the specimen is placed in the test solution. This is the period preceding crack growth rate. The incubation period is followed by rapid crack growth – and thereafter a decrease in crack growth as the stress intensity decreases. Crack growth rates for the 480°C temper specimens were 10 times greater than the 550°C temper sample.

The starting stress intensity for test 2 was 31.3 MPa√m. Significant crack branching and crack tunnelling was noted for this sample – as seen in Figure C-2 Appendix C. Meaningful data could not be obtained from this test, and hence only one result is reported for the 480°C temper WOL specimen.

Figure 4-58 on page 99 shows the relationship between the crack length and test time.

550°C temper specimens

The starting stress intensity (K_{10}) for tests 1, 2, and 3 of the 550°C temper WOL specimen was 50.2 MPa√m, 35.0MPa√m and 50.9 MPa√m. Crack growth was preceded by an incubation period of approximately 288, 320 and 250 hours – for tests 1, 2 and 3 respectively.

For tests 1 and 3, the incubation period is followed by rapid crack growth and thereafter a decrease in crack growth, as represented in Figure 4-59. The results of these two tests showed good correlation.

Significant crack branching and crack tunnelling was noted for specimen 2 – as seen in Figure C-3 Appendix C. These results were discarded and were not utilised further in the data analysis. Meaningful data could not be obtained from this test, and thus a third test was carried out.

560°C temper specimens

The starting stress intensity (K_{10}) for tests 1, 2, and 3 of the 560°C temper WOL specimen was 67.4, 114.2 and 68.0 MPa√m, respectively. Crack growth was preceded by incubation time of approximately 210, 48 and 196 hours for tests 1, 2, and 3, respectively.

For tests 1 and 3, the incubation period is followed by rapid crack growth and thereafter a decrease in crack growth – as represented in Figure 4-59. A maximum crack growth of 0,05mm/hr at a stress intensity of 53,2MPa.√m was noted for the 560(1) specimen as shown in Table 4-6.

Significant crack branching and crack tunnelling was noted for specimen 2 – as seen in Figure C-4 in Appendix C. Meaningful data could not be obtained from this test, and hence a third test was carried out.

570°C temper specimens

The starting stress intensity (K_{10}) for tests 1 and 2 were 80 MPa.√m and 76 MPa.√m respectively. Crack growth rate was preceded by an incubation period of 334 and 168 hours respectively.

The incubation period is followed by rapid crack growth, and thereafter a decrease in crack growth. A maximum crack growth rate of 0.02 and 0.031 mm/hr at a stress intensity of 55.5 and 63 MPa√m, for tests 1 and 2 respectively, was recorded as shown in Table 4-6.

580°C temper specimens

The starting stress intensity (K_{10}) for tests 1 and 2 was 81 MPa.√m and 82 MPa.√m respectively. Crack growth rate was preceded by an incubation period of 576 and 453 hours respectively.

A maximum crack growth rate of 0.038 and 0.023 mm/hr at a stress intensity of 64.1 and 65.9 MPa√m for tests 1 and 2 respectively, was obtained.

590°C temper specimens

The starting stress intensity (K_{10}) for test 1 was 47 MPa.√m. After an incubation period of 2300 hours, no discernible crack growth was observed. The starting stress intensity for tests 2 and 3 was 81 and 86 MPa.√m respectively. After 1300 hours, no discernible crack growth was observed for test 3.

600°C temper specimens

The starting stress intensity (K_{10}) for tests 1 and 2 was 102 MPa.√m. After an incubation period of 1500 hours, no discernible crack growth rate was recorded at this stress intensity.

620°C temper specimens

The starting stress intensity (K_{10}) for tests 1 and 2 was 105 and 98 MPa.√m respectively. Crack growth rate was preceded by an incubation period of 650 and 400 hours respectively. A maximum crack growth rate of 0,013mm/hr was recorded at a stress intensity of 80 MPa√m shown in Table 4-6.

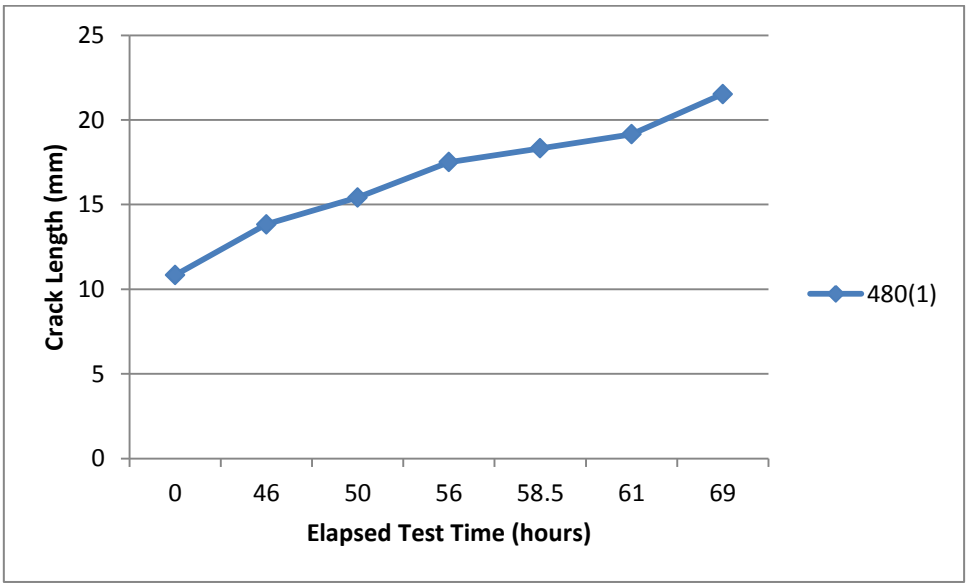

Figure 4-58: Crack length versus test time for the 480°C temper WOL specimen

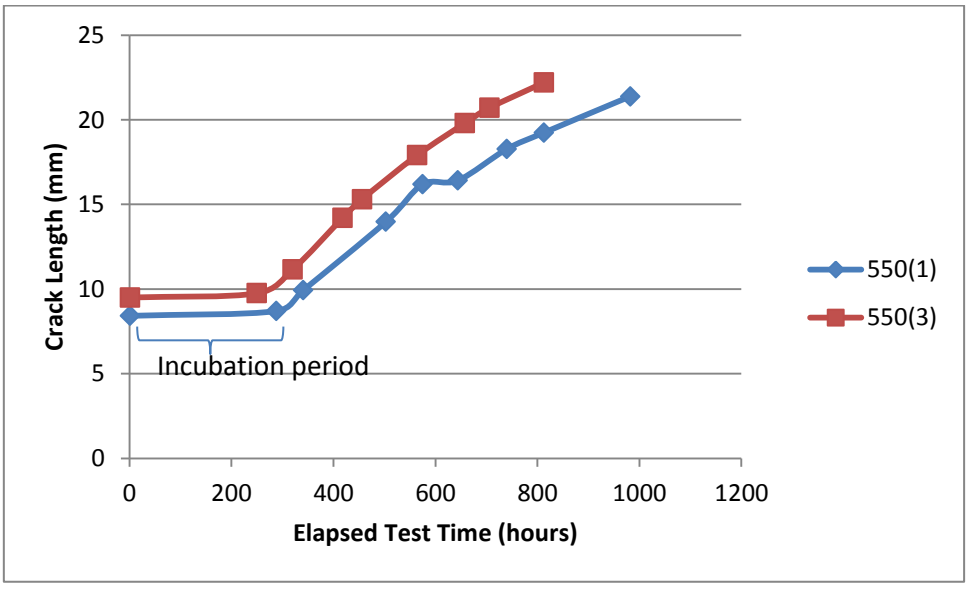

Figure 4-59: Crack length versus test time for the 550°C temper WOL specimens

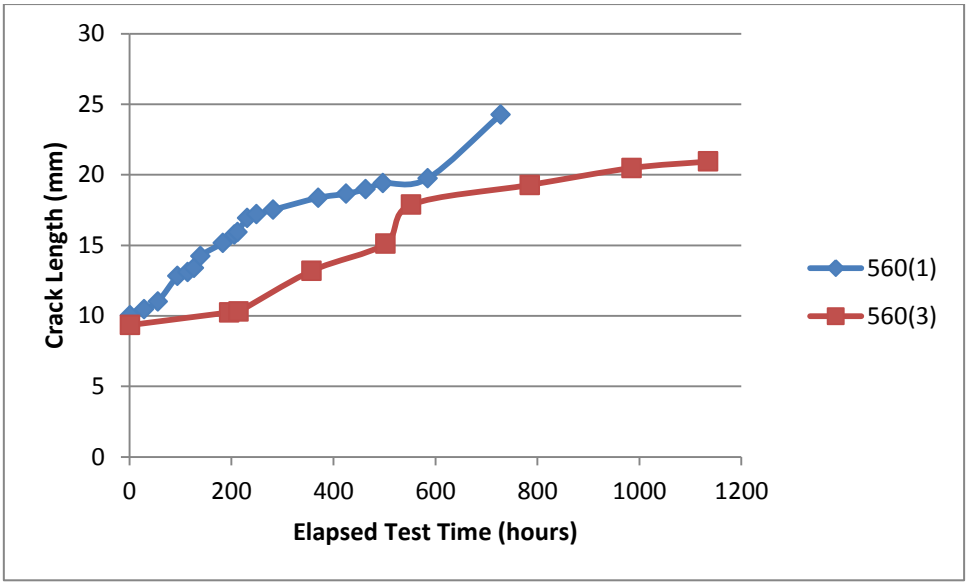

Figure 4-60 Crack length versus test time for the 560°C temper WOL specimens

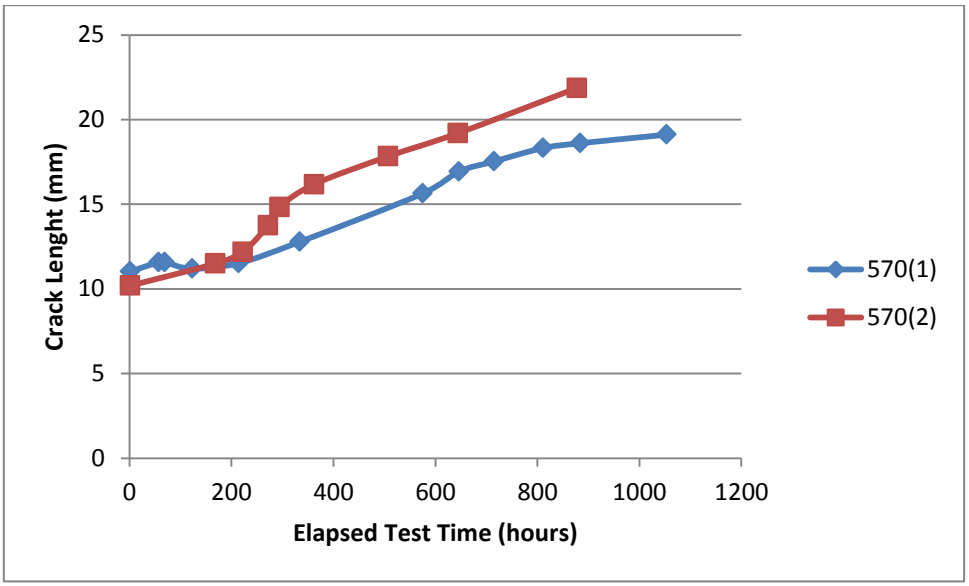

Figure 4-61: Crack length versus test time for the for 570°C temper WOL specimens

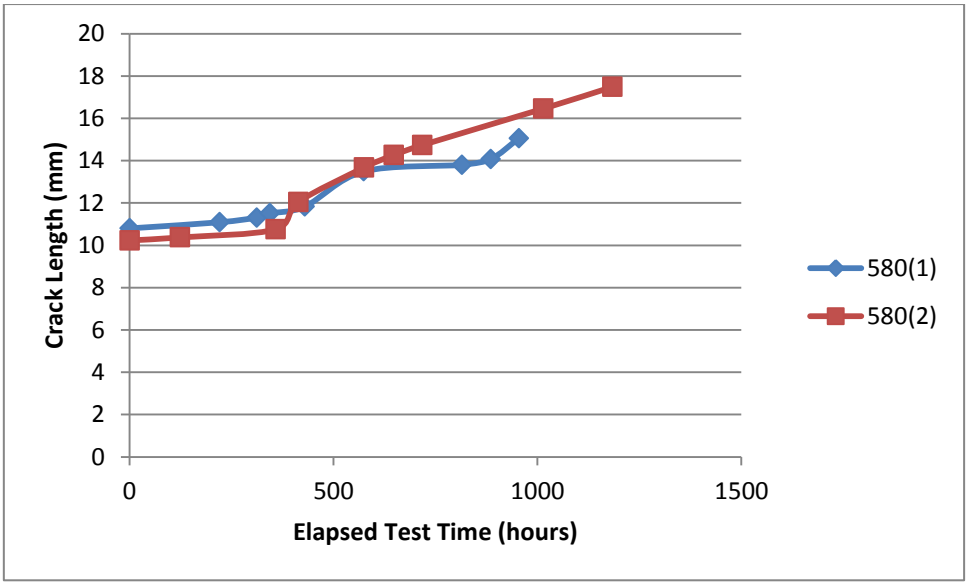

Figure 4-62: Crack length versus test time for the 580°C temper WOL specimen

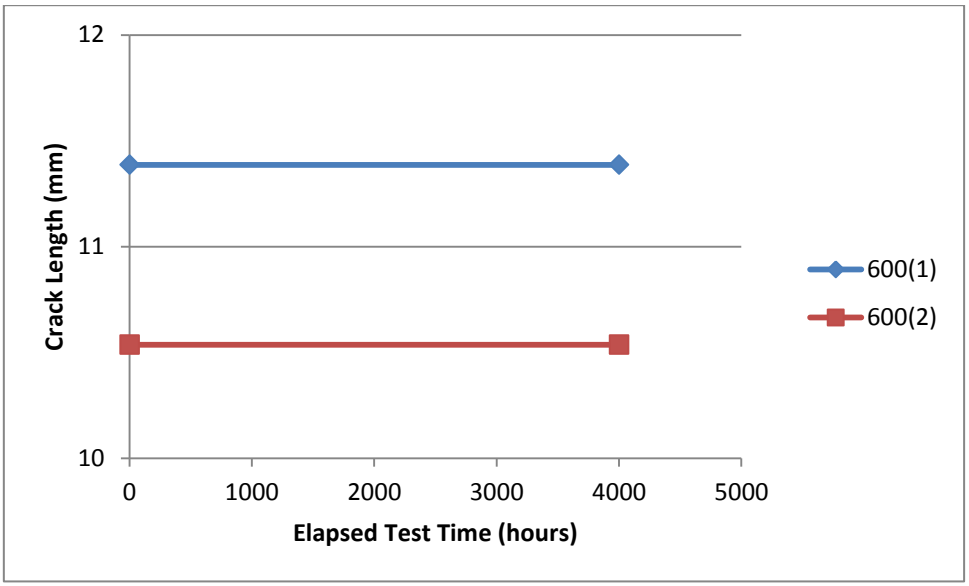

Figure 4-63: Crack length versus test time for the 600°C temper WOL specimen

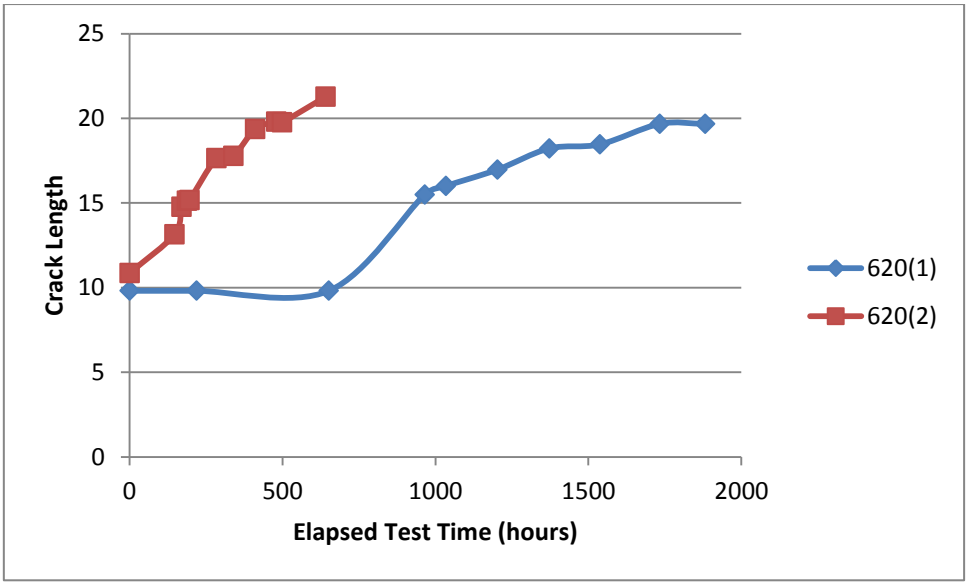

Figure 4-64: Crack length versus test time for the 620°C temper WOL specimens

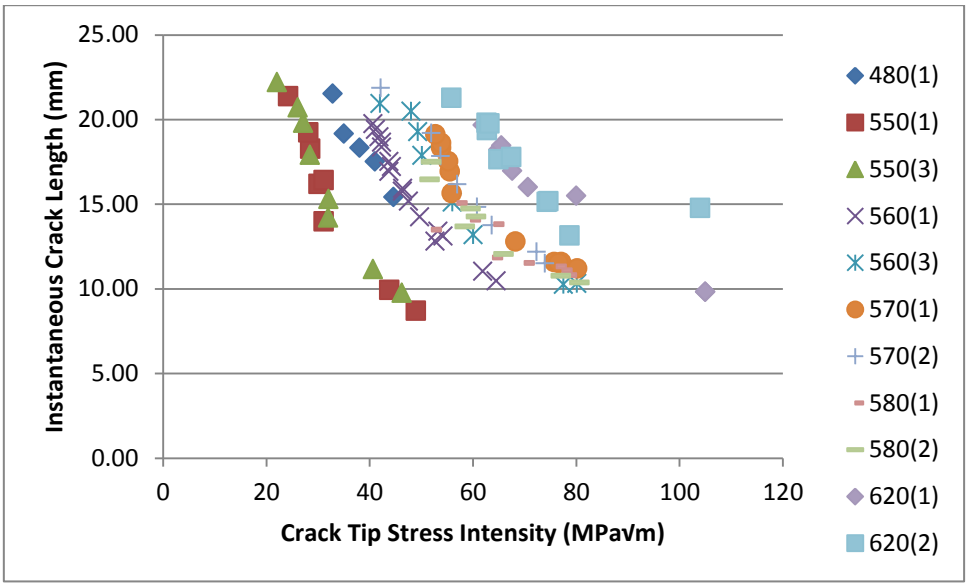

Figure 4-65: Instantaneous crack length versus crack tip stress intensity for the different temper specimens

Tempering Temperature (°C)	Starting Stress Intensity K_{10} ($\frac{MPa}{\sqrt{m}}$)	Instantaneous crack length a (mm)	Elapsed Time (hours)	Crack growth (mm)	Stress Intensity - K ($\frac{MPa}{\sqrt{m}}$)	Crack growth rate (mm/hr)
480(1)	62	13.83	46	2.997	46.2	0.065
		15.4155	50	1.583	44.6	0.4
		17.5045	56	2.089	41	0.34
		18.32	58.5	0.81	38	0.32
		19.15	61	0.83	35	0.31
		21.527	69	2.377	32.8	0.3
550(1)	50.2	8.7005	288	0.283	48.9	0.00098
		9.9355	341	1.235	43.8	0.023
		13.973	503	4.0375	31.1	0.025
		16.181	575	2.208	30.1	0.031
		16.412	644	0.231	31.1	0.02
		18.269	740	1.857	28.5	0.019
		19.2405	813	0.9715	28.1	0.013
		21.3785	982	2.138	24.2	0.013
550(3)	50.9	9.75	250	0.35	46.2	0.001
		11.15	320	1.4	40.6	0.020
		14.2	418	3.05	31.9	0.031
		15.3	456	1.1	32.0	0.029
		17.9	564	2.6	28.4	0.024
		19.8	658	1.9	27.1	0.020
		20.7	706	0.9	26.1	0.019
		22.2	813	1.5	22.0	0.014
560(1)	67.4	10.453	29	0.433	64.5	0.015
		11.0165	56	0.5635	61.9	0.02
		12.811	94	1.7945	52.7	0.046
		13.0975	114	0.2865	54.2	0.0137
		13.3805	127	0.283	53.2	0.05
		14.237	139	0.8565	49.7	0.067
		15.1575	183	0.9205	47.5	0.0209
		15.7565	206	0.599	46.3	0.0255
		15.92	212	0.1635	46.4	0.0251
		16.9265	231	1.007	43.7	0.0507
		17.2	249	0.2735	44.2	0.015
		17.521	282	0.321	43.7	0.0095

		18.3655	370	0.8445	42.3	0.0096
		18.649	425	0.2835	42.3	0.0051
		18.9765	463	0.3275	41.8	0.0086
		19.401	497	0.4245	41.1	0.0123
		19.739	585	0.338	40.6	0.0038
560(3)	68				84	0
		10.244	196	0.901	77.5	0.0045
		10.3	214	0.056	80.1	0.0297
		13.185	357	2.885	60	0.0202
		15.114	502	1.929	56	0.0133
		17.872	552	2.758	50.1	0.0541
		19.2775	785	1.4055	49.3	0.0060
		20.477	985	1.2	48	0.006
		20.937	1135	0.45	42	0.003
570(1)	80	11.5755	57	0.557	75.7	0.0096
		11.5785	69	0.003	77.1	0.0003
		11.1945	123	-0.384	80.2	0.0071
		11.5195	214	0.501	76.6	0.0055
		12.781	334	1.2615	68.2	0.0105
		15.6335	575	2.8525	55.9	0.0118
		16.9335	646	1.3	55.5	0.0181
		17.529	715	0.5955	55.2	0.0086
		18.3195	811	0.7905	53.8	0.0082
		18.604	884	0.2845	53.8	0.0039
		19.11	1053	0.507	52.7	0.0031
570(2)	76	11.494	168	1.31	73.9	0.0078
		12.179	222	0.685	72.3	0.0127
		13.754	272	1.575	63.6	0.0314
		14.8265	294	1.0725	60.8	0.0478
		16.1775	362	1.351	56.9	0.0200
		17.824	507	1.6465	53.7	0.0113
		19.1965	644	1.3725	51.9	0.0100
		21.8615	877	2.665	42.1	0.0114
580(1)	81	10.7995	1	0.2885	78.2	0.001
		11.088	221	0.2195	77.3	0.002
		11.3075	312	0.204	76.2	0.0061
		11.5115	344	0.319	70	0.003
		11.8305	430	1.6585	63.9	0.011

		13.489	574	1.974	52	0.008
		13.8045	815	0.2715	64.1	0.038
		14.076	886	0.9845	59.6	0.014
		15.0605	955	1.016	57	0.0106
580(2)	82	10.3715	123	0.1415	80.6	0.001
		10.756	358	0.3845	77	0.001
		12.0465	413	1.2905	65.9	0.0234
		13.6735	575	1.627	58.4	0.0101
		14.2675	648	0.594	60.6	0.0081
		14.7345	717	0.467	59.5	0.0068
		16.4575	1014	1.723	51.6	0.0058
		17.485	1183	1.0275	51.9	0.0061
620(1)	105	9.811	220	2.811	105	0
		9.811	652	4.1845	105	0.0032
		15.492	965	8.492	80	0.01372
		16	1034	9	70.6	0.00735
		16.9715	1203	9.9715	67.6	0.00572
		18.2195	1372	11.2195	64.9	0.00737
		18.464	1538	11.464	65.5	0.00147
		19.6705	1733	12.6705	61.9	0.00617
		19.6715	1882	12.6715	62.9	6.71E-06
620(2)	98	13.1375	147	2.2735	78.7	0.01
		14.7685	170	1.631	104	0.068
		15.133	188	0.3645	74.3	0.012
		15.175	196.5	0.042	74.6	0.005
		17.6405	284.5	2.4655	64.9	0.0028
		17.78	339.5	0.1395	67.4	0.0025
		19.3675	411.5	1.5875	62.7	0.0022
		19.805	480.5	0.4375	62.6	0.0063
		19.7605	498.5	-0.0445	63.2	0.0024
		21.273	641.5	1.5125	55.8	0.0011

Table 4-6: Summary of relationship between stress intensity and crack growth rate for the various heat treatments

4.4.2.2. Threshold stress intensity determination

Threshold stress intensity (K_{1SCC}) is the minimum stress intensity for which SCC initiation can occur. K_{1SCC} is determined using WOL samples. For a valid K_{1SCC} measurement (final crack length: width) the ratio a/w must be less than 0.8 to satisfy the compliance equation conditions.

The threshold stress intensity (K_{1SCC}) was determined for the 620°C temper WOL samples. K_{1SCC} was determined using the crack length from the fracture surfaces as 23MPa.√m and 28MPa.√m for tests 1 and 2 respectively.

The threshold stress intensity was not determined for the remaining temper specimens.

For majority of the SCC tests, the crack extended through the specimen as seen in Appendix C. The test was stopped when the crack length reached an a/w ratio of 0.8, beyond which K_{1scc} measurements are not valid, as described in section 3.5.23.5.3. Hence, K_{1SCC} was not determined for these specimens. Tests were repeated at a lower stress intensity, which resulted in significant crack branching and crack tunnelling – and the threshold stress intensity was undetermined.

4.4.2.3. Fractography results for WOL specimens

Fracture surface images of the WOL specimens are shown in Figure 4-66 and Figure 4-72. The SCC fractures for the different temper treatments all followed an intergranular path. The intergranular cracking along prior austenite grains, can be distinctly seen in Figure 4-70 and Figure 4-70. Secondary cracking was noted for all specimens. A corrosion product layer was formed on the fracture surfaces – as seen in Figure 4-66 and Figure 4-70. The specimens were cleaned in SurTec 414 neutral activator with partial success. Due to the extended duration of the SCC tests, post-cracking corrosion was also observed on the fracture surfaces.

The transition from fatigue testing to SCC testing can be distinctly seen in Figure 4-66. The transition from the SCC surface to the fast fracture surface, can be seen in Figure 4-71. The absence of the corrosion attack on the fatigue precracked surface, can be clearly seen.

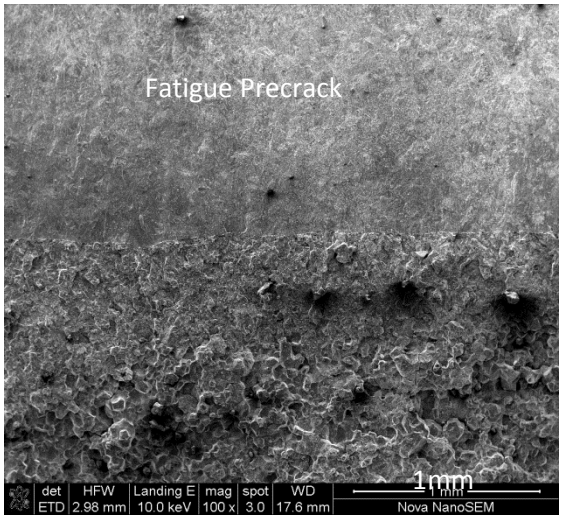

Figure 4-66: Fracture surface of 480°C temper WOL specimen, showing the difference between the fatigue precrack and SCC surface

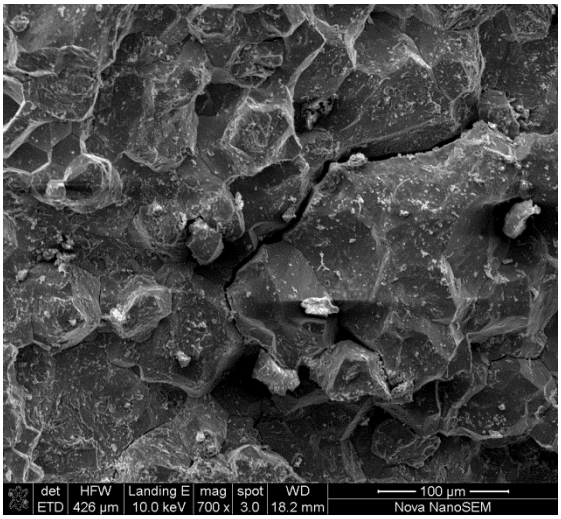

Figure 4-67: Fracture surface of 480°C temper WOL specimen at higher magnification, showing grain separation

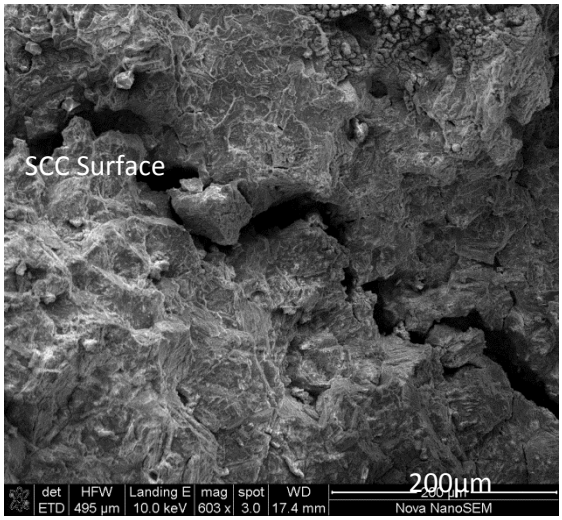

Figure 4-68: Fracture surface of 560°C temper WOL specimen, showing crack path across the sample displaying intergranular SCC and corrosion product formed on surface of the fracture path

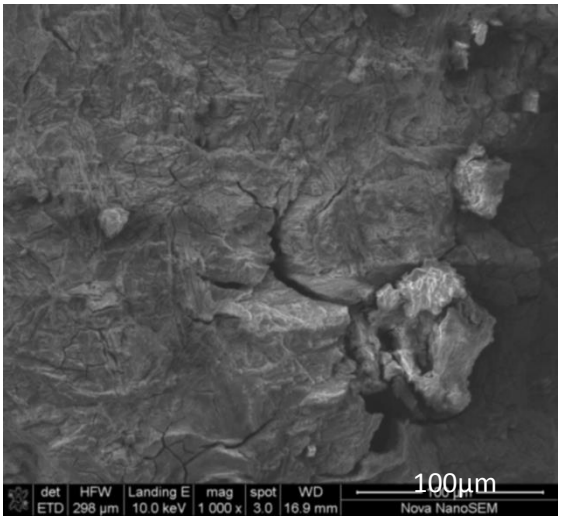

Figure 4-69: Fracture surface of 570°C temper WOL specimen, showing the intergranular fracture

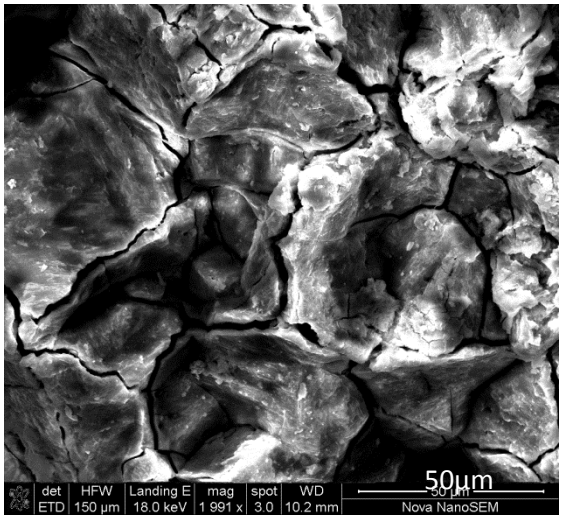

Figure 4-70: Fracture surface of 580°C temper WOL specimen, showing grain boundary separation

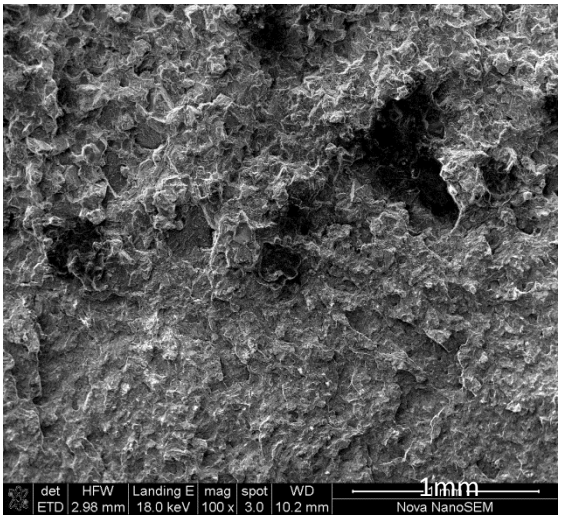

Figure 4-71: Fracture surface of 580°C temper specimen, showing difference between the fast fracture surface and the SCC surface; the absence of corrosion attack on the fast fracture surf ace can be noted

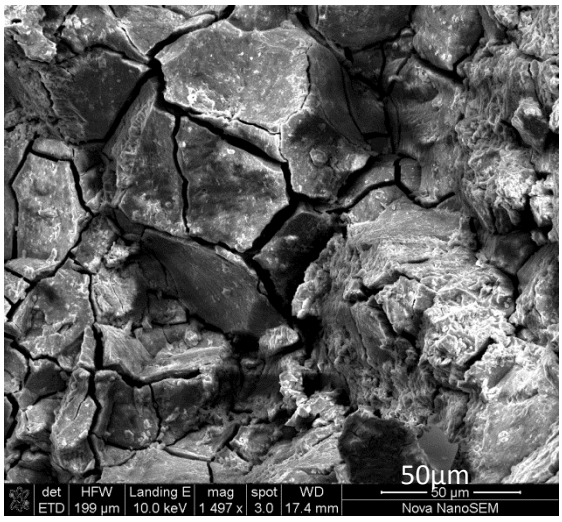

Figure 4-72: Fracture surface of 620°C WOL specimen, showing intergranular SCC with clear grain boundary separation and post-cracking corrosion

5. Discussion

The effect of tempering on the stress corrosion cracking behaviour of 12% Cr steels FV566 used to manufacture LP turbine blades, has been investigated. The hypothesised effect of tempering on the SCC and mechanical properties of 12% Cr steels by previous researchers, is presented below in Figure 5-1. [11] The findings of this research are evaluated and compared to the work of previous researchers.

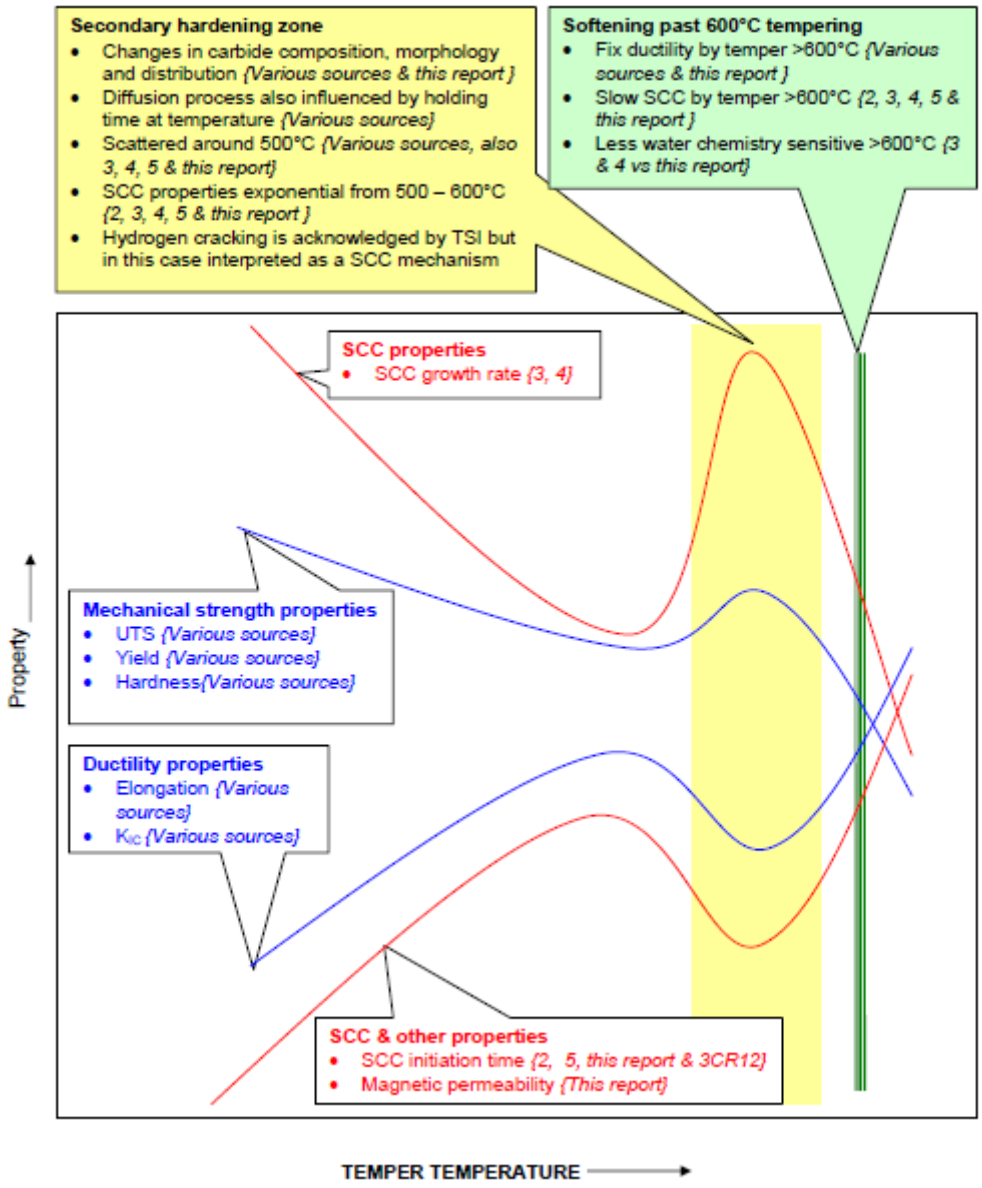

Figure 5-1: Postulated effect of tempering temperature on the SCC and mechanical behaviour of 12% Cr steels [11]

5.1. Material microstructure

The material microstructure was identified as tempered martensite. Analysis of the microstructure with the light microscope and SEM imaging did not show any carbide or chromium precipitates. EDS analysis was carried out on the as received (no applied heat treatment) material. A selection of inclusions were analysed and the results shown in Figure 4-6 and Figure 4-7. The inclusions were identified as most likely to be aluminium oxide and manganese sulphide. This is in agreement with the work of Perkins and Bache [76]. The distribution of the inclusion showed no directionality. Perkins and Bache [76] found the fatigue crack initiation to occur from oxide inclusions at the surface of the material for FV566. Gulbrandsen [77] found the pit initiation sites were MnS stringers and the pits grew along the pathway of the MnS stringers. Pitting and crack initiation mechanisms were not investigated in this study and should be considered for future work.

5.2. Metallurgical influences of tempering

Transmission electron microscopy was carried out on heat-treated samples to analyse the effect of tempering on the formation and location of precipitates – as described in section 3.4.5 4. Four main types of precipitates were identified. The influence of these precipitates on the SCC behaviour of FV566, is discussed below.

A change in tempering temperature resulted in a change in the quantity and type of precipitate formed, with consequent changes in the SCC properties of FV566.

No chromium-rich precipitates were observed in the matrix of the 480°C temper specimen – with isolated areas of chromium-rich precipitates observed for the 550°C temper specimen. Four main types of precipitates were observed for the 560°C, 570°C, 580°C, 590°C, 600°C and 620°C temper specimens. These were: Cr-rich $M_{23}C_6$ clustered precipitates, Cr-rich $M_{23}C_6$ platelet precipitates, Cr-rich precipitates which were not identified, and AlN precipitates. These are summarised in Table 4-3.

Comparing these results to Figure 2-10 obtained by Irivne et al. $M_{23}C_6$ precipitates were noted for 600°C temper samples both this study and Irvine and et al. [23] For the 580°C and greater temper samples the precipitates were noted preferentially at the grain boundaries. A distinct difference in the SCC behaviour between the 600°C and 620°C sample was noted. This is thought to be a result of the difference in chromium precipitates between the two samples. The 600°C temper sample consisted of predominantly $M_{23}C_6$ clustered precipitates at the grain boundary whereas the 620°C sample contained Cr-rich precipitates which were not identified. A more in depth investigation was

needed to determine the exact crystallographic of this precipitate as the precipitate could not be identified during this study.

TEM analysis of carbon extraction replicas showed the number and size of the precipitates increased with tempering temperature. This analysis is based on the limited number of samples and sample size (TEM samples <100nm). This relationship can be correlated to the material's resistance to SCC, which increased as the tempering temperature increased. Similarly with the study of Irvine et al the quantity of the precipitates has increased with the tempering temperature. [23] Refer to sections 4.4.1.4 and 4.4.2 for time to failure and crack growth rate results.

5.3. Mechanical properties

From the mechanical testing it was observed that hardness values and tensile strength decrease with an increase in tempering temperature. The hardness decreased from 480 HV to 355 HV, at tempering temperatures of 480°C and 620°C respectively. The 0.2% proof strength decreased from an average of 1136.1 MPa to 925.0MPa at a tempering temperature of 480°C and 620°C respectively These results are in agreement with those obtained by van Rooyen et al for FV566 studies [78] as seen in the figures below. The 580°C temper sample demonstrated a tensile strength lower than the 590°C temper sample. The deviation was however within the scatter of the results.

The peak seen in Figure 5-2 at approximately 400-500°C indicates the secondary hardening peak. This secondary hardening peak has been observed by previous researchers and is a typical representation for 12-13% chromium steels [78] [22] [34]. The solid solution strengthening of the material which occurs before tempering is replaced by precipitation strengthening during tempering [13]. This leads to softening of the material and a decrease in hardness values as the tempering temperature increases.

These changes in the mechanical properties with tempering temperature can be attributed to changes in the microstructure as discussed in section 5.1 above.

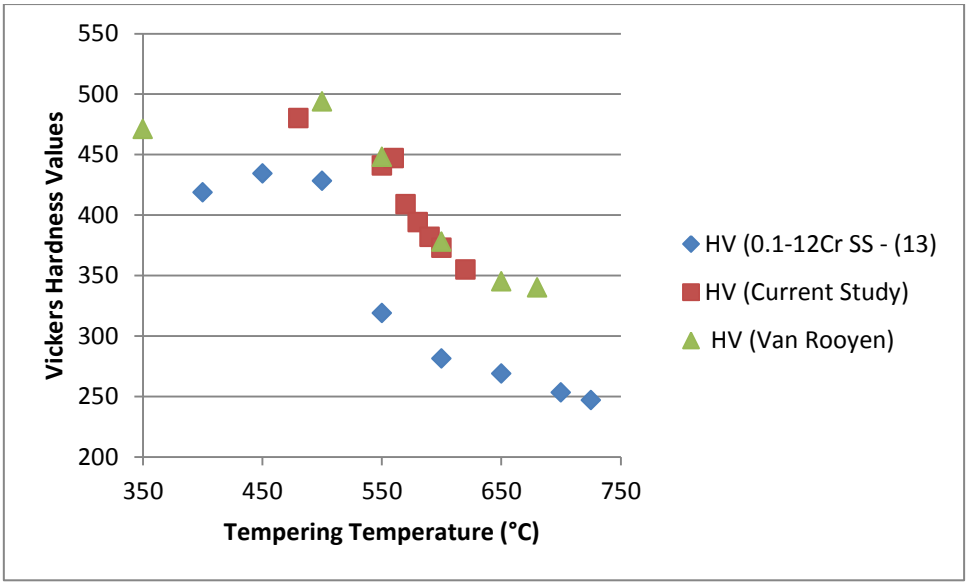

Figure 5-2: Comparison of hardness values obtained this study with previous authors

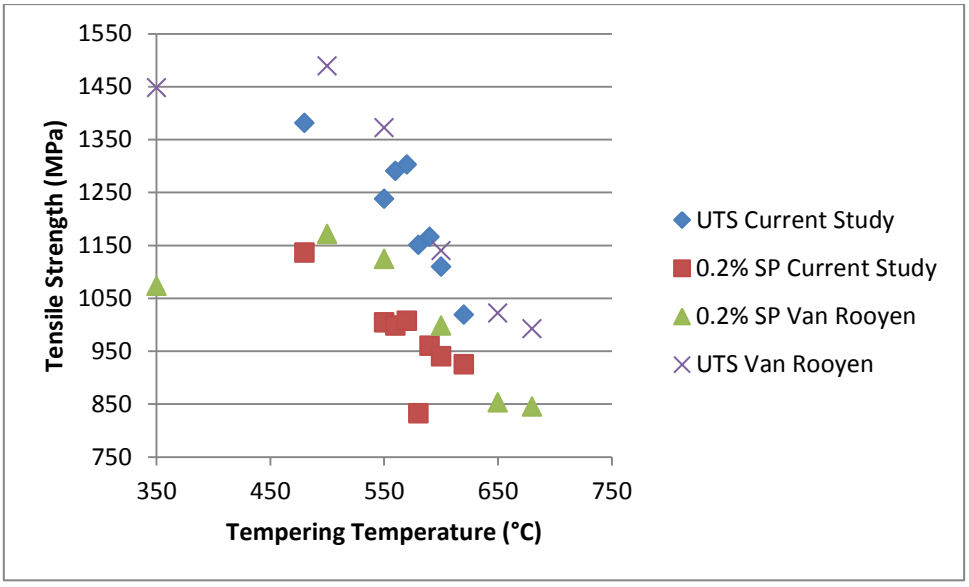

Figure 5-3: Comparison of tensile strength obtained in this study with previous authors

5.4. Stress corrosion testing

5.4.1. Time to failure of U-bend SCC specimens

The time to failure of the U-bend specimens has been recorded as the time taken for the crack to propagate the entire outer surface of the U-bend or when no further discernible crack propagation is noted for a two-week period.

The 480°C and 550°C temper specimens proved to be the most sensitive to SCC – with an average time to failure of 129 and 175 hours respectively. These results concur with research carried out by EPRI on 12% Cr steel X20Cr13, which is commonly used to manufacture LP turbine blades as shown Figure 5-4. [63] X20Cr13 specimens were tested by EPRI by means of a slow strain rate test in 3.5% NaCl (boiling) and demineralised water. EPRI reported the lowest resistance to SCC in the 400-500° temper range. [79] The time to failure of the EPRI 480°C temper slow strain specimens tested to 40%$Rp_{0.2}$ in NaCl, was 2 hours and 100 hours at 80 %$Rp_{0.2}$ in demineralised water.

The 590°C temper specimen failed prematurely. This could have been the process of manufacturing the U-bends and bending. The tests at this temper should be investigated for future work. Due to the prolonged testing times the tests were not repeated.

The 600°C temper U-bend specimen proved immune to SCC after 4000 hours of testing. EPRI showed a time to failure of greater than 4000 hours for X20Cr13 slow strain specimens stressed to 0.4$Rp_{0.2,}$ and 100 000 hours for X20Cr13 specimens in demineralised water stressed to 0.8$Rp_{0.2.}$ [79] The comparison can be seen in Figure 5-4. The 620°C temper specimen failed before the 600°C temper specimen. This is thought to be due to the different carbides present at the grain boundaries.

As seen in Figure 4-27 above, the material's resistance to SCC improved with an increasing tempering temperature – with the 600°C temper specimen being resistant to SCC after 4000 hours of testing. The SCC mechanisms and characterisation are discussed below in section 2.4.2.

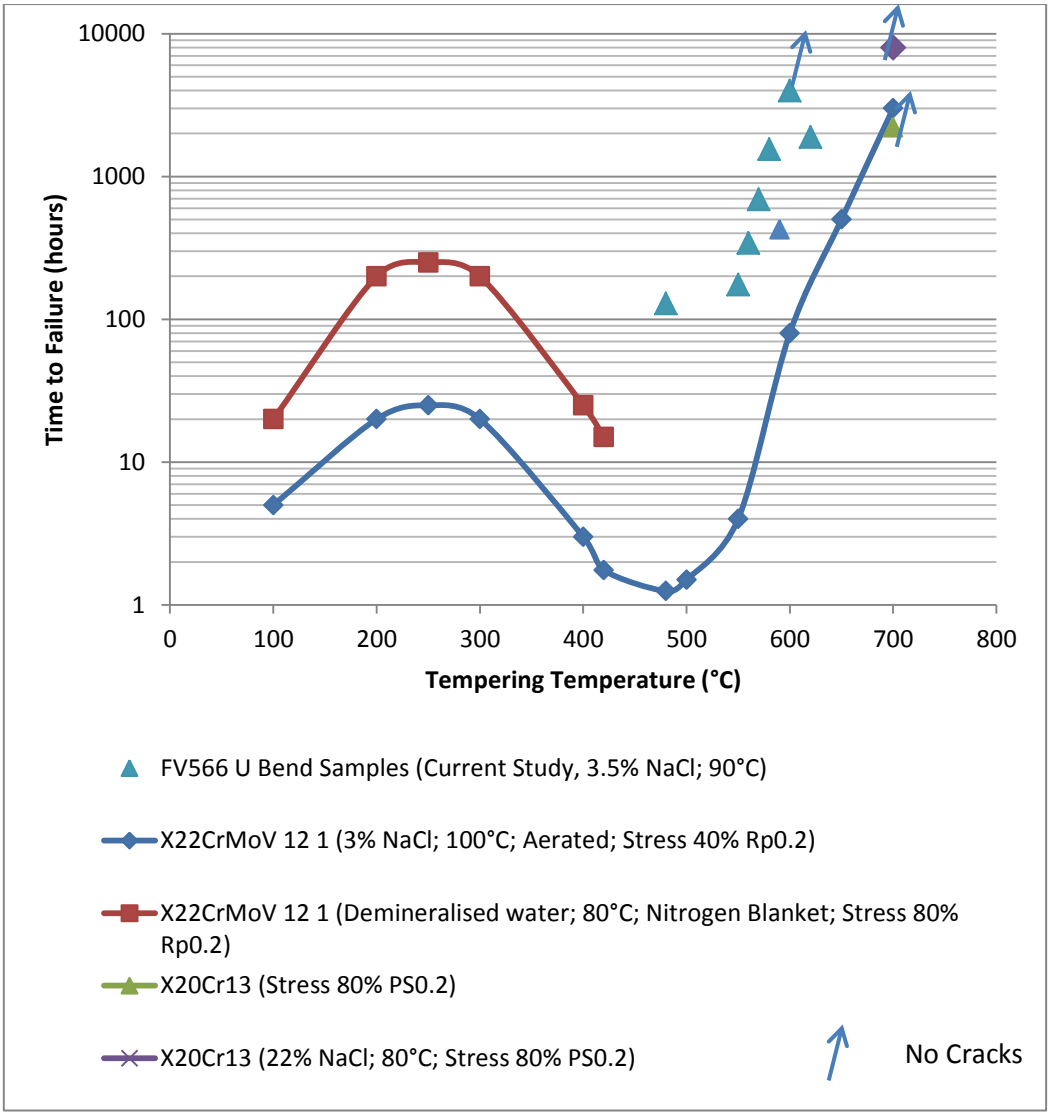

Figure 5-4: Time to Failure Comparison of FV566 and X20 SCC specimens

5.4.2. Stress intensity relationship results

The term crack initiation referenced in the preceding text is used to describe the onset of growth from an existing fatigue precrack.

5.4.2.1. Crack incubation period

Crack growth was preceded by a period of incubation. It was noted that the incubation period for the WOL specimens increased as the tempering temperature of the specimens increased. The starting stress intensity for each specimen varied to achieve crack growth within the time frame of the project, hence a comparison of the incubation periods could not be made. An average incubation period of 48 hours with a starting stress intensity of 62MPa√m was noted for the 480°C

temper specimen, and 2300 hours for the 590°C temper specimen at a starting stress intensity of 47MPa √m.

From the literature, it is known that for crack growth to occur, the starting stress intensity needs to be greater than the threshold stress intensity – in addition to the material being susceptible to SCC. If the starting stress intensity is too low, the incubation period will be extended.

There are two possible reasons for the extended incubation periods. First, is that the solution at the crack enclave does not initially penetrate the crack tip but only the sides of the specimens [39] or the material is resistant to SCC and crack growth is not initiated. At the start of the test the solution has limited access to the crack enclave. The crack tip surfaces are filmed with a protective passive oxide layer which is formed during fatigue precracking. The crack tip is protected from the aggressive environment by the film. This film is ruptured chemically by the environment or by the mechanical force of the starting stress intensity. For SCC to occur, the solution has to be present at the fatigue precrack tip and concentrate at the central regions of the crack tip.

5.4.2.2. Crack length versus test time and stress intensity results

Most WOL specimens showed no crack arrest at test termination. The crack length to width ratio (a/w) extended beyond 0.8, and, consequently, the threshold stress intensity could not be determined for all samples except the 620°C temper specimens. Figure 4-58-Figure 4-63 above show the crack length versus test time data based on a rigid bolt analysis. Based on the time to failure results of the U-bend specimens, it can be anticipated that the threshold stress intensity increases with the tempering temperature. Hence, a higher starting stress intensity was required to initiate crack growth for the 570-620°C temper specimens. Therefore, the starting stress intensity for each of the heat-treated specimens differed as shown in Table 4-6. Crack branching was observed for specimens loaded to low stress intensity. The results from these specimens were discarded.

The maximum crack growth obtained for the 480°C temper specimen was 0,4mm/hr at a computed stress intensity of 45,2MPa√m. This crack growth rate was 10 times higher than that of the 550°C temper specimen. This is due to the brittle nature of the 480°C temper specimen – which failed due to hydrogen embrittlement.

The 560(1) and 580(1) specimens incubation period was followed by a period of crack growth acceleration. The crack growth rate thereafter increases with decreasing crack tip stress intensity. This transient period of crack growth could be due a number of factors as discussed by Hudak and Wei. [51] This period of transient crack growth could be due to changes the chemistry at the crack tip.

This could be due to corrosion product wedging which became dislodged during crack length measurement determination in which the sample was removed from the test environment. The removal of the samples for crack length measurements was kept to a minimum to avoid such discrepancies.

The 580(2) sample incubation period was followed by accelerating crack growth rate. This was preceded by steady state crack growth. At test termination the 580(2) sample did not reach K_{1scc} as the sample crack growth measurements exceeded the specimen's dimension of a/w<0.8 for a valid compliance relationship.

For the 620°C temper specimens the incubation period was followed by accelerating crack growth rate preceded by steady state crack growth. The WOL specimen is a K decreasing specimen. The stress intensity and crack growth relationship showed variability within the temper specimens and could not be compared to Figure 2-28. In figure 4-65 comparison is made of the crack length versus instantaneous crack tip stress intensity for the different temper specimens. A lower crack tip stress intensity was required to enable crack growth for the specimens tempered at lower tempering temperatures.

For FV566 tempered at 650°C for 4 hours and tested in aerated 300ppb Cl^- and 300ppb SO_4^{2-}, Turnball et al. reported a maximum crack growth rate of 143µm/yr at a stress intensity of 74MPa√m. [8] In this environment, K_{1SCC} was determined to be between 42 to 52.9MPa√m by Turnball et al. Turnball reported that K_{1SCC} varied with the environment in which the specimen was tested in. Turnball also evaluated the SCC behaviour of these tempered specimens in a 36ppm Cl^- deaerated solution, and reported a crack growth rate of 44µm/yr at 65MPa√. This crack growth rate was achieved after approximately 12000 hours of testing. [8] These crack growth rates are less than those achieved in this study for the 620°C temper samples. However, a meaningful comparison could not be made between the two crack growth rates – as the bulk chemistry condition in the two tests differed.

A crack growth rate of 44µm/yr is essentially considered arrested for the application of turbine blades in the power generation industry. [8]

For FV566 samples tempered at 600°C, no discernible crack growth was achieved in this study, after 1500 hours of testing at a starting stress intensity of 102MPa√m. Based on the results obtained by Turnball et al., extended testing durations are required to obtain crack growth rate for this type of temper specimen.

Samples tempered at 600°C should be tested for a duration longer than 10 000 hours.

5.4.3. Morphology of fracture surfaces and SCC mechanisms

5.4.3.1. Crack branching

Crack branching from the primary crack was noted on the surface of the U-bend specimens for the 480°C, 550°C, 560°C and 570°C heat treatments. Crack branching was similarly noted in the 480°C, 550°C and 560°C temper WOL specimens.

Significant crack branching was observed for the 480°C and 550°C temper specimens. The amount of crack branching decreased as the tempering temperature increased.

Clark et al. [80] showed that the crack velocity is a significant factor for crack branching to occur. They postulated that crack branching during the initial stages of crack growth is negated by the initial accelerating crack growth due to the initial high applied stress intensities. As the crack propagates, the stress intensities decrease for the WOL and U-bend specimens, crack growth acceleration decreases and becomes constant, and then crack branching occurs.

Congleton and Petch [80] also established that a critical stress intensity is required for crack branching to occur. This stress intensity is greater than two to four times the threshold stress intensity. [80] Hence, for materials with a higher threshold intensity, crack branching will not occur.

For the WOL specimens, as a crack propagates through the specimen the stress state at the crack tip may cause the crack to deviate from the specimen mid-plane. For specimens with a low h/w (height:width) ratio, this will occur unless there is an external force driving the crack growth on the specimen mid-plane. [81] This is the applied stress intensity. Hence, for samples with a low threshold stress intensity which are loaded to relatively low initial stress intensities, crack branching will occur. This was seen for the 480°C, 550°C and 560°C temper WOL specimens.

Specimens with a crack deviation of more than 10% from the primary crack, were not utilised in the da/dt versus K relationship analysis, as per ASTM 1681. [9] WOL specimens are commonly face-notched to overcome crack branching. [71] [81] This should be considered for future research.

5.4.3.2. Post-corrosion cracking

Fractograph examinations of U-bend and WOL specimens revealed that specimens that were exposed to the aggressive solutions for longer periods of time, experienced post-cracking surface corrosion. The 580°C, 590°C and 620°C U-bend specimens exhibited post-corrosion cracking as seen

in Figure 4-43-Figure 4-44 and in the 620°C temper WOL specimens shown in Figure 4-72. The formation of an oxide layer can influence the crack tip chemistry and crack propagation. If the applied stress intensity is insufficient to overcome this layer then a corrosion-controlled crack growth and threshold stress intensity results. [53]

For the WOL specimens, only the 620°C specimen exhibited the post-corrosion cracking. A minimum crack growth rate of $6{,}7.10^{-6}$ mm/hr was determined at a stress intensity of 62MPa√m and 0,01mm/hr at a stress intensity of 55,8MPa√m for the 620(1) and 620(2) temper WOL specimens respectively. This indicates that the threshold stress intensity of 23MPa√m determined for test one at test termination – was corrosion-controlled threshold intensity and not mechanically-controlled threshold stress intensity.

5.4.3.3. Cracking mechanisms

The SCC failure mechanism noted for all temper treatments was intergranular stress corrosion cracking (IGSCC). Cracking was found primarily across prior austenite grain boundaries with cracking across martensite lath boundaries. This is confirmed with EBSD analysis across crack paths of the failed U-bend specimens shown in Figure 4-47-Figure 4-55.

It is well accepted than random high angle grain boundaries (HAB) have high energy than low angle grain boundaries (LAB) providing easier crack paths. Intergranular cracking requires much less energy to propagate comparatively to transgranular cracking [82] [83].

The immunity of the grain boundaries is also largely related to the properties of the materials. For stainless steels IGSCC is commonly associated to sensitisation of the material as a result of chromium depletion at the grain boundaries. This is referred to as anodic dissolution. The sensitisation of the material is further discussed in section5.4.3.Sensitisation by anodic dissolution is the proposed failure mechanism for the 550-620°C specimens. There was no crack arrest marks or microvoid coalescence detected on the fractographic surface of the specimens.

For the 480°C temper specimen, the failure mechanism has been noted by previous researches as IGSCC by hydrogen embrittlement. [8] [34] Comparing the fractographs to the sumamrised features of Table 2-6 voids ahead of the crack tip with cleavage like features were noted. This embrittlement behaviour of 12-13% stainless steels in the 400-500°C temper range, has been observed previously and also noted in this study. [3] [63] [79] [44]

5.4.4. Testing techniques

5.4.4.1. Wedge open loaded specimens

The WOL testing method uses a constant displacement testing specimen. Typically, as the crack propagates, the load and stress intensity decrease until the threshold stress intensity K_{1SCC} is achieved. For a valid K_{1SCC} measurement the (final crack length : width) ratio a/w must be less than 0.8 to satisfy the compliance equation conditions. [9] If the starting stress intensity is elevated, the crack will propagate through the specimen (i.e. a/w>0.8) and valid data for K_{1SCC} will not be achieved. This is the case for the 480(1), 550(1), 560(2), 560(3) and 570(1) WOL specimens. If the starting stress intensity is below the K_{1SCC} value, there is an increased incubation period – resulting in longer testing times and no crack growth initiation. This occurred in 590°C and 600°C temper WOL specimens. If the starting stress intensity is too low – but above the K_{1SCC} value – this can result in crack branching as seen in the 480(2), 550(2) and 560(1) specimens. If crack branching occurs, meaningful data cannot be obtained. The selection of the starting stress intensity is a critical parameter for successfully determining the K_{1SCC} value and eliminating excessive testing times. The time for crack arrest must be factored into selecting this value.

The difficulty experienced in accurately measuring the change in COD and measuring the final load associated with the change in COD can result in errors of K_{1SCC} determination. The change in final COD can be affected by the presence of corrosion products on the fracture surfaces – so introducing errors.

Corrosion-product wedging can generate self-loading forces in excess of the aimed bolt load. [81] Specimens that exhibit increasing crack growth at test termination, may be a result of crack growth accelerations due to corrosion product wedging.

Difference in crack growth measurements between the optical measurements on specimen surface faces and fracture surfaces, will result in errors in determination of stress intensity values and crack growth rates. Minor errors in crack length measurements do not substantially affect the computed stress intensity results.

5.4.4.2. U-bend stress corrosion testing

The U-bend stress corrosion specimen is suitable for determining a material's resistance to SCC. The specimens are easily manufactured and the testing procedure is not difficult to set up. Results of the material's resistance to SCC are readily achieved.

The limitation of the U-bend specimen is the inability to produce quantitative results. The results obtained from the U-bend tests only indicate the material's susceptibility – and do not provide any information on threshold stress intensity and crack growth rates.

The crack growth and time to failure was determined visually with an optical microscope. This determination is subject to interpretation and can result in errors.

5.4.5. Metallurgical influences of tempering on SCC

The SCC failure mechanism observed was intergranular SCC (IGSCC) by sensitisation for the 550°C, 560°C, 570°C,580°C, 590°C, 600°C and 620°C specimens – as shown in section 4.4 on pages 84-95. For the 480°C temper specimen, the failure mechanism has commonly been noted as hydrogen embrittlement. [8] [34] This concurs with observations in this study.

TEM analysis was carried out on a sample taken cross-sectionally across the grain boundary just ahead of the crack tip shown in Figure 4-56 above, for the 590°C U-bend sample. Elemental distribution surrounding the grain boundaries was mapped. The EELS relative Cr count – as shown in Figure 4-57 – appears to decrease from left to right with a minimum count observed at the grain boundaries. [61] This result is, however, inconclusive and does not confirm Cr depletion in the material. Samples of various temper treatments need to analysed, with a quantitative analysis rather than a relative EELS count.

The analysis was largely based on TEM samples with specimen sizes of <100nm. Quantitative elemental analysis of the EELS and EDS data needs to be carried out. Grain boundary analysis highly for the sensitive 480°C and 550°C specimens also needs to be carried out. Nano-beam diffraction of the unidentified precipitates to obtain the crystal structure needs to be done.

The material's resistance to SCC increased with increasing tempering temperature. Chromium-rich precipitates were clearly identified from 560°C temper specimens and above. The quantity and size of the chromium-rich precipitates also increased with increasing tempering temperature. The 550-590°C U-bend samples displayed clear intergranular SCC or sensitisation.

Several authors, as discussed in section 2.3.4.3, showed that this failure mode can be directly linked to the formation of chromium-rich precipitates and the depletion of chromium at the grain boundaries. [84] [82] [36] The 600°C temper samples contained comparatively large amounts of $M_{23}C_6$ precipitates, grouped together at the grain boundaries. These 600°C temper U-bend specimens did not exhibit SCC after 4000 hours. Tavares et al. [44] and Stawsrom and Hillert [43] referred to this as "healing" of the material at this temper treatment and a decrease in sensitivity of the material.

These authors found that tempering for prolonged durations and increasing tempering temperature has an impact in the matrix chromium content at the carbide matrix interface. Tavres postulated increasing the tempering temperature results in a greater quantity and number of precipitates by diffusion of chromium from a point further away in the material – thereby restoring the materials stainless steel properties at the grain boundary. The 620°C temper sample which contained a different chromium rich precipitate at the grain boundary, failed after 1890 hours. This chromium precipitate was not identified. The type of precipitates of the 620°C compared to 600°C temper specimen is thought to have a direct impact of the SCC behaviour.

Previous authors [22] [85; 79] noted that martensitic stainless steels can be tempered below 400°C and above 600°C – but not the in the 400-600°C range in between.

5.5. Summary

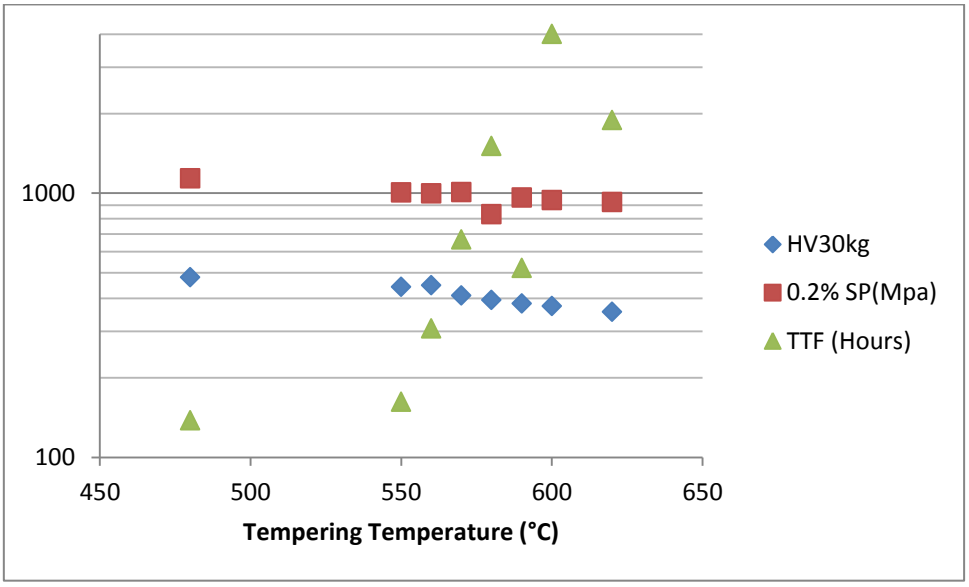

Figure 5-5: Summary of the effect of tempering temperature on FV566

When comparing the results obtained in this study to the hypothesised effects of tempering on SCC and mechanical properties of Figure 5-1 a similar relationship can be noted. The hardness and proof strength of the material decreases whilst the SCC resistance increases. The crack initiation times increased with tempering temperature which is in agreement with Figure 5-1. The results of this study when compared to Figure 5-1 are from the secondary hardening peak. Changes were noted in the carbide composition, morphology and distribution with tempering temperature in this study. A qualitative assessment of the carbides showed the 600°C temper specimen contained a larger

number of chromium precipitates in the matrix and at the grain boundaries. This heat treatment specimen proved to be the most resistant to SCC. A quantitative analysis of the precipitates at the different tempering temperature should be carried out in future work. The 590°C temper specimen has a decreased resistance to SCC when compared to the other lower temper specimens. These results were based on a limited number of specimens and the tests should be repeated. The tempering temperature has a significant effect on the mechanical and stress corrosion cracking properties. These differences can be related to the changes carbide precipitation at the different tempering temperatures. A quantitative analysis of the carbide precipitation should be carried out for future work.

6. Conclusion

The objectives of the study were to determine the effect of tempering on the mechanical behaviour, SCC behaviour, and microstructure of 11-13% Cr stainless steel FV566 turbine blades. The focus was on the tempering temperature used and the influence of this temperature on the SCC mechanism, the crack propagation rates for a given applied stress intensity, and the threshold stress intensity of the material. The tempering temperature was seen to have a significant effect on the properties investigated in the material.

Stress corrosion cracking behaviour

The SCC failure mechanism was intergranular SCC or sensitisation for the 550°C, 560°C, 570°C, 580°C, 590°C, 600°C and 620°C specimens. For the 480°C temper specimen, the failure mechanism was IGSCC by hydrogen embrittlement. Cracking was found primarily across prior austenite grain boundaries – with secondary cracking across martensite lath boundaries.

The material's resistance to SCC improved with increasing tempering temperature. The specimens tempered at higher temperatures were more resistant to stress corrosion cracking. The 480°C and 550°C temper specimens were the most sensitive to SCC with an average time to failure of 175 and 210 hours respectively during U-bend SCC testing, while specimens tempered at 600°C were immune to SCC in a 4000-hour period during susceptibility tests.

The maximum crack growth obtained for the 480°C temper specimen was 10 times higher than that of the 550°C temper specimen. For FV566 samples tempered at 600°C no discernible crack growth was achieved in this study after 1500 hours of testing, at a starting stress intensity of 102MPa√m. Testing durations greater than 10000 hours are required for the 600°C temper specimens. The 600°C temper specimens proved to be the most resistant to stress corrosion cracking for the testing periods employed, and further testing on these samples is indicated for future research.

There was limited success in determining the threshold stress intensity for the different temper specimens. The threshold stress intensity (K1SCC) was determined for the 620°C temper WOL samples. K1SCC was determined using the crack length from the fracture surfaces - as 23MPa.√m and 28MPa.√m for test 1 and 2 respectively. For the remaining temper specimens, the crack length extended beyond the a/w of 0.8. The test method was not successful in determining the threshold stress intensity – and alternative test methods must be investigated in future research.

Microstructural investigation

A change in tempering temperature resulted in a change in the quantity and type of precipitate formed. Changes in resistance to SCC can be related to changes in microstructure. No chromium-rich precipitates were observed in the matrix of the 480°C temper specimen, which proved to be the most sensitive to SCC. Isolated areas of chromium-rich precipitates were observed for the 550°C temper specimen. Chromium-rich precipitates were observed for the 560°C, 580°C, 590°C, 600°C and 620°C temper specimens. These precipitates were identified as AlN, Cr-rich $M_{23}C_6$ precipitates, and unidentified Cr-rich precipitates. The unidentified Cr-rich precipitates were found mainly on the 580°C and 620°C temper samples. Due to the substantial thickness of these particles, diffraction patterns could not be obtained during HRTEM imaging. Future work should identify these Cr-rich precipitates. Chromium-rich precipitates were clearly identified from 560°C temper specimens and above. The 600°C temper samples contained comparatively large amounts of $M_{23}C_6$ precipitates grouped together at the grain boundaries.

Mechanical properties

From the mechanical testing it was observed that hardness values decrease with an increase in tempering temperature. A peak hardness was observed at approximately 480°C tempering temperature. This peak is associated in 12-13% chromium stainless steels is associated with the effects of secondary hardening, which occur during tempering. The 0.2% proof strength of the material decreased with increased tempering temperature. The change in mechanical properties can be related to the change in microstructural characteristics and the precipitates developed.

Overall, the tempering temperature has a significant effect on the SCC behaviour of FV566. The 600°C temper specimen proved to be the most resistant to SCC for the testing durations utilised, and also the most suitable for industrial applications.

7. Future work and recommendations

The current study provided a baseline of the relationship between tempering temperature and SCC. Several areas for future examination and work exist in terms of providing a better characterisation and understanding of the stress corrosion cracking mechanism and crack growth kinetics with tempering temperature:

- The minimum threshold stress intensity was not determined due to the crack length extending beyond the valid compliance relationship or required longer testing times which did not fit in with the testing times of this study. This value is, however, crucial for understanding and predicting the SCC behaviour of the material. Further tests should be carried out with longer testing times in order to obtain the K_{1SCC} value. Alternative testing methods should be investigated: e.g. the constant load testing method with increasing K_1 values.
- Further research is required on the specimen which has the optimum heat-treatment procedure for SCC resistance: the 600°C temper specimen. Tests should include obtaining crack growth kinetics data which could not be achieved during the time frame of this study.
- Precipitates were identified as mainly the chromium-rich precipitates $M_{23}C_6$ and Cr_7C_3. The chromium-rich precipitates for the 620°C samples were not unidentified by this study. Due to the thickness the particles the diffraction patterns and the crystallographic structure could not be obtained with HRTEM imaging. Nano-beam diffraction for obtaining crystallographic information on these unidentified precipitates, should be undertaken.
- During microstructural analysis, no chromium-rich precipitates were found in the 480°C and 550°C temper specimens. Grain boundary analysis for chromium depletion of these samples should thus be carried out.

References

1. **Gonzalez , J, Gutierrez-Solana , F and Varona , JM.** *The effect of microstructure, strength level and crack propagation mode on stress corrosion cracking behaviour of 4135 steel.* Metallurgical and Materials Transactions ,February 1996, Vol. 27A, pp. 281-290.

2. **Askeland, Donald and Phule, Pradeep.** *Science and Engineering of Materials.* s.l. : Brooks/Cole Thompson Learning, 2003. Vol. 4. 0-534-95373-5.

3. **Bezuidenhout, M and van Rooyen, GT.** *Heat Treatment Bench Mark Testing of FV566 Blade Material.* Germiston, South Africa : TSI, Eskom, 2004.

4. **(EPRI), B Dogan.** *Low Pressure Steam Turbine Corrosion: Mechanisms and Interactions: State of Knowledge 2010.* Palo Alto, California : Energy Power Research Institure (EPRI), 2010.

5. **Rimoli, J.** *A Computation model for intergranular SCC.* [Thesis] California, Passedena : California Institute of Technology, 2009.

6. **Turnball, A.** *Current understanding of environment induced cracking of steam turbine steels, 07RTS5.* Texas, USA : NACE International, 2007. NACE International Corrosion Conference and Expo. pp. 1-31.

7. **Gonzalez-Rodriguez J.M., Bahena-Martinez G., Salinas-Bravo J.M.** *Effect of heat treatment on the stress corrosion cracking behaviour of 403 stainless steel in NaCl at 95.* Material Letters, 2008. Vol 43, pp. 208-214.

8. **Turnbull, A. and Zhou, S.** *Comparative evaluation of environment induced cracking of conventional and advanced steam turbine blade steels. Part 1: Stress corrosion cracking.* 2010, Corrosion Science, Vol 52, pp. 2936-2944.

9. **International, ASTM.** *Standard Test for Determining Stress Intensity Factor for Environement Assisted Cracking of Metallic Materials.* [Standard] s.l. : ASTM INternational, 2003. ASTM E1681(E)-03(2008).

10. World Coal Association. [Online] 2012. [Cited: 11 03, 214.] www.worldcoal.org/wa/uses of coal.

11. **M, Bezuidenhout.** *RTD/MAT/13/214.* Rosherville, Johannesburg : Eskom, RTD, 2013.

12. **AB, Outokumpu Stainless.** *Handbook of Stainless Steels.* [Document] Sweden : Awesta Research Centre, Outokumpu, 2013.

13. **ER, Petty.** *Martensite Fundamentals and Technology.* London, Great Britain : Longmang Group Ltd, 1970. SBN 582 46930 9.

14. **Askeland.** *Science and Engineering of Materials.* s.l. : Brooks and Crook, 2003. Vol. 4.

15. **Co., English Electric.** *Firth Vickers FV566 Data Sheet, Spec No. 30/211.* s.l. : English Electric Co., 1967.

16. **Thelning, Karl-Erik.** *Steel and its Heat Treatment, Bofors Handbook.* London : Butterworth Group, 1975. pp. 82-126. ISBN 0 408 70651 1.

17. **Pickering, FB.** *The Metallurgical Evolution of Stainless Steel.* s.l. : The Metals Society, London, 1979. ISBN 0-87170-077-8.

18. **Shatynski, Stephen R.** *The Thermochemistry of Transition Metal Carbides.* Oxidation of Metals, 1979, Vol. 13.

19. **Tschiptschin, André Paulo.** *Predicting Microstructure Development During High Temperature Nitriding of Martensitic Stainless Steels Using Thermodynamic Modeling.* 3, University of São Paulo, Brazil : s.n., Materials Research, Vol. 5, pp. 257-262.

20. **ASTM.** *Metal Handbook, Vol8.* s.l. : ASTM, 1973.

21. **D, Porter and K, Easterling.** *Phase Transformation in Metals and Alloys.* United Kingdom : Van Nostrand Reinhold, 1980.

22. **F.B., Pickering.** *Physical Metallurgy and the design of steels.* London : Applied Science Publishers Ltd, 1978.

23. **KJ Irvine KJ, et al** *High alloy steels.*. London : The iron and steel institute, 1964, Vol. 34.

24. **M. C. PAYARES-ASPRINO, H. KATSUMOTO, AND S. LIU.** *Effect of Martensite Start and Finish Temperature on Residual Stress Development in Structural Steel Welds.* Welding Journal, 2008, pp. 279-289.

25. **Pickering FB, Irvine KJ.** *High strength 12% Chromium steels.* s.l. : The Iron and Steel Institute, 1964, The Metallurgical Evolution of Stainless Steels, pp. 63-78.

26. **Doubel, Philip.** *Private Communication on Dilatometry of FV566.* Cape Town : University of Cape Town, 2017.

27. **Sarioglu, F.***The effect of tempering on susceptibility to SCC of AISI 4140 steel in 33% sodium hydroxide.* Material Science and Engineering, 2001, pp. 98-102.

28. **Babylon, Univeristy of.** EDU - University of Babylon. [Online] [Cited: 02 15, 2017.] http://en.uobabylon.edu.iq/.

29. **SEQUEIRA, CÉSAR A. C.** *Some Considerations on the Background of Passivity.* Corrosion Prot Mater, 2010, Vol. 29.

30. [Online] [Cited: 02 18, 2017.] http://nptel.ac.in/courses/113108051/module3/lecture20.pdf.

31. **Hinds, Gareth.** The Electrochemistry of Corrosion. *National Physical Laboaratory* . [Online] [Cited: 02 18, 2017.] www.npl.co.za.

32. **TL, Anderson.** *Fracture Mechanics Fundamentals and Applications.* s.l. : Taylor and Francis Group, 2005. Vol. 3rd. ISBN: 13: 978-1-4200-5821-5.

33. **S, Gulbrandsen.** *Overview of SCC in Stainless Steel: Electronic Enclosures in Extreme Enviromental Conditions.* Maryland : DFR Solutions.

34. **(EPRI), Energy and Power Institute.** *Embrittlement of Power Plant Steels.* Palo Alto : Energy and Power Institute (EPRI) , 2013. 3002001474.

35. **Mayo, William E.** *Predicting IGSCC/IGA susceptibility of Ni-Cr-Fe alloys by modeling of grain boundary chromium depletion.* Materials Science and Engineering, 1997, Vol. A232, pp. 129-139.

36. **Hall EL, Briant CL.** *Chromium depletion in the vicinty of carbides in sensitised austenitic stainless steels* Metallurgical Transactions, 5, May 1984, Vol. 15, pp. 793-811.

37. **Atanda P et al.** *Sensitisation Study of Normalized 316L Stainless Steel.* USA : Journal of Minerals & Materials Characterization & Engineering, 2010, Vol. 9.

38. **Kai et al.***The IGSCC, sensitisation and microstructural study of alloly 600 and 690.* 3, s.l. : Nuclear Engineering and Design, November 1993, Vol. 144, pp. 449-457.

39. **Sarver et al.** *Effect of carbide precipitation on the corrosion behavior of Inconel alloy 690.* San Franciso : NACE International Corrosion, March 1987, NACE International Corrosion, Vol. 43.

40. **Yanliang, Huang, Kinsella, Brian and Becker, Brian.** *Sensitisation identification of stainless steel to intergranular stress corrosion cracking by atomic force microscopy.* s.l. : Elservier, 2008, Science Direct, Vol. 62, pp. 1863-1866.

41. **Holzworth, M L and Beck, F H.** 1977, Corrosion, Vol. 7, pp. 441-449.

42. **Cowan, R L and Gordon, G M.** *Proc. Conf. Stress Corr. Cracking and Hydrogen Embrtittlement.* NACE, Houston : s.n., 1977, p. 1025.

43. **Stawstrom, C and Hillert, M.** 1969, Journal of Iron and Steel Institute, Vol. 207, pp. 77-85.

44. **Tavares, SSM et al .***Microstructure and Intergranular Corrosion Resistance of UNS 17400 Stainless Steel.* [ed.] Elsevier. 2010, Corrosion Science, Vol. 52, pp. 3835-3839.

45. **Chial, V et al.** *On the development of the electropotential method.* s.l. : Acta, 2001, Electrochim, Vol. 46.

46. **Schleithoff et al.** *Corrosion Fatigue of Stean Turbine Blade Materials.* Palo Alto, California : EPRI, 1981. Workshop Proceedings.

47. **Holdsworth, S.** *A review of Factors Influencing the Mechanisms of Environmental Crack Initiation.* Proceedings: Workshop on Corrosion of Steam Turbine Blading and Disks in the Phase Transition Zone.

48. **Dietzel, W.** *Fracture Mechanics Applications to SCC beyond K.* Germany : GKSS-Forschungszentrum Geesthacht GmbH.

49. **Roylance, David.** *Introduction to Fracture Mechanics.* Massachussetts : Department of Materials Science and Engineering, Massachusetts Insitute of Technology, 2001, June 14.

50. **RP Wei, Novak, Williams.** *Some important considerations in teh development of stress corrosion testing methods.* s.l. : Fritz Engineering Labraotary Report No.358.36, 1971.

51. **Hudak, SJ and Wei, RP.** *Consideration of Nonsteady Crack Growth in Materials Evaluation and Design.* 1, s.l. : International Journal for Pressure Vessels and Piping, 1979, Vol. 9, pp. 63-74.

52. **Zhanpeng Lu *, Tetsuo Shoji, Yoichi Takeda, Yuzuru Ito, Akira Kai, Seiya Yamazaki.***Transient and steady state crack growth kinetics for stress corrosion cracking of a cold worked 316L stainless steel in oxygenated pure water at different temperatures.* s.l. : Corrosion Science, 2008, Vol. 50, pp. 561-575.

53. **RS, Thompson.** *The Stress Corrosion Cracking of Corrosion Abrasion Resistant Development Steels.* Cape Town : University of Cape Town, 1991 December.

54. **AH Hanish, LH Burk.** 6, s.l. : Corrosion Science, 1986, Vol. 4, p. 331.

55. **Carter, C M.** 10, 1969, Corrosion, Vol. 25, p. 423.

56. **International, ASM.** *Standard Test Methods for Tensile Tesing of Metallic Materials.* [Standard] s.l. : ASM International, 2011. ASTM E8/EM-11.

57. **Hafner, Bob.** [Online] [Cited: October 30, 2014.]

58. **AR, Marder.** *Replication Microscopy Techniques for NDE.* s.l. : ASM International, 1989. ASM Handbook Volume 17: Nondestructive Quality Control and Testing.

59. **N.M, Hall and J.M., Capus.** *A selective extraction replica technique for carbides in steel.* s.l. : Journal of Science and Instrumentation, 1966, Vol. 43.

60. **International, ASM.** *Chapter 2 - Extraction Replica Techniques.* [Standard] s.l. : ASM International, 1973. STP 547-EB/Oct 1973.

61. **Westraadt, J.** *Stress Corrosion Crackign of FV566.* Nelson Mandela Metropolitan University. Port Elizabeth : s.n., 2015.

62. **Wei RP, Novak SR, Williams DP.** *Some Important Considerations is SCC Testing.* s.l. : Fritz Engineering Laboratory Report, 1971, October. 358.36.

63. **Electric Power Research Institute.** *Steam Turbine Reliability Workshop.* Boston, Massachusetts : s.n., 1982, July 7-9.

64. **ASTM.** ASTM International. *ASTM Internation Website.* [Online] 97. [Cited: 04 16, 2013.] www.astm.org. E30-97.

65. **International, ASTM.** *Standard Test Method for Evaluating SCC of Stainless Steel Alloy with different Nickel content in boiling acified sodium chloride solution.* 2011. G123-00.

66. **Maitland T, Sitzman S.** EBSD Technique and Materials Characterisation Techniques. [book auth.] Lin Wang Z Zhou W. *Scanning microscopy for NanoTechnology: Techniques and Applications.* s.l. : Springer Science and Business Media, 2007, March.

67. **Wright S, De Clou R, Nowell M.** *EBSD Analysis of Cracks in Polycrystalline Materials.* [Report] s.l. : EDAX.

68. **Manjoine, MJ.** *Biaxial Brittle Fracture Tests.* s.l. : American Society of Mechanical Engineers, 1965, June, JOurnal of Basic Engineering Transactions, Vols. pgs 293-298.

69. **ET, Wessel.** *State of the Art WOL Specimen for K1C Fracture Toughess Testing.* 1, Engineering Fracture Mechanics, 1986, pgs 77-103, June, Vol. 1.

70. **DB, Dawson.** *Development of a Stress Corrosion Cracking Test For Armor Alloys.* Watertown, Massachussetts : Army Materials and Mechanics Research Centre, 1972 June. AD746251.

71. **Novak SR, Rolfe ST.** *Modified WOL Specimen for K1SCC Environmental Testing.* Journal of Materials , 1969, Vol. 3, pgs 701-728.

72. **Yokobori T, Watanabe J, Aoki T, Iwadate T.** *Evaluation of K1SCC Testing Procedure by Round Robin Tests on Steels.* Boulder, Coloraso : ASTM International, 1985, June 25-27. Fracture Mechanics Eighteenth Symposium.

73. **Wei RP, Novak SR.** *Interlaboratory Evaluation of K1SCC and da/dt Deterination Procedures for High Strenght Steels.* January, Journal of Evaluation and Testing, 1987, Vol. 15, pgs 38-75.

74. **International, ASTM.** Standard Test Method for Measurement of Fatigue Crack Growth Rates. *ASTM International.* [Online] 2013. [Cited: March 19, 2013.] www.astm.org. ASTM 647-13.

75. *Oxford, HKL Channel 5 Software.*

76. **Perkins, Bache.** *Corrosion fatigue of a 12%Cr low pressure turbine blade steel in simulated service environment .* International Journal of Fatigue, 2005, Vol 27, pp. 1499-1508.

77. **S, Gulbrandsen.** DRF Solutions. *DRF Solutions Website.* [Online] [Cited: 02 27, 2013.] http://www.dfrsolutions.com/uploads/white-papers/WP_Stress.pdf.

78. **Bezuidenhout M., Rooyen v G.T.** *Heat Treatment Bench Mark Testing of FV566 Blade Material.* Germiston, South Africa : TSI, Eskom, 2004.

79. **Jaffee, R.I.** *Corrosion Fatigue of Steam Turbine Blade Materials.* Palo Alto, California : Pergamon Press, 1981. Electric Power Research Institute. pp. 69-85.

80. **CS, Carter.** *Stress Corrosion Crack Braching in High Srength Steels.* Being Commercial Airplane Divison. Washington : s.n., March 1969. AD687725.

81. **Domack, MS.***Evaluation of K1SCC and da/dt Measurements for Aluminium Alloys using Precracked Specimens.* Philadelphia : American Society for Testing of Materials, 1990, ASTM STP 1049, pp. 391-409.

82. **Gertsman VY, BruemmerSM.** *Study of Grain Boundary Character Along Intergranular Stress Corrosion Crack Paths In Austenitic Alloys.* s.l. : Acta Mata, 2001, Vol. 49, pp. 1589-1598.

83. **Arafin MA, Szpunar JA.** *A new understanding of intergranular stress corrosion cracking resistance of pipeline steel through grain boundary character and cyrstallographic texture studies.* s.l. : Corrosion Sciene, 2009, Jan, Vol. 51, pp. 119-128.

84.**Was, GS.** *Grain Boundary Chemistry and Intergranular Fracture in Austenitic Nickel-Base Alloys.* 4, April 1990, Corrosion, Vol. 46.

85. **Book, ASM Metals Hand.** Heat Treatment. s.l. : ASM International, 1991, Vol. 4.

86. **P Bing, et al.** *Two dimensional digial image correlation for in plane displacement and strain measurement: A review.* s.l. : IOP Publishing Ltd, 2009, Measurement of Science and Technology, Vol. 20, pp. 1-17.

87. **Cook A, et al.** *Preliminary Evaluation of Digital Image Correlation for In-situ Observation of Low Temperature Atmospheric Induced Chloride SCC in Austenitic Stainless Steels.* 25, s.l. : The Electrochemical Society, 2010, ECS Transactions, Vol. 37, pp. 119-132.

88. **Cook A, et al.** *Low Temperature Atmospheric Induced Chlroide Stress Corrosion Cracking of Austenitic Stainless Steels.* [Presentation] s.l. : University of Manchester, 2010.

89. **Becker, Selim.** Surface Pattern Technique for DIC of Stress Corrosion Cracking Samples . [Electronic communication]. s.l. : University of Oxford.

90. **Filiz, S** *The effect of tempering on susceptibility to stress corrosion cracking of AISI 4140 steel in 33% sodium hydroxide in at 80°C.* Journal of Material Science and Engineering A315, 2001, pp. 98-102.

91. **Dietzel W., Ghosal S.K.** *Stress Corrosion Cracking - A New Approach To Testing Methods.* Journal of Material Science, 1997, Vol 33, No.4, pp. 516-523.

92. **Tchizhik A.A., Tchizhik T.A., Tchizhik Anna A.** *Optimization of the heat treatment for steam and gas turbine manufactured for 9-12% Cr steels.* Journal of Materials Processing Technology, 1998 Vol 77, pp. 226-232.

93. **Klotz, Solenthelar, Uggowitzer.** *Matensitic-austenitic 9-12% Cr steels - Alloy design, microstructural stablity and mechanical properties.* 2008, Materials Science and Engineering A, 146, pp. 186-,194.

94. **Janovec J., Svoboda M., Blach J.** *Evolution of secondary phases during quenching and tempering 12%Cr steel.* Materials and Science Engineering A246, 1998, pp. 184-189.

95. **Vickers, Firth.** *FV566 Data Sheet.* Sheffield : Brown Firth Research Labrotaries .

96. **LD, Barlow.** *The Effect of Austenising and Tempering Parameters on the Microstructure and Hardness of Martensitic Stainless Steel AISI 420.* Pretoria, South Africa : University of Pretoria, 2009.

97. **Fabien, Leonard.** *Study of Stress Corrosion Cracking of Alloy 600in High Temperature High Pressure Water.* Manchester, United Kingdom : University of Manchester, 2010.

98. *I* **Judy, R. W., Jr., King, W. E., Jr., Hauser, J. A., II, and Crooker, T. W.** I*nfluence of Experimental Variables on the Measurement of Stress Corrosion Cracking Properties of High Strength Steels.* s.l. : American Society for Testing of Materials, Environmentally Assisted Cracking: Science and Engineering, 1990, ASTM STP 1049, pp. 410-422.

99. **Lisagor, WB.** *Influence of precracked specimen configuration and starting stress intensity on the stress corrosion cracking behaviour of 4340 steels.* Philidelphia : American Society for Testing and Materials, 1984, ASTM STP 821, pp. 80-97.

Appendix A

Microstructural analysis

Elemental analysis

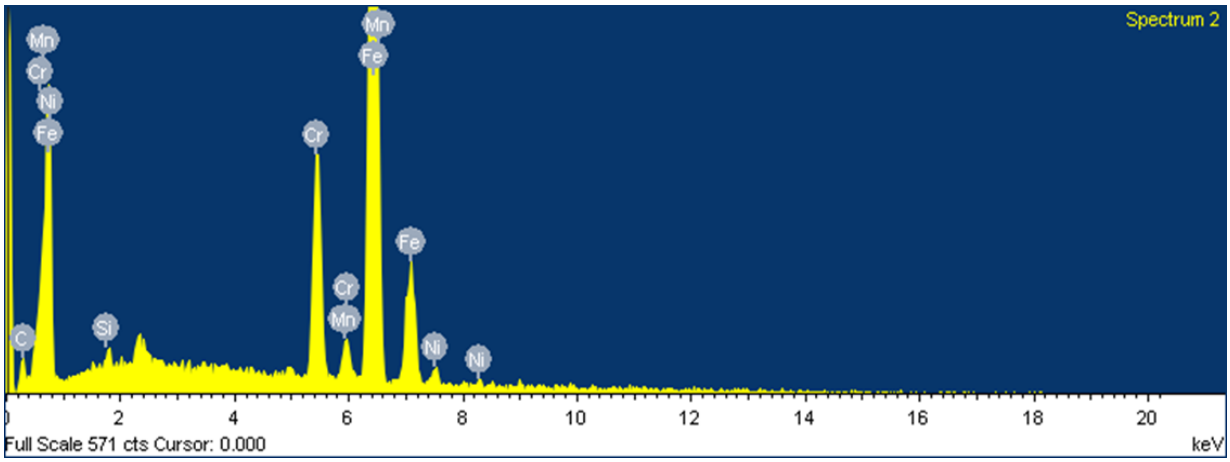

Figure A-1: SEM EDS analysis of inclusion content on as received FV566 turbine steel

Element	Weight %	Atomic %
C	4.83	18.89
Si	0.52	0.86
Cr	12.07	10.90
Mn	0.96	0.82
Fe	79.29	66.67
Ni	2.33	1.86

Table A-1: SEM EDS elemental analysis of as received FV566 turbine steel

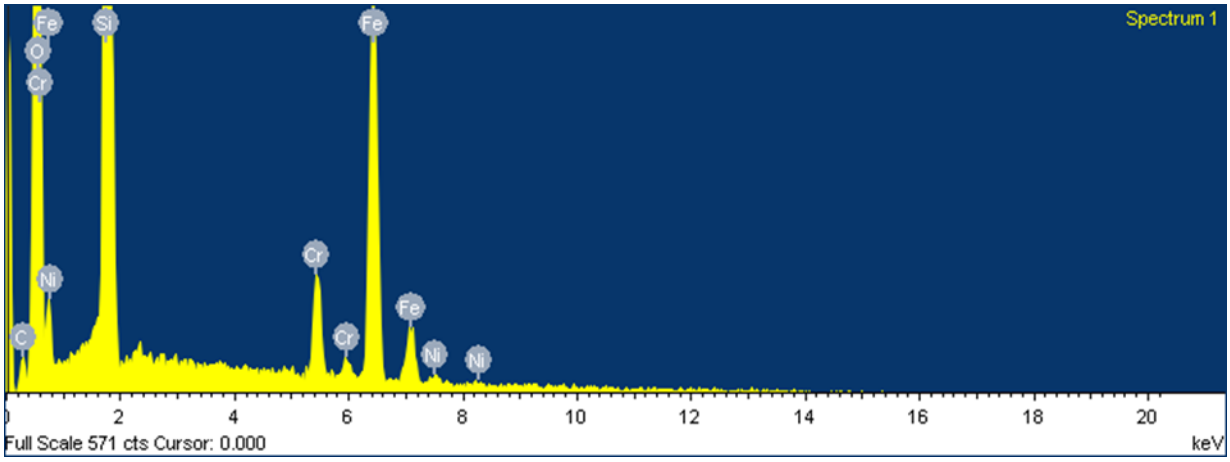

Figure A-2: SEM EDS analysis of inclusion content on as 550°C temper FV566 turbine steel

Element	Weight %	Atomic %
C	5.39	9.77
O	43.29	58.88
Si	29.26	22.67
Cr	3.39	1.42
Fe	18.23	7.10
Ni	0.44	0.16

Table A-2: SEM EDS elemental analysis of 550°C temper FV566 turbine steel

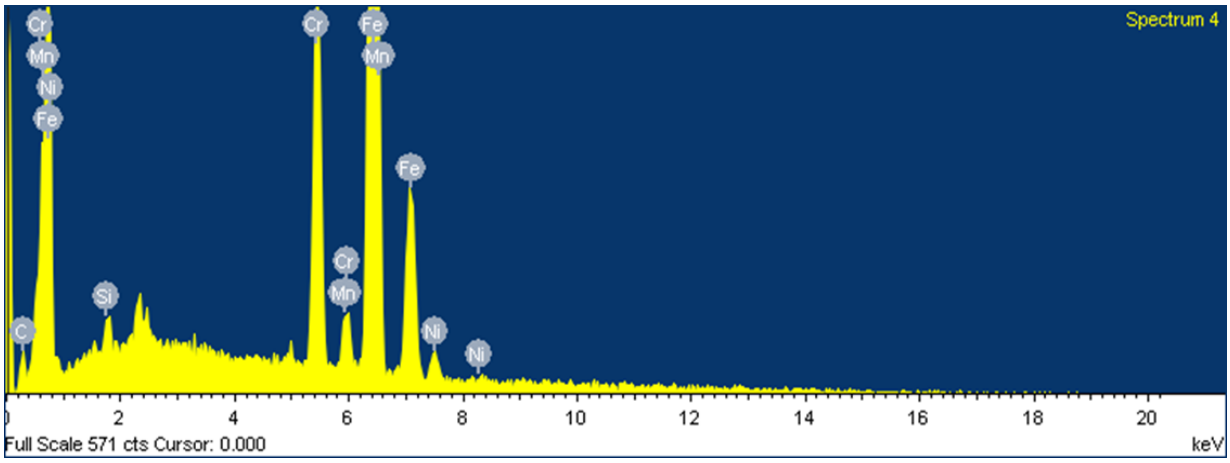

Figure A-3: SEM EDS analysis of inclusion content on as 550°C temper FV566 turbine steel

Element	Weight %	Atomic %
C	3.90	15.67
Si	0.71	1.21
Cr	12.28	11.39
Mn	0.81	0.72
Fe	80.03	69.14
Ni	2.27	1.87

Table A-3: SEM EDS elemental analysis of 550°C temper FV566 turbine steel

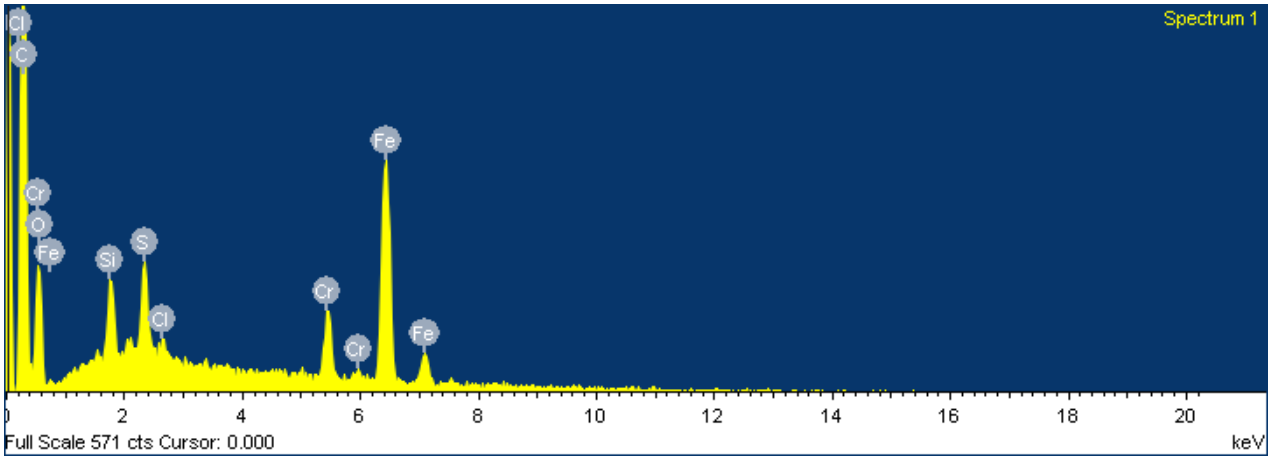

Figure A-4: SEM EDS analysis of inclusion content on as 570°C temper FV566 turbine steel

Element	Weight %	Atomic %
C	58.28	76.28
O	15.71	15.43
Si	1.50	0.84
S	1.95	0.96
Cl	0.43	0.19
Cr	3.38	1.02
Fe	18.76	5.28

Table A-4: SEM EDS elemental analysis of 570°C temper FV566 turbine steel

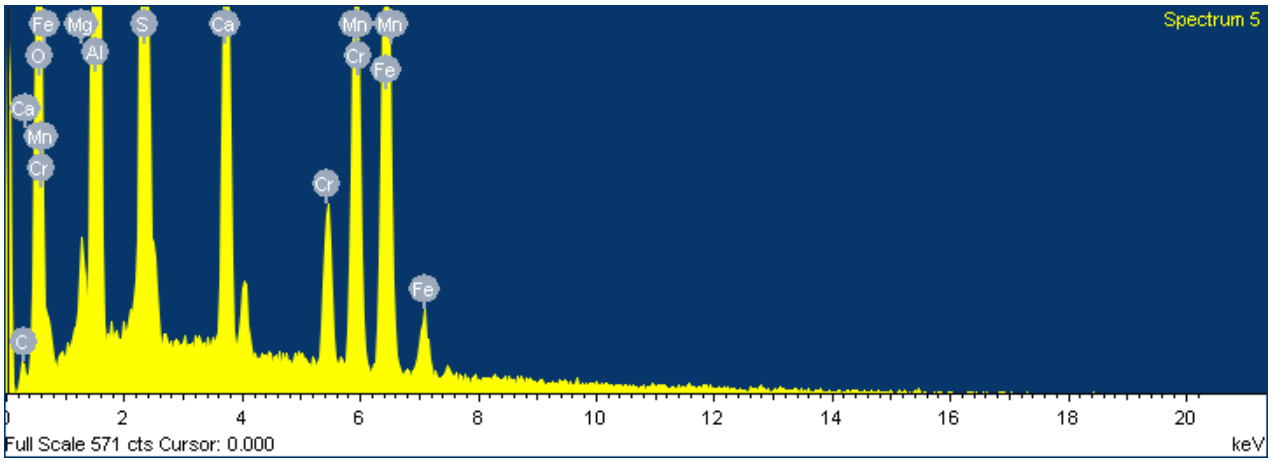

Figure A-5: SEM EDS analysis of inclusion content on as 570°C temper FV566 turbine steel

Element	Weight %	Atomic %
C	2.91	6.39
O	26.25	43.34
Mg	0.73	0.80
Al	21.11	20.67
S	11.89	9.80
Ca	6.67	4.39
Cr	3.72	1.89
Mn	11.67	5.61
Fe	15.05	7.12

Table A-5: SEM EDS elemental analysis of 570°C temper FV566 turbine steel

Appendix B

U Bend test

The information below pertains to the U-bend SCC tests.

Figure B-1: Light micrograph of 480°C temper polished U-bend specimen

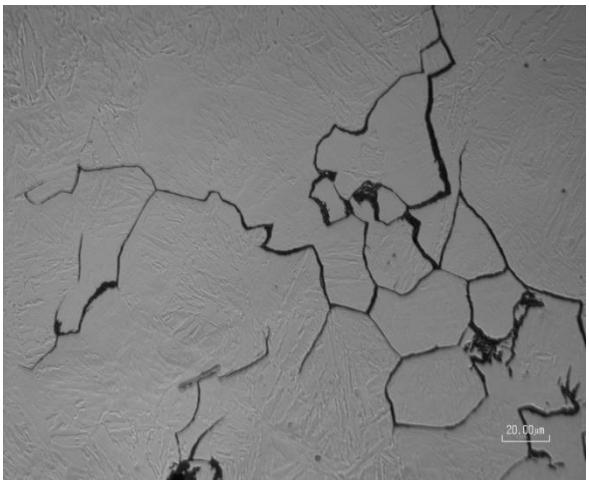

Figure B-2: Light micrograph of 480°C temper polished U-bend specimen

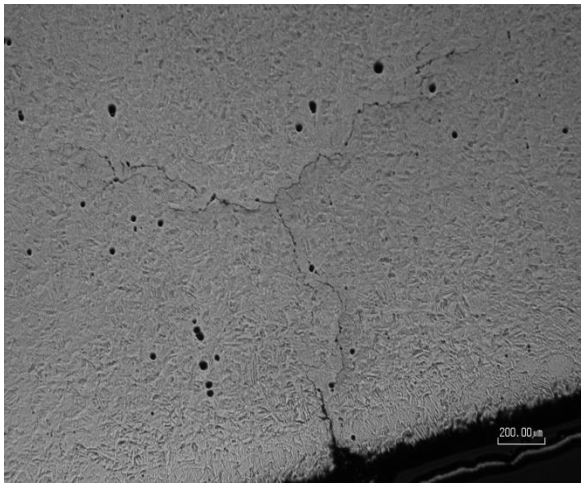

Figure B-3: Light micrograph of 550°C temper polished U-bend specimen

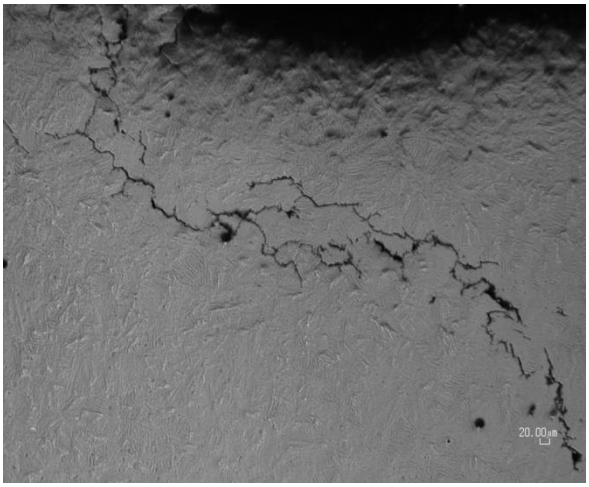

Figure B-4: Light micrograph of 550°C temper polished U-bend specimen

Appendix C

WOL test specimens

The information below pertains to the WOL tests.

Initial crack opening measurements

The initial crack mouth opening displacement is listed in Table C-1.

Tempering Temperature (°C)	Test 1	Test 2	Test 3
480	0,252	0,120	
550	0,178	0,135	0,178
560	0,315	0,230	
570	0,330	0,296	
580	0,327	0,322	
590	0,314	0.330	
600	0,407	0,380	
620	0,400	0,403	

Table C-1: Initial crack opening displacement V0 for the WOL Tests

WOL crack measurement images

Figure C-1: 480(1) temper WOL with crack growth extending beyond a/w=0.8. K1SCC could not be determined as compliance equations were not satisfied

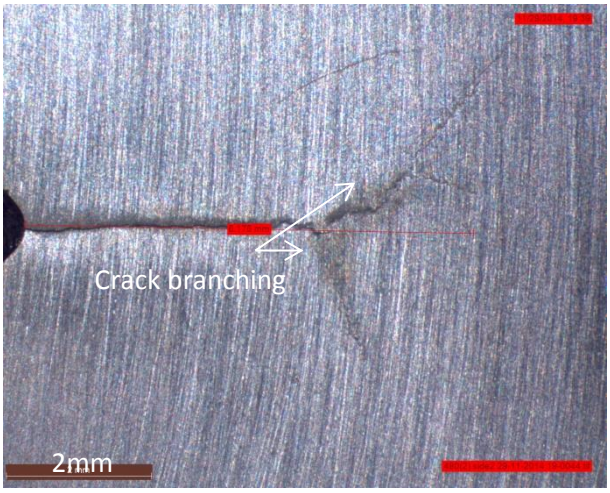

Figure C-2: 480(2) temper WOL specimen with crack branching

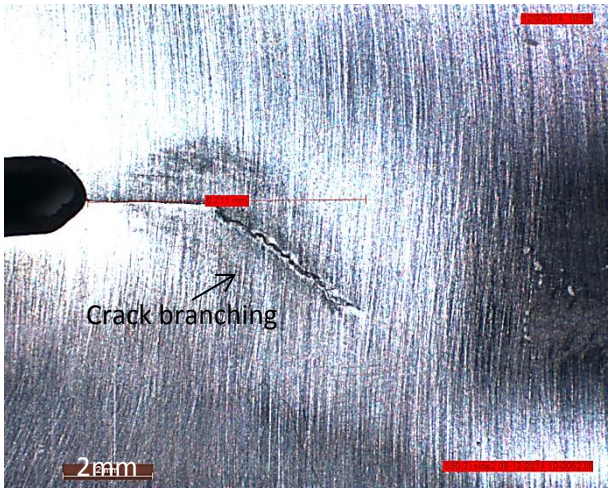

Figure C-3: 550(2) temper WOL specimen with crack branching

Figure C-4: 560(2) temper WOL specimen with crack branching

Final crack length measurements

Below are images of the final crack length measurements:

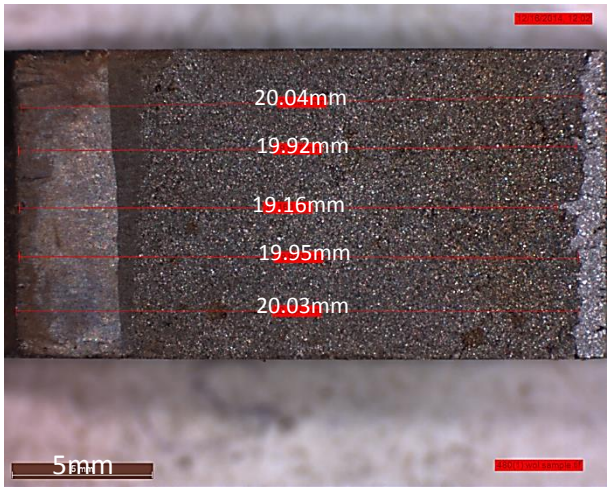

Figure C-5: Final crack length measurement of 480(1) temper specimen, with the final crack length to width ratio (a/w) > 0.8.

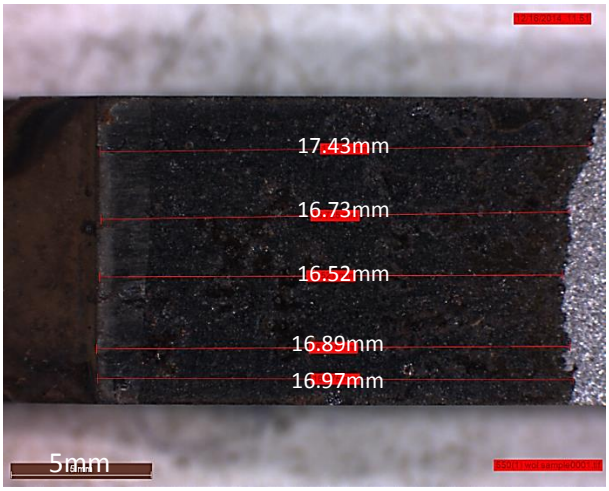

Figure C-6: Final crack length measurement of 550(1) temper specimen, with the final crack length to width ratio (a/w) > 0.8

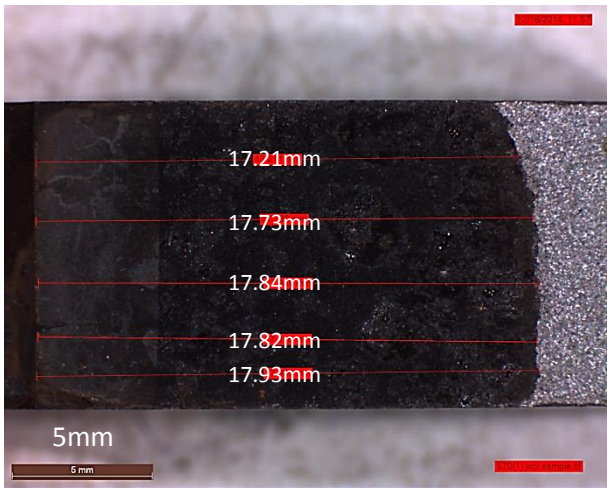

Figure C-7: Final crack length measurement of 570(1) temper specimen, with the final crack length to width ratio (a/w) > 0.8

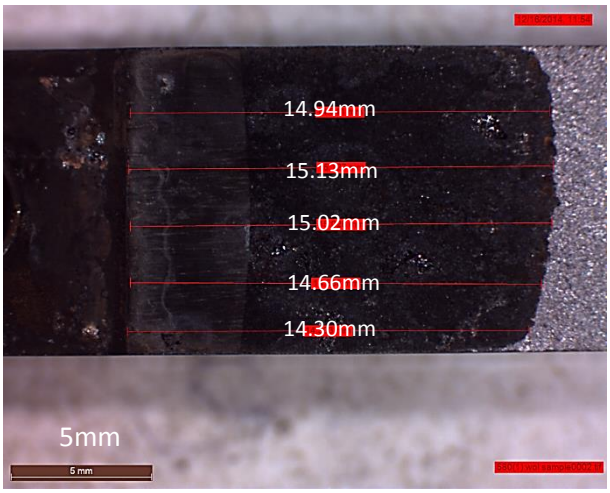

Figure C-8: Final crack length measurement of 580(1) temper specimen

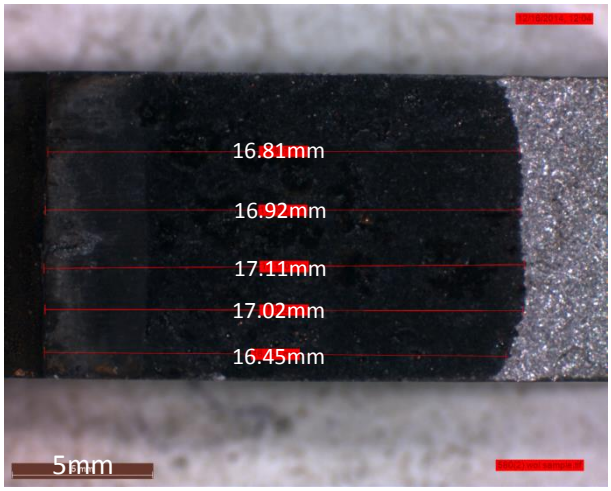

Figure C-9: Final crack length measurement of 580(2) temper specimen

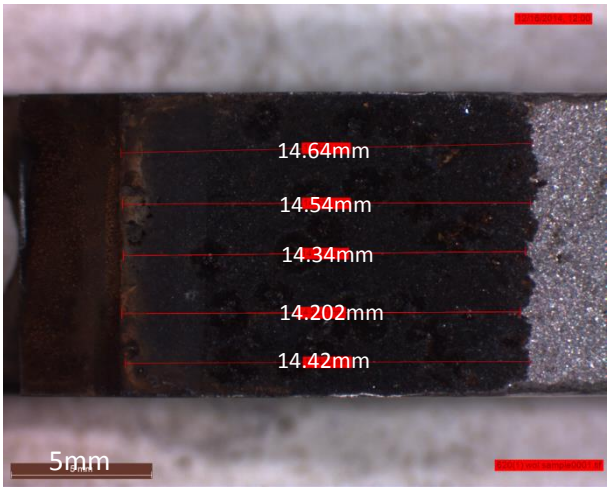

Figure C-10: Final crack length measurement of 620(2) temper specimen